



Anna Maria Werkovits, BSc

# Surface tension measurements of liquid nickel and steel W360 using electromagnetic levitation

## Master's Thesis

to achieve the university degree of  
Diplom-Ingenieur

Master's degree programme: Technical Physics

submitted to  
**Graz University of Technology**

Supervisor  
Ao.Univ.-Prof. Dipl.-Ing. Dr.techn. Gernot Pottlacher

Co-Supervisor  
Dipl.-Ing. BSc Thomas Leitner

Institute of Experimental Physics

Graz, November 2019

This document is set in Palatino, compiled with pdfL<sup>A</sup>T<sub>E</sub>X<sub>2</sub>ε and Biber.

The L<sup>A</sup>T<sub>E</sub>X template from Karl Voit is based on KOMA script and can be found online: <https://github.com/novoid/LaTeX-KOMA-template>

## **Affidavit**

I declare that I have authored this thesis independently, that I have not used other than the declared sources/resources, and that I have explicitly indicated all material which has been quoted either literally or by content from the sources used. The text document uploaded to TUGRAZonline is identical to the present master's thesis.

---

Date

---

Signature



## Acknowledgement

First of all, I wish to express my sincere appreciation to my supervisor Prof. Gernot Pottlacher, who gave me the opportunity to write my thesis at the *Thermophysics and Metalphysics Group*, take part in conferences and to author a publication. From the very outset, I received excellent mentoring. Next, I would like to pay my special regards to my co-supervisor DI Thomas Leitner, as he supported me day by day, so I was able to learn a lot about scientific working, engineering and, of course, the challenges and difficulties that are occurring at surface tension measurements by the method of electromagnetic levitation. I am also very grateful to the group colleagues DI Peter Pichler and DI Matthias Leitner for fruitful inputs and discussions. In general, I really enjoyed being part of the group the last year.

I also wish to show my gratitude to our project partner Dr. Siegfried Kleber and the company *voestalpine BÖHLER Edelstahl GmbH & Co KG* for cooperation and the *Austrian Research Promotion Agency (FFG)* for supporting me with an research grant. I appreciated also the discussions with Dr. Boris Wilthan from NIST, Boulder, about improving quality in temperature acquisition and with Prof. Douglas Matson about the influence of finite surface deformation on surface tension measurements. I also received generous support from the publishing fund of the *Graz University of Technology* for financing the open access attribute of the paper that will be published soon in the journal *High Temperatures-High Pressures*.

Without the guidance and persistent help of Hana Hampel, completing my studies would not have been possible. At last, I owe my deepest gratitude to my parents for their encouragement, support and love.

## Abstract

In this work temperature dependent surface tension of two different liquid metallic materials was determined. The first investigation was carried out on the hot-work steel *W360* produced by the Austrian company *voestalpine BÖHLER Edelstahl GmbH & Co KG* with the aim of obtaining surface tension as function of temperature. *BÖHLER* intends to use these data later as input parameter for ab initio simulations of various processes.

The second part of the thesis focussed on high purity nickel. In the *Thermophysics and Metalphysics Group* at *Graz University of Technology*, measurement results of the surface tension of liquid nickel have been already published in 2015 by *Aziz, Schmon and Pottlacher* [4]. As those results seemed to be elevated regarding the recent literature, the decision was made to perform a re-measurement. In a comprehensive literature review, 17 studies starting from the 1950s were investigated particularly regarding the experimental and evaluational methods used, which allowed to narrow the bandwidth of the surface tension results as a few were classified as "not recommended". When the re-measurement was performed, results were shifted by  $-7\%$  with respect to the ones obtained by *Aziz, et. al.* In the course of searching for the reason of this drastic deviation, the original measurement data of *Aziz, et. al.* were re-evaluated, which decreased the surface tension results by fairly  $-8\%$  as the translational frequency in the vertical direction has been misidentified by *Aziz, et. al.* In the end, the discrepancy between those two studies was reduced to  $1.3\%$ , which now gives an overlap within the measurement uncertainty of both data sets.

In addition, an extensive uncertainty analysis was performed according to *GUM*. As well, numerous influencing factors were discussed, which mainly cannot be treated within the uncertainty analysis by *GUM*. This involves for example the finite surface deformation amplitudes, the contamination with surface active substances, pyrometric challenges and the misidentification of the translational frequency in the vertical direction.

## Kurzfassung

Im Zuge dieser Arbeit wurde die temperaturabhängige Oberflächenspannung von zwei flüssigen metallischen Materialien bestimmt. Zuerst wurde der vom österreichischen Unternehmen *voestalpine BÖHLER Edelstahl GmbH & Co KG* hergestellte Warmarbeitsstahl *W360* untersucht. Die erhaltenen Oberflächenspannungsdaten werden zukünftig als Eingangsparameter für ab-initio Simulationen verschiedener Fertigungsprozesse verwendet.

Der zweite Teil der Diplomarbeit beinhaltet eine umfassende Untersuchung der Oberflächenspannung von hochreinem flüssigen Nickel. In der *Arbeitsgruppe für Thermophysik und Metallphysik* der *Technischen Universität Graz* wurde bereits im Jahre 2015 eine Publikation von *Aziz, Schmon und Pottlacher* [4] zu diesem Thema veröffentlicht. Die damals erhaltenen Oberflächenspannungsdaten lagen deutlich über den Literaturwerten der letzten Jahre, sodass eine weitere Untersuchung veranlasst wurde. Dazu wurde im Vorfeld zur Neuvermessung eine Literaturrecherche im Umfang von 17 Studien durchgeführt, wobei das Hauptaugenmerk auf die verwendeten Mess- und Evaluationsmethoden gelegt wurde. Speziell die Evaluationsmethoden welche bei der elektromagnetischen Levitation angewandt wurden entsprachen teilweise nicht dem heutigen Stand der Technik, sodass die Bandbreite der vertrauenswürdigen Literaturwerte der Oberflächenspannung von Nickel reduziert werden konnte. Die Neuvermessung ergab eine im Mittel um 7 % niedrigere Oberflächenspannung im Vergleich zu den von *Aziz, et al.* ermittelten Daten. Um dieser drastischen Abweichung auf den Grund zu gehen, wurden die originalen Messdaten von *Aziz, et al.* erneut ausgewertet, wodurch sich das Resultat um ca. -8 % geändert hat, da ursprünglich die Translationsfrequenz in vertikaler Richtung nicht korrekt identifiziert wurde. Somit beträgt die Diskrepanz der beiden Messergebnisse letztendlich 1.3 %, wobei sich deren Unsicherheitsbereiche sogar überlappen. Zusätzlich wurde eine umfassende Unsicherheitsanalyse nach *GUM* durchgeführt. Einige der möglichen Einflüsse die nicht anhand von *GUM* quantifiziert werden können, da sie keinen Eingang im theoretischen Modell finden, wurden ausführlich diskutiert. Beispiele dafür sind finite Oberflächendeformationen, die Kontamination mit oberflächenaktiven Substanzen, pyrometrische Herausforderungen und inkorrekte Identifikation der vertikalen Translationsfrequenz.



# Contents

<b>1</b>	<b>Motivation</b>	<b>1</b>
1.1	Hot-work steel <i>W360</i> . . . . .	2
1.2	Nickel . . . . .	2
<b>2</b>	<b>Introduction</b>	<b>5</b>
2.1	Electromagnetic levitation . . . . .	5
2.2	Electrostatic levitation . . . . .	8
2.3	Oscillating drop technique . . . . .	9
2.4	Pyrometry . . . . .	15
<b>3</b>	<b>Experimental</b>	<b>17</b>
3.1	Setup of the EML apparatus . . . . .	17
3.1.1	Oscillation circuit . . . . .	18
3.1.2	Pumping system . . . . .	20
3.1.3	Temperature acquisition . . . . .	21
3.1.4	Levitation atmosphere . . . . .	22
3.1.5	Videometry . . . . .	24
3.1.6	Previous setup modifications and improvements . . . . .	25
3.2	Measurement procedure . . . . .	26
3.2.1	Sample preparation . . . . .	26
3.2.2	Levitation preparation . . . . .	26
3.2.3	Temperature regulation, measurement and calibration . . . . .	27
3.2.4	Density measurements and evaluation . . . . .	29
3.2.5	Surface tension measurements and evaluation . . . . .	31
<b>4</b>	<b>W360</b>	<b>39</b>
4.1	Experimental . . . . .	39
4.2	Density . . . . .	44
4.3	Surface Tension . . . . .	46

## Contents

<b>5 Nickel</b>	<b>49</b>
5.1 Literature research . . . . .	49
5.2 Re-measurement . . . . .	55
5.2.1 Material, experimental and evaluation details . . . . .	55
5.2.2 Density . . . . .	60
5.2.3 Surface tension . . . . .	62
5.3 Re-evaluation of Aziz study . . . . .	64
5.4 Conclusion . . . . .	69
<b>6 Uncertainty Analysis</b>	<b>73</b>
6.1 Influencing factors . . . . .	73
6.1.1 Influences at measurement . . . . .	74
6.1.2 Influences at evaluation . . . . .	84
6.2 Statistical reproducibility . . . . .	90
6.3 Uncertainty budget . . . . .	91
<b>7 Outlook</b>	<b>95</b>
<b>Appendix</b>	<b>96</b>
<i>W</i> <sub>360</sub> . . . . .	96
Nickel . . . . .	96
<b>Bibliography</b>	<b>115</b>

# List of Figures

2.1	Schematic sketch of the levitation coil . . . . .	6
2.2	Position and heating efficiency factors . . . . .	7
2.3	Schematic sketch of ESL . . . . .	9
2.4	Exemplary dependence of of oscillation frequencies on translational frequencies . . . . .	13
3.1	Schematic experimental setup of the EML apparatus used . .	17
3.2	Levitation coils used for measurements . . . . .	19
3.3	Schematic sketch of the pumping system . . . . .	20
3.4	Typical temperature profiles and plateaus . . . . .	28
3.5	Series of density images . . . . .	29
3.6	Evaluation of density frames . . . . .	30
3.7	Series of surface tension images . . . . .	31
3.8	Evaluation of surface tension frames . . . . .	32
3.9	Spectra of translational frequencies in x- and y-direction . . .	33
3.10	Determination of translational frequency in z-direction . . . .	34
3.11	Visualisation of the $l = 2$ oscillation modes . . . . .	34
3.12	$R_\alpha$ and $R_{\alpha+90^\circ}$ spectra . . . . .	35
3.13	$R_+$ and $R_-$ spectra . . . . .	35
3.14	$R_\alpha$ spectra for several angles . . . . .	37
4.1	$W_{360}$ samples in all experimental stages . . . . .	40
4.2	Typical temperature profile at experiment . . . . .	42
4.3	Liquidus and solidus plateaus of $W_{360}$ . . . . .	43
4.4	Results of temperature dependent density measurements of $W_{360}$ . . . . .	44
4.5	Results of temperature dependent surface tension measurements of $W_{360}$ . . . . .	46
5.1	Literature study of surface tension of liquid nickel . . . . .	52

## List of Figures

5.2	Nickel samples in different stages of preparation and experimentation . . . . .	56
5.3	Temperature profile of one experiment of nickel . . . . .	58
5.4	Density results of liquid nickel and literature . . . . .	60
5.5	Results of the surface tension of nickel for different suppliers	62
5.6	Re-evaluation of data obtained by <i>Aziz</i> . . . . .	64
5.7	Visualisation of the dependence of the Rayleigh frequency on the translational frequencies . . . . .	66
5.8	Conclusion of nickel investigations with recommended literature, results from re-measurement and re-evaluation of data obtained by <i>Aziz</i> . . . . .	69
6.1	Influencing factors of surface tension measurements . . . . .	73
6.2	Dependence of pyrometer readings at the melting plateau on the heating rate . . . . .	75
6.3	Dependence of pyrometer reading at the melting plateau on the mass specific heating rate . . . . .	76
6.4	Vapour pressures of selected metals . . . . .	78
6.5	Typical radial surface deformation of nickel measurements .	81
6.6	Extremal radial surface deformation of nickel measurements	82
6.7	Radial surface deformation of nickel measurements performed by <i>Aziz</i> . . . . .	83
6.8	Dependence of levitation time on mass loss . . . . .	87
6.9	Mass loss in dependence of integrated temperature profile of nickel measurements . . . . .	88
6.10	Statistical spread of surface tension measurement and evaluation . . . . .	90

# List of Tables

3.1	Technical data of the pyrometers used . . . . .	21
3.2	Heat capacities of filling gases . . . . .	23
4.1	Typical chemical composition of $W_{360}$ . . . . .	39
4.2	Liquidus and solidus temperatures of $W_{360}$ . . . . .	40
4.3	Information about specimen mass and experimental parameter of $W_{360}$ . . . . .	41
4.4	Density fit parameter of $W_{360}$ . . . . .	45
4.5	Surface tension fit parameter of $W_{360}$ . . . . .	47
5.1	Overview of OD evaluation formulas used in nickel literature	50
5.2	Literature study of the surface tension of liquid nickel . . . . .	51
5.3	Classification of nickel literature regarding to purity . . . . .	54
5.4	Material information of nickel samples . . . . .	55
5.5	Specimen mass and experimental parameter of nickel . . . . .	57
5.6	Result of density measurements of liquid nickel with corresponding literature . . . . .	61
5.7	Surface tension fit parameter of liquid nickel . . . . .	63
5.8	Surface tension fit parameter after the re-evaluation of data obtained by <i>Aziz</i> . . . . .	65
5.9	Mode splittings of <i>Aziz</i> study and this work . . . . .	67
5.10	Conclusion of the obtained surface tension fit parameter . . . . .	70
6.1	GUM uncertainty budget of surface tension of $W_{360}$ . . . . .	93
6.2	GUM uncertainty budget of surface tension of nickel . . . . .	94
7.1	Obtained density data points of $W_{360}$ . . . . .	97
7.2	Obtained surface tension data points of $W_{360}$ . . . . .	98
7.3	Exemplary density and surface tension fit data points of steel $W_{360}$ . . . . .	99

List of Tables

7.4	Obtained density data points of nickel . . . . .	100
7.5	Obtained surface tension data points of nickel . . . . .	102
7.6	Exemplary density and surface tension fit data points of nickel	109

# Abbreviations

Common physical measures used within this work:

$T$	...	Temperature / K or °C
$T_M$	...	Melting temperature / K or °C
$T_L$	...	Liquidus temperature / K or °C
$T_S$	...	Solidus temperature / K or °C
$\epsilon$	...	Normal spectral emissivity / a.u.
$\rho$	...	Density / $\text{kg} \cdot \text{m}^{-3}$
$\gamma$	...	Surface tension / $\text{N} \cdot \text{m}^{-1}$

Common methods measuring the surface tension of liquid metals:

EML	...	Electromagnetic Levitation
ESL	...	Electrostatic Levitation
OD	...	Oscillating Drop
SD	...	Sessile Drop
DDW	...	Dynamic Drop Weight
MBP	...	Maximum Bubble Pressure

Companies:

*BÖHLER* ... *voestalpine BÖHLER Edelstahl GmbH & Co KG*



# 1 Motivation

Thermophysical properties, such as surface tension, density, viscosity etc., of liquid metals have become a topic of high importance. Reliable data are essential for the design of welding, casting and other processes like metal additive manufacturing in the metalworking industry. With methods like CALPHAD, equilibrium phase diagrams of new alloys can be simulated by the knowledge of thermophysical properties of each alloy component. But the experimentation with liquid metals is quite challenging due to their high chemical reactivity. In general there are two types of setup approaches: Either measurements are operated non-containerlessly, where the melt is at least partially in contact with a crucible or any surface, or containerlessly, where the sample is only in contact with the measuring atmosphere. In this work, data acquisition is only performed containerless by use of the electromagnetic levitation (EML) setup of the *Thermophysics and Metalphysics Group at Institute of Experimental Physics (IEP), Graz University of Technology (TU Graz)*.

The thesis focuses on the investigation of temperature dependent surface tension of two metallic materials. Firstly, data of the commercial hot-work steel W360 produced by *voestalpine BÖHLER Edelstahl GmbH & Co KG* is obtained for use in powder metallurgy simulations. The other part of this work deals with nickel. As surface tension data in the literature are highly spreading the surface tension of nickel is re-measured and an extensive literature study is performed regarding possible influencing parameter.

## 1 Motivation

### 1.1 Hot-work steel W360

The Austrian company *BÖHLER* produces high quality special steels. Aside of the conventional manufacturing route consisting of primary melting, secondary metallurgy, casting and recasting the route of powder metallurgy has been launched in the recent years. In comparison to the the conventional route, the liquid steel is filled in a tundish where the homogenized melt is atomised at its nozzle. The resulting powder with typical particle sizes in the  $\mu\text{m}$ -range is either used in *metal additive manufacturing* or a *hot isostatic pressing (HIP)* is performed. Complex product geometries without the need of casting moulds can be realised by metal additive manufacturing methods like *selective laser melting*, which can be described as 3D printing of metals or steels. Additionally, very fine microstructures can be achieved as diffusion is widely hindered through the short-time exposure of the laser [1]. In comparison to conventional manufacturing methods like casting or forging, *HIP* attains microstructures with increased refinement, homogeneity and isotropy, which also refers to the distribution of alloy components [2]. Simulating all these processes requires knowledge of the temperature dependent surface tension of the liquid steels, amongst other thermophysical properties. As the presence of surface-active elements like oxygen or sulphur is responsible for a significant decrease in surface tension, potential impurity sources at experimentation have to be minimized.

### 1.2 Nickel

Nickel is one of the most common alloy components, thus trustable thermophysical data in the liquid phase like surface tension and density are essential for designing processes or new alloys in metal industry. Starting in the 1950s, the surface tension of liquid nickel has been measured numerous times using different techniques. Most of the results have been obtained containerlessly by the *Oscillating Drop (OD)* technique and some by non-containerless methods, such as *Sessile Drop (SD)* and *Maximum Bubble Pressure (MBP)*. It is evident that the temperature dependent surface tension data spread over a broad range. For example, the surface tension at the

melting point, varies from (1653 to 1924)  $\text{mN}\cdot\text{m}^{-1}$ , which corresponds to a span of 16 % referred to the minimal value.

In general, non-containerless measurements yield lower surface tension values than containerless measurements. Hence, the spread may be caused by the use of various measuring methods and setups, but also due to different evaluation methods and especially the purity of the specimen. Regarding the measurements performed by means of the OD technique, there was a progress in theory in 1991, as Blackburn and Cummings derived a mathematical description for the behaviour of the levitated drop under terrestrial conditions [3]. Therefore, the OD results gained from ground-based experiments before 1991 yield typically too high values and thus have a loss in significance.

In 2010, Kirmanj Aziz and Alexander Schmon started to build up the EML apparatus in the *Thermophysics and Metalphysics Group* at *Graz University of Technology*. Later in 2015, one of the first publications of measurement results obtained by the apparatus, about the surface tension of liquid nickel, was released by Aziz, Schmon and Pottlacher [4]. When comparing to recent literature, the results of the study appeared to deliver relatively high values for surface tension. In the course of the investigation of the iron-nickel-system in 2017, see Leitner, Klemmer and Pottlacher [5], the earlier obtained results for pure nickel also seemed to be increased and did not fit to the iron-nickel results well. For this reason the decision was made to re-measure the surface tension of liquid nickel and to investigate which material, experimental or evaluation parameter like purity, type of impurities, measurement/evaluation method, oxygen contamination, atmosphere, etc. could cause such highly spreading literature. At this time, strong influences in impurity composition seemed to be a plausible explanation, therefore nickel samples of different suppliers but at same purity have been investigated. In general, comparing single studies regarding their material, measurement and evaluation parameter raise difficulties as essential information is often not stated at all. Regarding purities, typically only purities on metals basis are provided in publications or sometimes even by suppliers, although the knowledge of the content of non-metallic substances like oxygen or sulphur is relevant for performing surface tension measurements.



## 2 Introduction

Containerless processing of metallic samples has the advantage that high temperatures of metallic melts can be achieved without interacting chemically with a crucible or any other surface. This saves the sample from contamination, but complicates the handling, which can then only be performed by means of levitation. There are various methods to accomplish the levitation of a sample: Acoustically, aerodynamically, magnetically, electrostatically or electromagnetically, to name a few. For the investigation of metals and alloys it is most eligible to use electromagnetic or electrostatic levitation, whereas each method has its own benefits and drawbacks. In the following sections and as well in the whole work the focus is put on containerless methods, which enables surface tension evaluation by the *Oscillating Drop (OD)* technique. Later in the literature study of the surface tension of nickel, other non-containerless experimental methods like *Sessile Drop (SD)*, *Maximum Bubble Pressure (MBP)* and *Dynamic Drop Weight (DDW)* have been used. A detailed description of those methods would go beyond the scope of this thesis, but a good survey is given in [6, 7].

### 2.1 Electromagnetic levitation

Electromagnetic levitation (EML) requires a radio frequency (RF) oscillation circuit, where power is coupled into the sample between two contrariwise twisted coils (Figure 2.1). The induced inhomogeneous alternating electromagnetic field generates eddy currents inside the conducting sample, which cause the effects of positioning and inductive heating [8]. In addition a fluid flow is provoked, that is stronger here than in case of electrostatic levitation.

## 2 Introduction

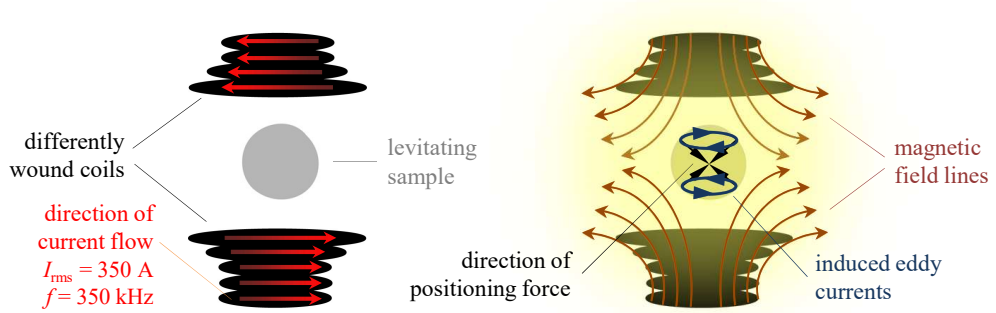


Figure 2.1: Two schematic sketches of the levitation coil inclusive plotted current flow, magnetic field lines, induced eddy currents and direction of the positioning force. (Right figure partly adapted from Thomas Leitner.)

**Positioning:** The induced currents in the sample generate according to *Lenz's law* a magnetic field that is oppositionally directed to the external field. As a consequence the sample is shifted by the *Lorentz force* as far to regions of lower magnetic field strength as the gravitational force is counteracted. An approach of the emerging lifting force through a multipole expansion of lowest order [9] is stated in Equation 2.1. Accordingly, the final position of the sample depends on its mass, conductivity and density as well as on the geometry, strength and frequency of the primary magnetic field. The positioning efficiency  $Q(q)$  is plotted in Figure 2.2.

$$\text{Lifting force: } \vec{F} = -\frac{4\pi R_s^3}{3\mu_0} Q(q) \vec{\nabla} B^2 \quad (2.1)$$

$$\text{with } q = \frac{R_s}{\delta}, \delta = \sqrt{\frac{2}{\omega\sigma\mu_0}} \text{ and } Q(q) = \frac{3}{4} \left( 1 - \frac{3}{2q} \frac{\sinh(2q) - \sin(2q)}{\cosh(2q) - \cos(2q)} \right)$$

$R_s$	...	sample radius / m
$B$	...	magnetic flux density of the external RF field / T
$\omega$	...	angular frequency of the RF field / Hz
$\sigma$	...	sample conductivity / $\text{S} \cdot \text{m}^{-1}$
$\delta$	...	skin depth / m
$\mu_0$	...	vacuum magnetic permeability ( $1.256\,637\,062\,12 \times 10^{-6} \text{ N} \cdot \text{A}^{-2}$ from [10])

In principle the only use of the lower coil would be sufficient for achieving levitation, but for enhanced stabilization the upper coil is implemented to the setup.

## 2.1 Electromagnetic levitation

**Inductive heating:** The sample is heated intrinsically due to the ohmic losses of the induced eddy currents. The absorbed power is given in Equation 2.2 [9] and depends beside of the magnetic field strength mainly on the EM field frequency and the conductivity of the sample. Samples with a poor conductance can be heated well. In Figure 2.2 the heating efficiency  $H(q)$  is depicted, which has a maximum at about  $q \approx 2$ .

$$\text{Heating power: } P = \frac{4\pi}{3} \frac{\omega R_s^3}{2\mu_0} H(q) B^2 \quad (2.2)$$

$$\text{with } q = \frac{R_s}{\delta}, \delta = \sqrt{\frac{2}{\omega\sigma\mu_0}} \text{ and } H(q) = \frac{9}{4q^2} \left( q \frac{\sinh(2q) + \sin(2q)}{\cosh(2q) - \cos(2q)} - 1 \right)$$

- $R_s$  ... sample radius / m
- $B$  ... magnetic flux density of the external RF field / T
- $\omega$  ... angular frequency of the RF field / Hz
- $\sigma$  ... sample conductivity /  $\text{S} \cdot \text{m}^{-1}$
- $\delta$  ... skin depth / m
- $\mu_0$  ... vacuum magnetic permeability ( $1.25663706212 \times 10^{-6} \text{ N} \cdot \text{A}^{-2}$  from [10])

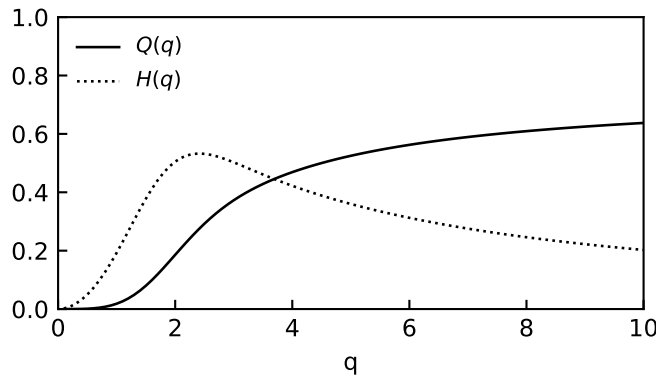


Figure 2.2: Dependence of the position  $Q(q)$  and heating  $H(q)$  efficiency factors on  $q = \frac{R_s}{\delta}$  from Equation 2.1 and 2.2

Similar to induction cookers, additional heating power is generated for ferromagnetic samples below the corresponding *Curie temperature* through cyclic magnetisation losses. Practically, this has only an impact on heating

## 2 Introduction

in the solid phase as *Curie temperatures* are typically lower than melting or liquidus temperatures except for a few ferrofluids in the undercooled region [11].

**Fluid flow:** At electromagnetic levitation the fluid flow is predominantly driven by the *Lorentz force*. Due to the permanent stirring, multi-component alloys are prevented from de-mixing or segregation. But this is the only positive side effect as turbulent material flow inside the bulk material may occur and possibly effect the surface energy of the sample. Fluid flow can also be caused by *Marangoni convection*, which is driven by a surface tension or temperature gradient, natural convection and buoyancy effects. [12]

Experiments can either be performed under terrestrial conditions or under microgravity ( $\mu g$ ) like on parabolic flights (*TEMPUS*) or on the *International Space Station* (ISS). Due to terrestrial gravity, EML experiments hold disadvantages such as the drop-shaped deformation of the liquid sample and the occurrence of turbulent fluid flow. In  $\mu g$  the drop exhibits an ideal spherical shape and laminar flow is only occurring as lower positioning forces are required. Additionally, a decoupling of controlling positioning and heating can be achieved through separate coil systems. After the melting process, only insignificantly small forces are acting on the metal drop, so the drop is almost perfectly spherical. To excite surface oscillations short heating pulses are generated. Accordingly, the sample is quenched and the formerly excited surface oscillations are damped, so that also the viscosity can be determined. This is not possible at terrestrial EML as surface oscillations are excited continuously due to permanently strong magnetic fields. [13, 14]

## 2.2 Electrostatic levitation

Processing samples with electrostatic levitation (ESL) requires negatively charged materials. Therefore the spectrum of investigation objects is extended by non-metals, especially oxides. The electrostatic field is induced by two oppositional charged and vertical arranged electrodes, whereas the lower one is charged negatively to orientate the established electric field in the manner that the sample experiences a lifting force against gravity. To fix

## 2.3 Oscillating drop technique

the horizontal position, the electrodes exhibit either a concave or ring-type geometry in order to create a field inhomogeneity. Vertical positioning can be achieved easily by altering the voltage between the electrodes, but heating occurs not intrinsically as for EML. For this reason one or multiple high power lasers are deployed. In addition to surface tension, also viscosity measurements are able even for terrestrial setups. [15]

A schematic sketch of the ESL realization is depicted in Figure 2.3.

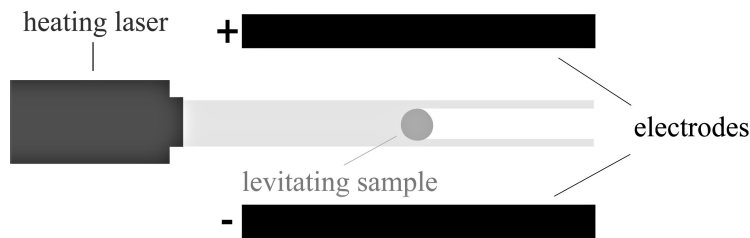


Figure 2.3: Schematic sketch of electrostatic levitation, where the negatively charged sample is levitates through the electrostatic field of the electrodes. Heating is maintained by laser radiation.

Experimental difficulties are primary connected to positing instabilities through charge losses of the sample. One advantage of ESL is the absence of electrohydrodynamic flow, which is driven by the *Lorentz force* for EML. Therefore, the strength of the fluid flow is in general decreased, whereas *Marangoni convection* gives the major contribution to the residual flow. At  $\mu\text{g}$ -ESL buoyancy driven segregation effects are also suppressed. [16] A detailed description of the ESL technique is given in the publication of *Paradis et al.* [15].

## 2.3 Oscillating drop technique

The deviation ( $\delta R_0$ ) of the ideal spherical shape of a levitating, wobbling and liquid sample can be expressed in terms of spherical harmonics of all orders  $l$  and degrees  $m$ , according to Equation 2.3.  $a_{l,m}(t)$  are the time ( $t$ ) dependent coefficients of the spherical harmonics  $Y_m^l(\theta, \phi)$ , which are functions of the polar angle  $\theta$  and the azimuthal angle  $\phi$ .

## 2 Introduction

$$\delta R_0(\theta, \phi, t) = \sum_{l \geq 0} \sum_{m=-l}^{m=+l} a_{l,m}(t) Y_m^l(\theta, \phi) \quad (2.3)$$

The surface deformation of a sample material is directly connected to its surface tension, which acts as a restoring force on the surface elements. In 1879, *Lord Rayleigh* [17] derived the dependence of the prevailing surface oscillation frequencies on the surface tension of the liquid drop, which holds the limitations of perfect sphericity and the absence of external forces and rotation.

$$\omega_{l,m}^2 = l(l+2)(l-1) \frac{4\pi}{3} \frac{\gamma}{M} \quad (2.4)$$

$l$	...	order of spherical harmonics	$\gamma$	...	surface tension / $\text{N} \cdot \text{m}^{-1}$
$m$	...	degree of spherical harmonics	$M$	...	mass / kg
$\omega_{l,m}$	...	angular frequency of $l,m$ -mode / $\text{rad} \cdot \text{s}^{-1}$			

Equation 2.4 gives the general description of the problem, but the fundamental frequency is described by the order  $l = 2$  of the spherical harmonics, as constant changes in the radius ( $l = 0$ ) and translational motion ( $l = 1$ ) do not contribute to surface oscillations. Frequencies of orders  $l > 2$  are in general not used for the description of the problem as assignment rules would increase in complexity and as damping is increased in comparison to the  $l = 2$  modes. Equation 2.5, namely *Rayleigh equation*, describes the behaviour in microgravity ( $\mu\text{g}$ ) well, why it is used at  $\mu\text{g}$ -EML and  $\mu\text{g}$ -ESL until today. The formula holds a five-fold degeneracy in the degree  $m$  of the spherical harmonics, hence only one peak is expected in the frequency spectrum. This frequency is denoted as Rayleigh frequency  $\omega_R$ .

$$\omega_R^2 = \omega_{l=2,m}^2 = \frac{32\pi}{3} \frac{\gamma}{M} \quad (2.5)$$

For processing in an EML apparatus at terrestrial conditions the *Rayleigh equation* is not valid any more, as the restoring forces acting on the surface elements may be influenced by the electromagnetic field or the internal fluid convection. Furthermore, rotation is arising and the external forces of terrestrial gravity and the positioning force, which additionally deform

### 2.3 Oscillating drop technique

the sample from ideal sphericity, cannot be neglected [3]. Non-rotating, terrestrial liquid drops hold a degeneracy of the  $\pm m$ -modes, which are further denoted as  $|m|$ -modes, so only three peaks appear in the spectrum of oscillation frequencies. When rotation occurs, all degeneracies are removed and five oscillation frequencies are obtained. In 1984, *Busse* [18] analysed the behaviour of liquid, rotating drops and found that the emerging splitting of the  $\pm m$ -modes through rotation is symmetric around the non-rotating frequency of the  $|m|$ -mode, proportional to the rotational frequency  $\Omega_{\text{rot}}$  and the degree  $m$  itself, as described in Equation 2.6.

$$\omega_{2,\pm m} = \omega_{2,|m|} \pm \frac{m}{2}\Omega_{\text{rot}} \quad (2.6)$$

So the rotation-free frequency  $\omega_{2,|m|}$  can be expressed by the corresponding rotational frequencies  $\omega_{2,\pm m}$  according to Equation 2.7

$$\omega_{2,|m|} = \frac{1}{2}(\omega_{2,-m} + \omega_{2,+m}) \quad (2.7)$$

In 1991, *Cummings and Blackburn* [3] took the non-vanishing external forces with the resulting effects of drop asphericity as well as the contribution to the restoring forces into account in order to derive a correction term of  $\omega_R^2$  for Equation 2.5 in the form of Equation 2.8. The first term  $f(\omega_{l=2})$  depends on the oscillation frequencies of order  $l = 2$  and the second one,  $g(F_{\text{external}})$ , acts as correction term due to the external forces.

$$\text{general form:} \quad \omega_R^2 = f(\omega_{l=2}) + g(F_{\text{external}}) \quad (2.8)$$

In Equation 2.9, *Cummings and Blackburn* introduced a solution of the term  $f(\omega_{l=2})$  for non rotating samples, which exhibit the three oscillation frequencies of order  $m = 0, |1|$  and  $|2|$ . By additionally applying Equation 2.7, this formula can also be used for rotating drops, but this requires an assignment of all five  $m$ -modes (see Section 3.2.5 for employing the "assigned (A) method"). At assignment difficulties Equation 2.10 gives the upper limit of the resulting surface tension from quadratically summing all five

## 2 Introduction

appearing frequencies of the fundamental oscillation mode. This method will be further termed as "unassigned (UA) method".

$$\text{assigned (A):} \quad f(\omega_{l=2}) = \frac{1}{5}(\omega_{2,0} + 2\omega_{2,|1|} + \omega_{2,|2|}) \quad (2.9)$$

$$\text{unassigned (UA):} \quad f(\omega_{l=2}) = \frac{1}{5} \sum_{m=-2}^{+2} \omega_{2,m} \quad (\text{upper limit}) \quad (2.10)$$

In the term  $g(F_{\text{external}})$  of Equation 2.8, the magnetic field that is generated by the levitation coil setup is approximated better linearly (Equation 2.11<sup>1</sup>) than constantly (Equation 2.12<sup>2</sup>) in vertical direction.

$$\text{linear } B_z: \quad g(F_{\text{external}}) = -\overline{\omega_\tau^2} \left( 1.9 + 1.2 \left( \frac{z_0}{a} \right)^2 \right) \quad (2.11)$$

$$\text{constant } B_z: \quad g(F_{\text{external}}) = -2\overline{\omega_\tau^2} \quad (2.12)$$

$$\text{with} \quad \overline{\omega_\tau^2} = \overline{\omega_{1,m}^2} = \frac{1}{3} \sum_{i=1}^3 \omega_{\tau,i}^2 \quad \text{and} \quad z_0 = \frac{g}{2\overline{\omega_\tau^2}}$$

- $\overline{\omega_\tau^2}$  ... mean square of translational frequencies in x, y and z-direction / Hz<sup>2</sup>  
 $g$  ... gravitational acceleration (9.806 65 m · s<sup>-2</sup> from [10])  
 $a$  ... drop radius at ideal sphericity / m

If the assignment of the oscillation frequencies is not feasible and the magnetic field in vertical direction is approximated as constant, minimum and maximum values for the surface tension of a non-rotating drop can be determined (based on the Equations 2.10 and 2.12) through Equation 2.13<sup>3</sup>. This formula is not state-of-the-art, but has been used in the literature in previous times. As later a comparison of nickel surface tension literature

<sup>1</sup>as in *Cummings and Blackburn* [3]: Equation (5.20)

<sup>2</sup>as in *Cummings and Blackburn* [3]: Equation (6.1)

<sup>3</sup>as in *Cummings and Blackburn* [3]: Equation (6.3)

### 2.3 Oscillating drop technique

among the *Oscillating Drop* evaluation formulas is performed, the formula has to be stated.

$$\omega_R^2 = \frac{1}{10}(3\omega_{\max}^2 + 3\omega_{\min}^2 + 4\omega_{\text{middle}}^2) - 2\overline{\omega_\tau^2} \pm \frac{1}{10}(\omega_{\max} - \omega_{\min}) \quad (2.13)$$

At the evaluation (Section 3.2.5) it is more practicable to work with frequencies  $\nu_{l,m}$  instead of the angular frequencies/velocities  $\omega_{l,m}$ . Thus frequencies are expressed with  $\nu_{l,m} = \frac{\omega_{l,m}}{2\pi}$  below.

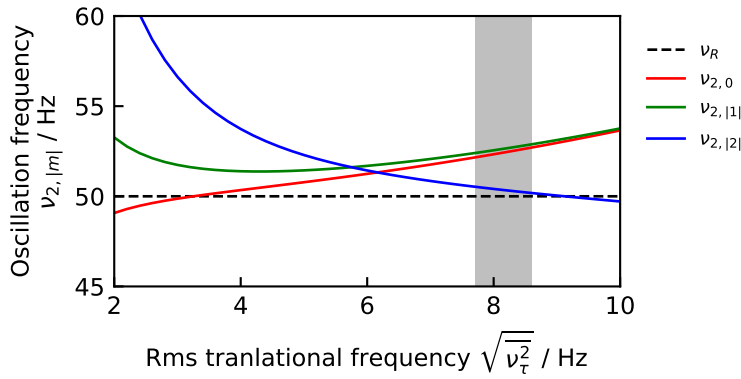


Figure 2.4: Exemplary positions of oscillation frequencies  $\nu_{2,|m|}$  dependent on the rms translational frequencies for a non-rotating nickel drop of 500 mg. The grey area marks the rms translational frequency range emerging at the experiments with nickel.

In Figure 2.4 the oscillation frequencies of a non-rotating, terrestrial drop of liquid nickel with the mass of 500 mg and a Rayleigh frequency of  $\nu_R = 50$  Hz are plotted in dependence of the root mean square (rms) of the translational frequencies. For increasing translational frequencies  $\nu_{2,0}$  and  $\nu_{2,|1|}$  are converging. For a linearly changing magnetic field in vertical direction, the translational frequencies are only connected to the material density and the gradient of the magnetic levitation field, so the relative positions between the  $|m|$ -modes vary for different sample materials and levitation coils [3].

## 2 Introduction

According to *Cummings and Blackburn*, the translational frequencies in the horizontal directions,  $\nu_{\tau,x}$  and  $\nu_{\tau,y}$ , suppose to have the relation displayed in Equation 2.14 to the one in the vertical direction,  $\nu_{\tau,z}$ , at a perfectly linear magnetic field in vertical direction. The deviation of this relation indicates the quality of the levitation coil.

$$\nu_{\tau,z} = 2\nu_{\tau,\text{horizontal}} \quad \text{with } \nu_{\tau,\text{horizontal}} = \nu_{\tau,x} = \nu_{\tau,y} \quad (2.14)$$

**Limitations:** As linear perturbation theory is used for the approaches of *Rayleigh* and *Cummings and Blackburn*, the formulas restrict only to small oscillation amplitudes. Additionally, negative shifts in the resulting Rayleigh frequency appear for finite surface deformation amplitudes, which is discussed more detailed in Section 6.1.1.

For terrestrial ESL the formulas derived by *Cummings and Blackburn* cannot be applied as correction of the Rayleigh frequency, but *Feng and Beard* [19] modelled an equivalent correction formula in 1990. In Equation 2.15 the influence of the finite drop charge on the surface tension is considered. As charge carriers strive for an enlargement of the surface through the repelling Coulomb force of equal charges, surface tension is diminished in total. Finally, the surface tension can be gained only numerically by inserting the characteristic oscillation frequency  $\omega_c$ , which corresponds to the  $\omega_{2,0}$ -mode, as Rayleigh frequency  $\omega_R$  in Equation 2.5.

$$\omega_c^2 = \left(\frac{8\gamma}{a^3\rho}\right)\left[1 - \frac{Q^2}{64\pi^2 a^3 \gamma \epsilon_0}\right][1 - F(\gamma, q, e)] \quad (2.15)$$

$$\text{with } F(\gamma, q, e) = \frac{[243.31\gamma^2 - 63.14q^2\gamma + 1.54q^4]e^2}{176\gamma^3 - 120q^2\gamma^2 + 27\gamma q^4 - 2q^6},$$

$$q^2 = \frac{Q^2}{16\pi^2 a^3 \epsilon_0} \quad \text{and } e^2 = E^2 a \epsilon_0$$

$\gamma$	...	surface tension / $\text{N} \cdot \text{m}^{-1}$	$\epsilon_0$	...	vacuum electric permittivity
$a$	...	drop radius at ideal sphericity / m			$(8.8541878128 \times 10^{-12} \text{F} \cdot \text{m}^{-1})$ from [10]
$\rho$	...	drop density / $\text{kg} \cdot \text{m}^{-3}$	$E$	...	electric field strength / $\text{V} \cdot \text{m}^{-1}$
$Q$	...	drop charge / C			

## 2.4 Pyrometry

A containerless surface tension measurement demands also a contactless temperature acquisition, namely the method of pyrometry. In case of a thermal equilibrium, *Planck's law* (Equation 2.16<sup>4</sup>) enables the assignment of electromagnetic spectra to distinct temperatures of the corresponding black body. Source of physical constants: [10]

$$\text{Planck's law: } L_{\lambda,B}(\lambda, T) = \frac{2c^2h}{\lambda^5} \frac{1}{\exp\left(\frac{ch}{k\lambda T}\right) - 1} \quad (2.16)$$

$L_{\lambda,B}$	...	spectral radiance / $\text{W} \cdot \text{sr}^{-1} \cdot \text{m}^{-3}$	$c$	...	speed of light in vacuum ( $299\,792\,458 \text{ m} \cdot \text{s}^{-1}$ )
$\lambda$	...	wavelength / m	$h$	...	Planck constant ( $6.626\,070\,15 \times 10^{-34} \text{ J} \cdot \text{Hz}^{-1}$ )
$T$	...	temperature / K	$k$	...	Boltzmann constant ( $1.380\,649 \times 10^{-23} \text{ J} \cdot \text{K}^{-1}$ )

The theoretical construct of a *black body* exhibits per definition the highest possible and angular isotropic absorbance and emissivity<sup>5</sup> values of 1. The corresponding surface elements radiate diffusively according to Lambert's cosine law and the radiation is non-polarised. In contrast, *real bodies* feature wavelength and temperature dependent absorbances and emissivities in general smaller than 1. *Real bodies* can further be separated into *grey* and *non-grey bodies*. The absorbance and emissivity of grey bodies is wavelength and temperature independent, which is not the case for *non-grey bodies*. Liquid metals can be typically classified as the latter, holding low emissivity values.

If the emissivity  $\epsilon$  is known, the measured spectrum of a real body can be assigned to a fictive black body temperature  $T_B$ . From that the real temperature can be calculated by Equation 2.18, which is based on Equation 2.17 and *Kirchhoff's law*, that states the equality of the material quantities absorbance  $\alpha(\lambda, T)$  and emissivity  $\epsilon(\lambda, T)$ . [20]

<sup>4</sup>taken from *Henning* [20] as well as the following equations from the pyrometry section

<sup>5</sup>In this thesis the quantity of emissivity is always referred to the normal spectral emissivity.

## 2 Introduction

$$L_{\lambda}(\lambda, T) = \alpha(\lambda, T)L_{\lambda,B}(\lambda, T) \quad (2.17)$$

$L_{\lambda}$	...	spectral radiance of real body / $\text{W} \cdot \text{sr}^{-1} \cdot \text{m}^{-3}$
$L_{\lambda,B}$	...	spectral radiance of black body / $\text{W} \cdot \text{sr}^{-1} \cdot \text{m}^{-3}$
$\alpha$	...	normal spectral absorbance / a.u.
$\lambda$	...	wavelength / m
$T$	...	temperature / K

The corresponding spectral radiances are further expressed by *Planck's law* and partially approximated by *Wien's law* [20]. Source of physical constants: [10]

$$\frac{1}{T} = \frac{1}{T_B} - \frac{k\lambda}{hc} \ln\left(\frac{1}{\epsilon(\lambda, T)}\right) \quad (2.18)$$

$T$	...	real temperature / K	$c$	...	speed of light in vacuum ( $299\,792\,458 \text{ m} \cdot \text{s}^{-1}$ )
$T_B$	...	black body temperature / K	$h$	...	Planck constant ( $6.626\,070\,15 \times 10^{-34} \text{ J} \cdot \text{Hz}^{-1}$ )
$\lambda$	...	wavelength / m	$k$	...	Boltzmann constant ( $1.380\,649 \times 10^{-23} \text{ J} \cdot \text{K}^{-1}$ )
$\epsilon$	...	normal spectral emissivity / a.u.			

As the wavelength and temperature dependent emissivity is widely unknown for liquid metals and alloys, especially for different wavelengths, it is assumed to be fairly steady for temperature alterations at liquid phase. Thus emissivity calibration is performed using phase transition temperatures, as melting temperature for metals and solidus or liquidus temperatures for alloys, in Equation 2.18. A more detailed description of temperature acquisition at the used EML setup can be found in Sections 3.1.3 and 3.2.3.

# 3 Experimental

## 3.1 Setup of the EML apparatus

In Figure 3.1 a schematic sketch of the experimental setup of the *Thermophysics and Metalphysics Group at Institute of Experimental Physics (IEP), Graz University of Technology* is depicted.

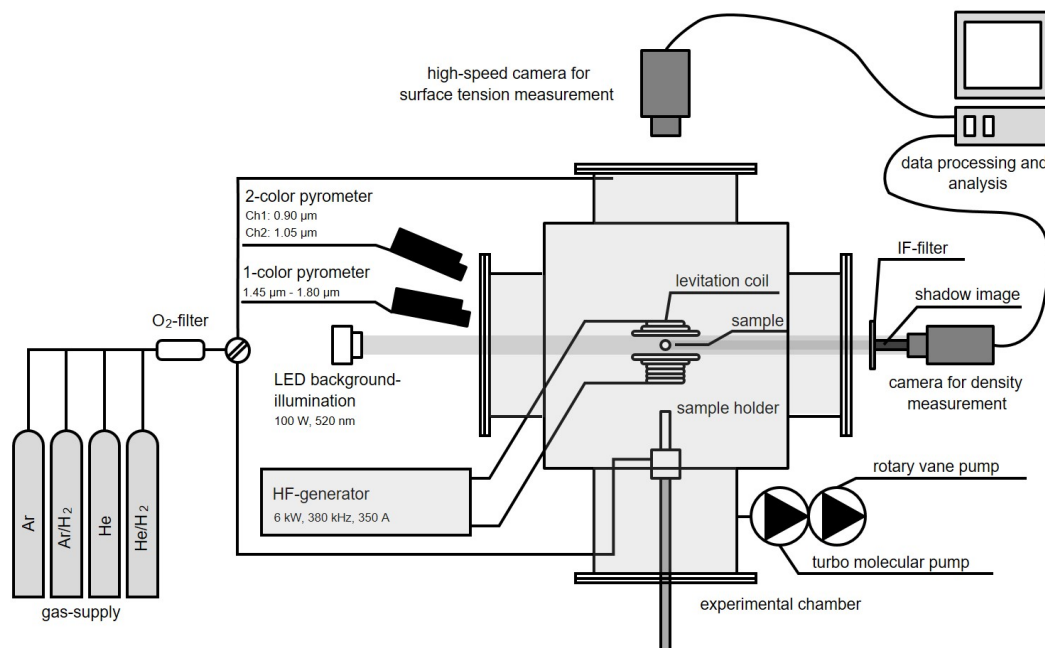


Figure 3.1: Schematic setup of the EML apparatus of *Graz University of Technology*. Figure adapted by Thomas Leitner from [21].

The main parts of the setup are the oscillation circuit for levitation and heating, the videometry for surface tension and density measurements, the

## 3 Experimental

pyrometric unit for temperature acquisition and the evacuation-/pressure-regulation-system in combination with a subset of inert gases for achieving an ideal levitation atmosphere and sample temperature controlling. An overview of every of these parts is given in the next subsections. For further details regarding setup, equipment list and experimentation procedure, reference is made to the PhD theses of Krimanij Aziz [21] and Alexander Schmon [22] and the master theses of Thomas Leitner [23] and Olivia Klemmer [24].

### 3.1.1 Oscillation circuit

The experimental chamber contains the levitation coil that is electrically connected by the vacuum feedthrough with the external elements of the oscillation circuit, namely capacitors and an additional inductance. The external inductance is tunable due to multiple taps and the total capacity can be adjusted by number, choice and type of interconnection (serial, parallel) of capacitors. Hence, the resonance frequency  $f_0$  of the circuit, which is a predominating factor for sample heating, can be altered by a change in this setup as it only depends on the total capacity  $C$  and the total inductance  $L$  regarding to Equation 3.1, which has been derived by William Thomson in 1853.

$$f_0 = \frac{1}{2\pi\sqrt{LC}} \quad (3.1)$$

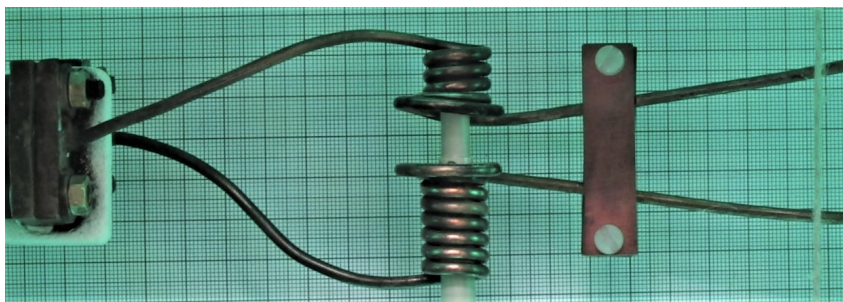
Power up to 6 kW is coupled into the oscillation circuit by a high frequency generator<sup>1</sup>, which exhibits a power control by means of pulse-length modulation with a duty cycle of 144 Hz [23]. The high amperage requires cooling-water lines of the levitation coil, the external LC components and the HF generator. As positioning and heating of the sample is not decoupled, the temperature can only be practicable controlled by heat transfer induced cooling with the surrounding gas atmosphere of the experimental chamber.

---

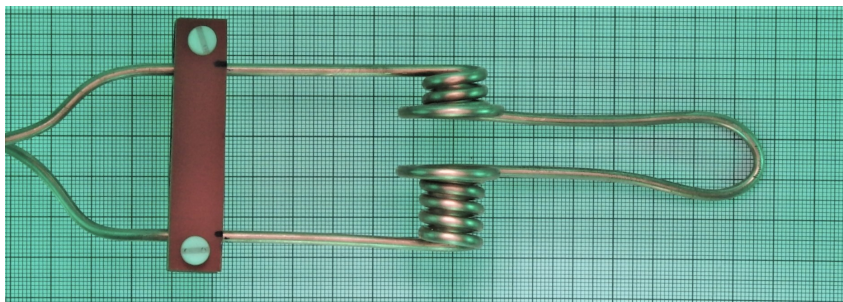
<sup>1</sup>IG 5/200HY from TRUMPF HÜTTINGER GMBH + Co. KG

### 3.1 Setup of the EML apparatus

While performing measurements for this thesis, two hand-manufactured levitation coils depicted in Figure 3.2 were used. The first one was installed for two years until the breakdown in January 2019, which was after the completion of investigating the steel  $W_{360}$ . The geometry of the previous coil has been adopted to the new one, including the distance between upper and lower coils of 12 mm, but less windings have been used in the upper and lower part. In total an increase in symmetry has been achieved by using a coil form. Special attention has been paid to align the coil as accurate as possible along the vertical direction. The entire nickel study has been performed with this coil, where mostly an oscillation frequency of 350 kHz was used.



(a) prior levitation coil: 2017/01 - 2019/01, investigation of  $W_{360}$



(b) actual levitation coil: 2019/02 - now, investigation of nickel

Figure 3.2: Levitation coils used for measurements. The coils have been hand-manufactured by use of a hollow conductor out of copper, which is water-cooled during experimentation. Both figures are displayed at comparable scale.

### 3 Experimental

#### 3.1.2 Pumping system

To achieve low oxygen partial pressures (see Section 6.1.1 for estimation), the experimental chamber has to be evacuated to a pressure in the ( $1 \times 10^{-6}$  to  $1 \times 10^{-5}$ ) mbar regime, which corresponds to the *high vacuum* level. In Figure 3.3 a schematic sketch of the evacuation and pressure regulation system is depicted.

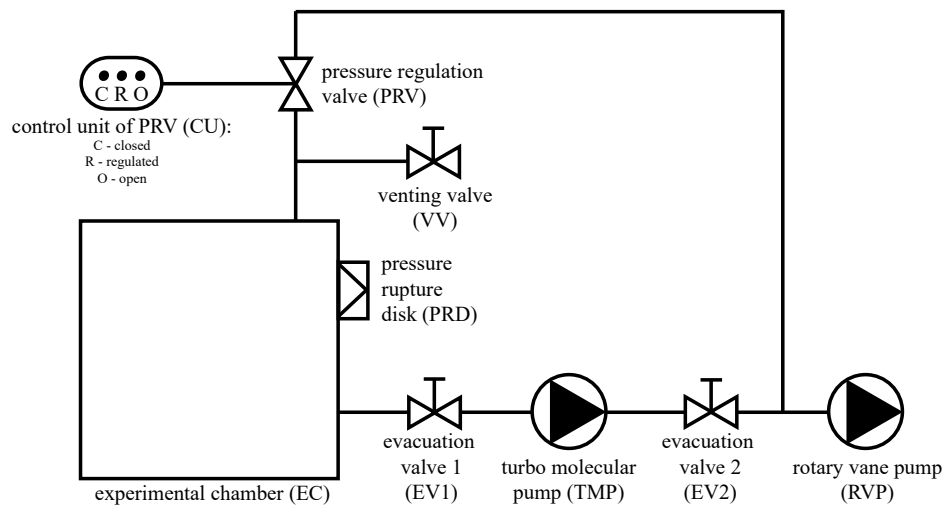


Figure 3.3: Schematic sketch of the pumping and pressure regulation system.

The system consists of two main branches. The first one is used only for the initial evacuation by using a rotary vane pump<sup>2</sup> (RVP) and a turbo molecular pump<sup>3</sup> (TMP). The main task of the second branch, which is serving as bypass, is the pressure regulation during the experiment. After the final evacuation the valves of the first branches, EV1 and EV2, are closed and the turbo molecular pump is shut down. The pressure regulation valve is set to *regulated*, in order ensure the opening of the valve only for pressures close to overpressures (above 850 mbar). Then the filling gas is streamed into the experimental chamber until the desired experimental pressure is reached,

<sup>2</sup>Pfeiffer Balzers Duo 0016B from PFEIFFER VACUUM GMBH

<sup>3</sup>Pfeiffer Balzers TPU 330 from PFEIFFER VACUUM GMBH

### 3.1 Setup of the EML apparatus

which is in the region of (250 to 850) mbar. Below 250 mbar and sometimes even at higher pressures (depending on the composition of the atmosphere) sparkovers may arise due to the high electric field strengths of the feed lines and the coils. In case of a failure of the PRV in the *regulated* mode or a nevertheless increasing chamber pressure, the pressure rupture disk bursts at about 2 bar and saves the experimenter from exploding components.

#### 3.1.3 Temperature acquisition

For a contactless temperature monitoring during experimentation, the method of pyrometry is used, which is shortly described in Section 2.4. Two pyrometers with different working principles are simultaneously employed. Their characteristic parameter are summed in Table 3.1.

Table 3.1: Characteristic data of the pyrometric devices according to datasheets [25, 26]

Type	IMPAC IGA 6 Advanced	IMPAC ISR 6-TI Advanced
Channel-1- wavelength	(1.45 to 1.8) $\mu\text{m}$	0.9 $\mu\text{m}$
Channel-2- wavelength	-	1.05 $\mu\text{m}$
Temperature range	(250 to 2500) $^{\circ}\text{C}$	(700 to 1800) $^{\circ}\text{C}$
Response time	120 $\mu\text{s}$	2 ms
Spot diameter at 210 mm	0.6 mm	1.1 mm
Uncertainty	$\leq 1500\text{ }^{\circ}\text{C}$ : 0.3 % or + 2 $^{\circ}\text{C}$	
	$> 1500\text{ }^{\circ}\text{C}$ : 0.6 %	

### 3 Experimental

The 1-colour-pyrometer *Impac IGA 6* from LUMASENSE is set to emissivity values of a *black body* ( $\epsilon = 1$ ) and is later used for temperature calibration. The second one is the 2-colour-pyrometer *ISR 6-TI Advanced* from LUMASENSE, also named quotient-pyrometer as heat radiation is measured in two neighboured bandwidths so that their emissivities are assumed to exhibit a high similarity at the same temperature. As a consequence the temperature can be assigned to the quotient of these two signals since the quotient of the emissivities can be approximated to 1. This method does not enable measuring true temperatures on spot, but gives temperature readings that hold smaller deviations from the real temperatures than for 1-colour-pyrometers. Temperature calibration may also be performed for the quotient-pyrometer, which has not been done at this work. The spot size diameters at the approximate measuring distance of 210 mm are 0.6 mm (1-colour-pyrometer) and 1.1 mm (2-colour-pyrometer). For a standard nickel sample of 500 mg and a diameter of about 5 mm the spots cover about 12 % and 22 % of the sample diameter respectively.

#### 3.1.4 Levitation atmosphere

As already mentioned in the pressure regulation section, experimentation at pressures below 250 mbar increases the likelihood for the occurrence of flash-arcs or glow discharges. So a levitation atmosphere of inert gases is established between pressure range of (250 to 850) mbar. For experiments of this thesis three different gases, namely high purity argon<sup>4</sup>, *ARCAL 10*<sup>5</sup> and a *custom gas mixture* containing high purity helium<sup>6</sup> with a hydrogen<sup>7</sup> admixture of a volume fraction of 3.83 %, have been used.

There are two different gas inlets in the experimental chamber - one allows streaming the sample from below through the specimen holder and the other

---

<sup>4</sup>*Alphagaz*<sup>TM1</sup> Ar [27] from AIR LIQUIDE: Ar  $\geq 99.999$  mol%  
impurities in ppm-mol: H<sub>2</sub>O  $\leq 2$ , O<sub>2</sub>  $\leq 2$ , KW  $\leq 0.2$ , CO<sub>2</sub>  $\leq 0.2$ , N<sub>2</sub>  $\leq 5$

<sup>5</sup>*ARCAL 10* [28] from AIR LIQUIDE: (2.4  $\pm$  0.5) % H<sub>2</sub> in Ar  
impurities in ppmv: H<sub>2</sub>O  $\leq 40$ , O<sub>2</sub>  $\leq 20$ , N<sub>2</sub>  $\leq 80$

<sup>6</sup>*Alphagaz*<sup>TM1</sup> He [29] from AIR LIQUIDE: He  $\geq 99.999$  mol%  
impurities in ppm-mol: H<sub>2</sub>O  $\leq 2$ , O<sub>2</sub>  $\leq 2$ , KW  $\leq 0.2$ , N<sub>2</sub>  $\leq 5$

<sup>7</sup>*Alphagaz*<sup>TM1</sup> H<sub>2</sub> [30] from AIR LIQUIDE: H<sub>2</sub>  $\geq 99.999$  mol%  
impurities in ppm-mol: H<sub>2</sub>O  $\leq 2$ , O<sub>2</sub>  $\leq 2$ , KW  $\leq 0.1$ , CO  $\leq 0.1$ , CO<sub>2</sub>  $\leq 0.1$ , N<sub>2</sub>  $\leq 5$

### 3.1 Setup of the EML apparatus

inlet is situated at the top of the experimental chamber, far away from the sample and is used for a general flooding of the experimental chamber. The built-in mass flow controller enables a reproducible and precise controlling of the flooding and therefore also temperature regulation, whereas the pressure regulation unit (described in the pressure section) prevents reaching pressures over the defined setpoint of 850 mbar.

The levitation atmosphere has three different functions:

1. **Temperature control:** As the effects of positioning and heating at an EML coil are not decoupled, power reduction of the LC circuit cannot be used for regulation of the sample temperature. Hence, mostly the maximal possible power is coupled into the sample, so that temperature is only controlled by variation in convective cooling. Heat dissipation can either be realized by the unpracticable and time-intensive method of decreasing the pressure of the experimental chamber, which functions only in a very limited temperature range, or by streaming the sample from below to obtain an elevated heat convection. In general noble gases with high specific heat capacities, as well as high thermal conductivities, are desired for an effective cooling process. Therefore the one-atomic noble gases argon and helium have been chosen in this case. Despite their equal molar heat capacities, helium exhibits a higher specific heat capacity than argon due to the lower mass, so helium has a higher cooling efficiency (see Table 3.2). Hydrogen exhibits an even higher specific heat capacity, but can only be applied below a volume fraction of 4 % due to risk of explosion or inflammation. The actual reason for hydrogen admixtures is stated in the next point.

Table 3.2: Specific ( $c_p$ ) and molar ( $c_{p,m}$ ) heat capacities of argon, hydrogen and helium at constant pressure [31]

Gas	$c_p / \text{J} \cdot \text{g}^{-1} \cdot \text{K}^{-1}$	$c_{p,m} / \text{J} \cdot \text{mol}^{-1} \cdot \text{K}^{-1}$
Ar	0.520	20.786
H	14.304	28.836
He	5.193	20.786

### 3 Experimental

2. **Protective and reducing surrounding:** Due to the increased reactivity of high temperature metallic melts, the levitation atmosphere should not contain any reactants influencing the surface tension measurements counterproductively. For this reason, noble gases have been chosen to build a protective surrounding for levitation. However, attention must be drawn to impurities of inert gases, as surfactants like oxygen or sulphur may infiltrate in this way. But those surfactants can already be present in samples from production, which accumulate on the surface when the liquid phase is reached due to their low surface tension. To decrease the formation of oxides on the surface, a hydrogen admixture is deployed for the reduction of oxygen by hydrogen to water. Additionally, samples can be purified by overheating as volatile oxides are forming then [32].
  
3. **Evaporation diminishing:** Operation at nearly atmospheric pressures reduces sample evaporation rates because the surrounding atmosphere acts like a confinement. Despite of that, sample evaporation is not totally negligible. It depends also on the vapour pressure of the material or alloy components as well as on the surface-volume-ratio of the sample. Until now no theoretical mass loss model for EML has been derived, but Thomas Leitner introduced an estimation which depends on measurement time and sample temperature (see Section 6.1.2). ESL has to deal with much higher mass losses during experimentation since operating at far lower pressures in the  $1 \times 10^{-7}$  mbar regime, thus can be theoretically calculated by *Langmuir's equation*. [33]

#### 3.1.5 Videometry

Performing surface tension and density measurements of liquid drops demand non-contact diagnostic tools, namely high speed cameras. For surface tension measurements the levitating drop is monitored from top<sup>8</sup> and for density measurements from the side<sup>9</sup> (see Figure 3.1). In addition

---

<sup>8</sup>Microtron EoSens CL from MICROTRON GMBH

<sup>9</sup>Basler avA1000-120km from BASLER AG

### 3.1 Setup of the EML apparatus

a frame grabber card, kind of an interface between cameras and computer, is built in for enabling high speed live view, general image capturing and additional image processing tools. To increase the contrast and the edge sharpness for density measurements, shadow images are generated through a back lighting of a monochrome LED-panel with a centroid wavelength of 520 nm and an interference filter installed prior to the side camera.

#### 3.1.6 Previous setup modifications and improvements

Since the master thesis of Thomas Leitner [23] two main setup improvements have been gained. The sample carousel, that has been designed by Alexander Höll [34], enables investigating nine samples at a single experiment instead of one. Therefore the levitation chamber has not to be vented and evacuated each time in advance. This is especially beneficial for alloys with components exhibiting a high vapour pressure as levitation time has to be drastically reduced to avoid a relative change of the alloy composition. The second improvement is the installation of a mass flow controller by Florian Kametriser [35] for achieving the desired sample temperature faster and more reproducibly.

In addition, a new current feedthrough for the experimental chamber has been deployed since the former one often caused vacuum leakage. But in turn high attention has to be drawn to the occurrence of glow discharges. They appear more likely at helium based atmospheres than at argon based at fairly same pressures, despite the helium exhibits the highest possible ionisation energy.

## 3.2 Measurement procedure

### 3.2.1 Sample preparation

Each sample has to be treated prior to measurements. The individual treatment depends on the material, initial geometry, sensitivity for oxidation and superficial contamination. If the desired mass and shape for levitation are not provided, a cylindrical shape with a diameter-height-ratio near one is gained through cutting and grinding by means of rotary tools such as *Dremel* or a turning machine. For cleaning the surface from oxides and other contaminants, abrasive paper of different grades is used for polishing. Strong oxidising materials have to be immersed in isopropanol after polishing until inserting to the experimental chamber in order to minimise the contact to air. All samples undergo a treatment in the ultrasonic bath to remove the remaining dust or metal chips, as well as other dirt on the surface.

### 3.2.2 Levitation preparation

Before inserting samples to the experimental chamber, their mass has to be determined by a precision balance<sup>10</sup>. If the maximal nine samples have been placed on the carousel, the evacuation process is started (for further details see Section 3.1.2). It usually takes several hours until the pressure is reduced to the  $10^{-6}$  mbar regime, where the partial pressure<sup>11</sup> of oxygen fairly equals the ones in the filling gases. Accordingly, the chamber is flooded to a level between 250 mbar and 850 mbar, which is the setpoint for reactivating the rotary vane pump as long as this level is exceeded. The filling gases mainly used are a combination of either *ARCAL10* or high purity argon with the custom gas mixture described in Section 3.1.4. If the final pressure and the desired atmospheric composition is accomplished, the sample is directed to the coil centre with help of the vertically displaceable sample holder. In the following, the power of the high frequency generator is increased as far

---

<sup>10</sup>*AB104-S-A* from METTLER TOLEDO: Readability of 0.1 mg, repeatability of 0.1 mg

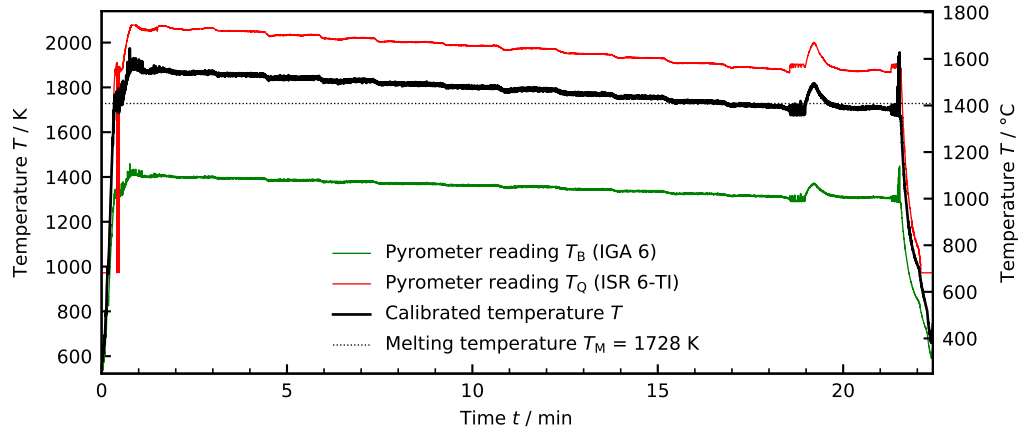
<sup>11</sup>A quantification of the oxygen partial pressures present in the levitation gases is given in Section 6.1.1.

as possible. While the already glowing sample is still in contact with the sample holder, chemical contamination is prevented as the sample holder is machined from a glass ceramic called *MACOR*®. Already before a stable levitation is reached, the sample holder should be brought down to its usual position.

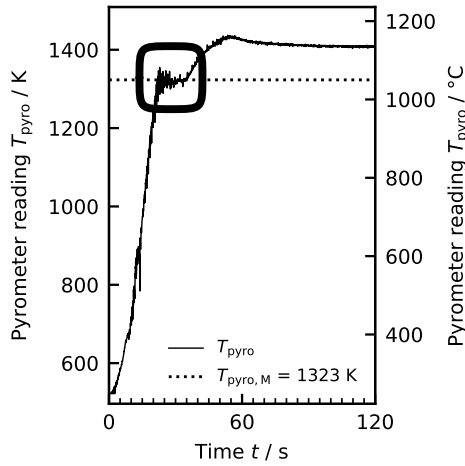
### 3.2.3 Temperature regulation, measurement and calibration

The temperature course of the levitating liquid sample has to be monitored all time, but especially prior measuring surface tension and density a correct focussing on the equator centre of the drop has to be provided for both pyrometers for enabling the determination of normal spectral emissivities. Measurements of surface tension and density are performed at different temperatures. In the end, the accomplished temperature profiles are basically shaped in the form of a decreasing step function. So the sample temperature is consecutively decreased between measurements by convective cooling with the different filling gases, which are inert and partially reducing (Section 3.1.4). Figure 3.4a depicts the comparison of the two different pyrometer readings obtained during measurement and the posteriorly calibrated temperature. Therein, the raw pyrometer reading  $T_B$  denotes the signal from the 1-colour-pyrometer *IMPAC IGA 6 Advanced*, which corresponds to the black temperature, and  $T_Q$  denotes the one of the 2-colour- or quotient-pyrometer *IMPAC ISR 6-TI Advanced*. The temperature calibration is performed on the pyrometer reading of the 1-colour-pyrometer *IMPAC IGA 6 Advanced* after experimentation on one of the two phase changing plateaus, which are plotted in Figures 3.4b and 3.4c. The pyrometer reading of the evaluated plateau (melting plateau:  $T_{\text{pyro},M}$ , solidification plateau:  $T_{\text{pyro},S}$ ) can be matched to the true temperature of the plateau, that is either known from literature or has to be determined externally through other methods, such as DSC (differential scanning calorimetry), etc.. With help of Equation 2.18, the normal spectral emissivity at the plateau can be gained. The decision for choosing almost exclusively the melting (or liquidus) plateau for calibration is discussed in Section 6.1.1. Under the assumption of a constant emissivity in liquid phase, the true temperature can also be computed through Equation 2.18.

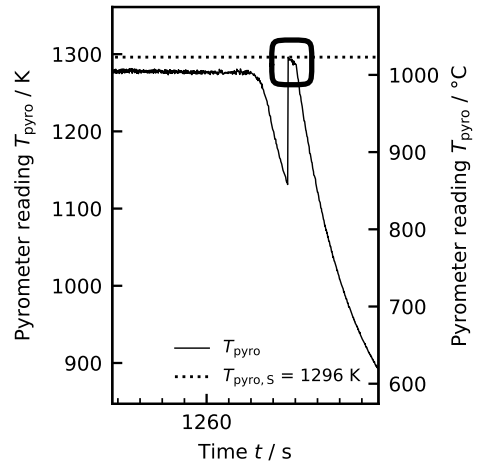
### 3 Experimental



(a) Temperature profile of pyrometer readings and calibrated temperatures (nickel)



(b) Melting plateau (nickel)



(c) Undercooling followed by a short solidification plateau and the effect of recalescence (nickel)

Figure 3.4: Typical temperature profiles and plateaus of nickel: The melting plateau duration is typically on time scales of a few seconds, whereas the solidification process is a comparable short process, which enters after partially strong undercoolings. Solidification is attended by the effect of recalescence, which can be observed by a short flashing of the sample. Both plateaus are marked by a rectangle.

### 3.2.4 Density measurements and evaluation

Density determination in an EML apparatus is a quite practicable additional tool for surface tension measurement, as density information is also required. So, if investigating a novel material where density behaviour in the liquid phase is not known, surface tension can be determined nevertheless.

The density acquisition is based on observing the projection in the  $xz$ -plane of the levitating sample for a sufficiently long time. If this is accomplished, the volume should conform to the spherical integration about the vertical  $z$ -axis of the time-averaged projection. Then easily the density can be calculated with help of the known mass.

Performing edge detection and integration needs some computational effort. Typically 4100 frames<sup>12</sup> are recorded per measurement point at a specific temperature. Sampling rates of 120 frames per seconds (fps) and shutter times of 400  $\mu$ s are used. An exemplary time series of records is depicted in Figure 3.5.

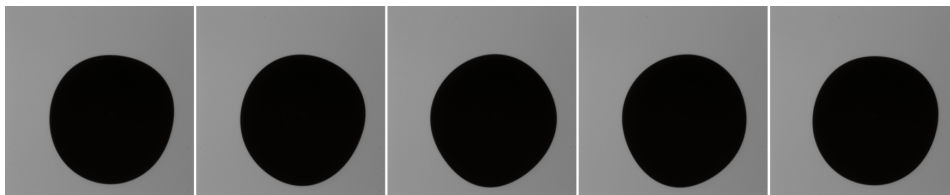


Figure 3.5: Exemplary series of shadow images recorded at density measurement.

The evaluation of a frame starts with identifying the centre of mass (CM) coordinates with a simple threshold based algorithm. From this the edge is detected in  $1^\circ$  steps through finding the point of inflection of a polynomial of 3<sup>rd</sup> order fitted to the line profile starting at CM. All radii and CM coordinates are stored in an ASCII file. An exemplary frame evaluation is shown in Figure 3.6. The gained radii are fitted to *Legendre polynomials* of 6<sup>th</sup> order to allow an analytical integration, which increases accuracy.

---

<sup>12</sup>Investigations of Thomas Leitner have shown that the volume typically converges already after 500 to 2000 frames.

### 3 Experimental

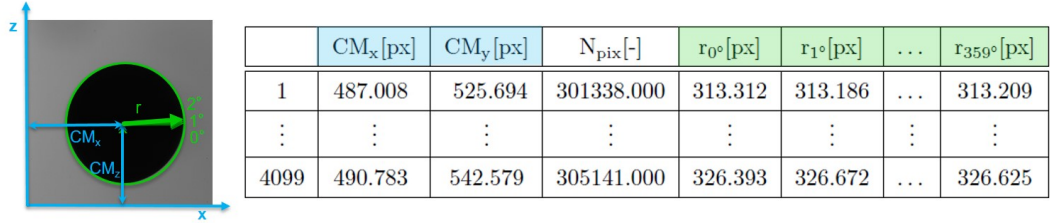


Figure 3.6: Exemplary evaluation of density frame regarding centre of mass coordinates in x- and z-direction (CM<sub>x</sub>, CM<sub>z</sub>), radii in 1° steps (r<sub>α</sub>) and the total number of pixels in the projecting area (N<sub>pix</sub>). Figure is partially adapted from Thomas Leitner [23].

As evaluation until this point is only performed in units of pixels, the pixel-meter-conversion has to be determined. For this reason ball bearings of defined diameter of 4 mm, 5 mm and 6 mm are levitated aerodynamically to also take non linear effects into account<sup>13</sup>.

The density measurement setup and evaluation at *Graz University of Technology* has been designed by Alexander Schmon within the scope of his doctoral thesis [22]. Modifications were performed by Thomas Leitner.

#### Fit equation

The density  $\rho$  of liquid metals is typically stated as linear function of the temperature  $T$ , see Equation 3.2. Therein,  $T_M$  denotes the melting temperature,  $\rho_M$  the density at the melting temperature and  $\frac{\partial \rho}{\partial T}$  the slope of the function, which possesses a negative value basically.

$$\rho(T) = \rho_M + \frac{\partial \rho}{\partial T}(T - T_M) \quad (3.2)$$

For alloys the index L is used instead of M for  $T_M$  and  $\rho_M$  as the liquidus temperature is used as reference point.

<sup>13</sup>Typical sample diameter are  $\leq 5$  mm, so it would make sense using ball bearings with diameters of 3.5 mm and 4.5 mm additionally

### 3.2.5 Surface tension measurements and evaluation

For explaining the method in a few words, it has to be stated that the surface tension of liquid metals is coupled to its surface oscillations. By analysing the oscillation frequencies, surface tension can be estimated using the approach of *Cummings and Blackburn* of Equation 2.8.

#### Measurement

In detail, the wobbling levitating liquid sample is observed with the top camera (Figure 3.1). For a period of about 45 s the projection in the horizontal  $xy$ -plane is recorded with a sampling rate of 300 fps and shutter times of typically 500  $\mu$ s. According to the *Nyquist-Shannon sampling theorem* oscillation frequencies up to 150 Hz can be analysed by this sampling rate. Figure 3.7 presents exemplary series of five sequential records.

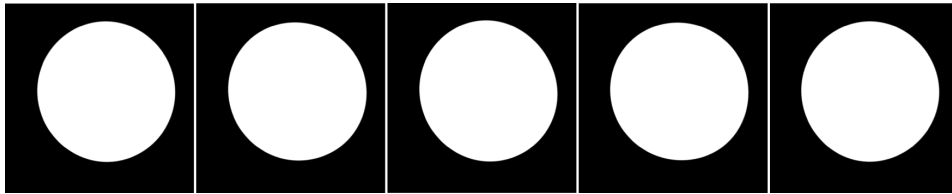


Figure 3.7: Exemplary series of images recorded at surface tension measurement.

#### Frame analysis

Here again, frames are analysed with a threshold-based algorithm to obtain the centre of mass coordinates in  $x$ - and  $y$ -direction ( $CM_x$ ,  $CM_y$ ), but also for determining radii in  $5^\circ$  steps. In comparison to density evaluation, no high accuracy in position is required as the time evolution is more essential for analysis. Consequently information of a whole video can be reduced to a table (stored in an ASCII file), where each row contains data from one frame. The table columns hold the time evolution. A schematic sketch of the evaluation is illustrated in Figure 3.8.

### 3 Experimental

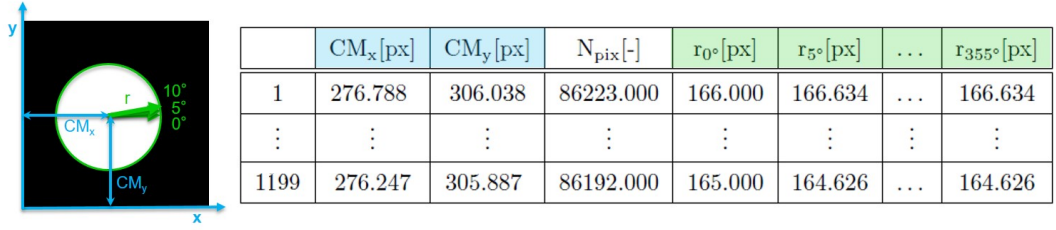


Figure 3.8: Exemplary evaluation of surface tension frame regarding center of mass coordinates in x- and y-direction (CM<sub>x</sub>, CM<sub>y</sub>), radii in 5° steps (r<sub>α</sub>) and the total number of pixels in the projecting area (N<sub>pix</sub>). Figure is partially adapted from Thomas Leitner [23].

### Frequency analysis

Evaluation in this thesis is performed by *Cummings and Blackburn* correction under assumption of a linear changing magnetic field in vertical direction and distinctly assigned oscillation frequencies. The explicit formula is stated in Equation 3.3, which is a combination of Equations 2.5, 2.7, 2.8, 2.9 and 2.11 from the introduction in Section 2.3. Here oscillation frequencies  $\nu$  are used instead of angular velocities  $\omega$  as they are more practicable when evaluating frequency spectra.

$$\gamma = \frac{3\pi}{8} M \left[ \frac{1}{5} \left( \nu_{2,0}^2 + 2\nu_{2,|1|}^2 + \nu_{2,|2|}^2 \right) - \overline{\nu_{\tau}^2} \left( 1.9 + 1.2 \left( \frac{z_0}{a} \right)^2 \right) \right] \quad (3.3)$$

$$\text{with } \nu_{2,|m|} = \frac{1}{2} (\nu_{2,-m} + \nu_{2,+m}) \quad \text{and} \quad z_0 = \frac{g}{8\pi^2 \nu_{\tau}^2}$$

$\gamma$	...	surface tension / N · m <sup>-1</sup>
$M$	...	mass / kg
$\nu_{2,m}$	...	oscillation frequency of fundamental order $l = 2$ and $m$ / Hz
$m$	...	degree of spherical harmonics
$\overline{\nu_{\tau}^2}$	...	mean square of translational frequencies in all directions / Hz
$a$	...	drop radius at ideal sphericity / m
$g$	...	gravitational acceleration (9.80665 m · s <sup>-2</sup> from [10])

### 3.2 Measurement procedure

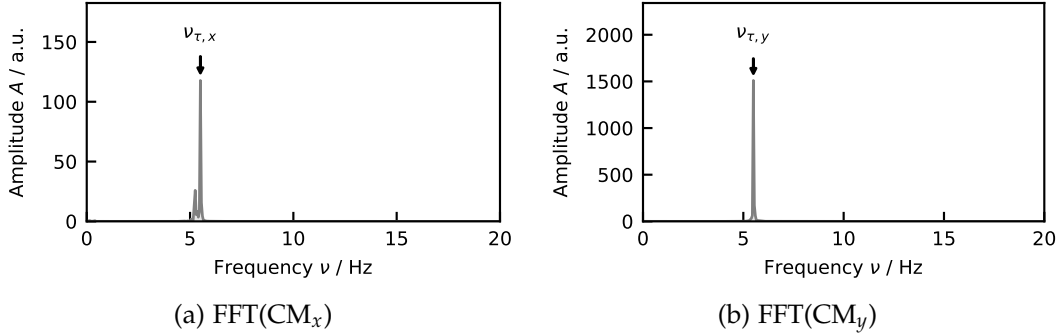


Figure 3.9: Fourier spectra of surface tension image center of mass coordinates in x- and y-direction of nickel.

So in total the mean square of all three translational frequencies  $\overline{\nu_{\tau}^2}$  has to be determined. The one in x- ( $\nu_{\tau,x}$ ) and y-direction ( $\nu_{\tau,y}$ ) can be easily identified by Fourier transforming  $CM_x$  and  $CM_y$ , which is apparent from Figure 3.9.

In contradiction, finding the translational frequency in the vertical z-direction  $\nu_{\tau,z}$  is more time-consuming, as it cannot be directly determined using the EML apparatus at *Graz University of Technology*. This could be realized by additional simultaneous records of the density camera, which views the xz-projection of the sample. However, this functionality is not implemented until now. Alternatively, records with the front camera can be taken after the one of the top camera since  $\nu_{\tau,z}$  is not changing drastically (Figure 3.10b). But due to a small deviation of the observation angle of the top camera to the vertical axis,  $\nu_{\tau,z}$  mostly also appear in the  $CM_x$  and/or  $CM_y$  spectra, as shown in Figure 3.10a. On the basis of experience, it is not trivial to identify  $\nu_{\tau,z}$  in between noise. Therefore it is highly recommended to determine a guiding value through measurement with the density camera and use  $CM_x$  and/or  $CM_y$  spectra for matching the peak in the vicinity of the guiding value. There is also the possibility of estimating  $\nu_{\tau,z}$  according to Equation 2.14 which only requires knowledge of the corresponding  $\nu_{\tau,x}$  and  $\nu_{\tau,y}$  if a linearity along the magnetic field in z-direction is guaranteed. Most of the levitation coils have a finite deviation of this linearity, hence no thoughtless trust should be placed to this formula.

### 3 Experimental

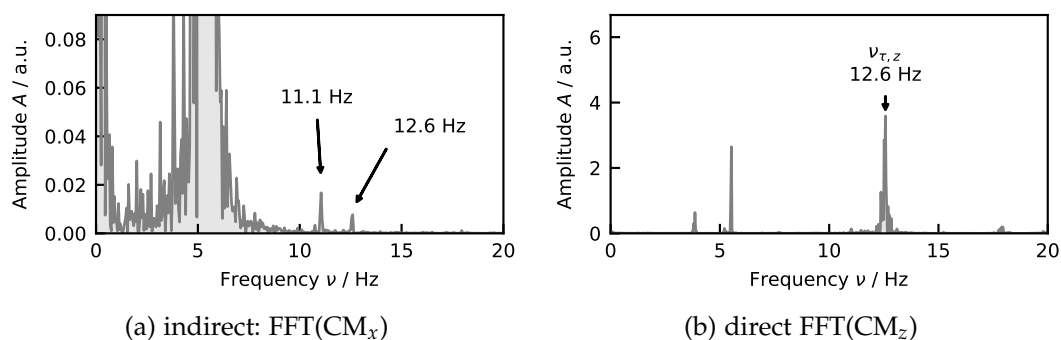


Figure 3.10: Different methods for determination of the translational frequency in  $z$ -direction. Indirect: Via zoomed  $CM_x$  or  $CM_y$  spectra. Direct: Via Fourier spectrum of centre of mass  $z$ -coordinate, which can be obtained through density measurements of the front camera. Spectra from nickel investigation.

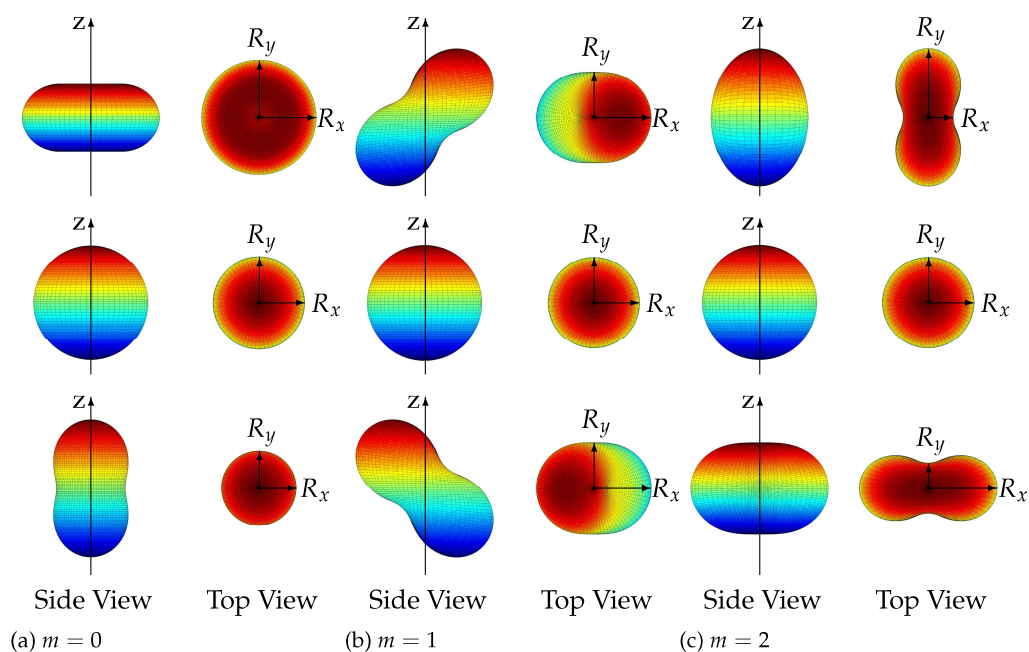


Figure 3.11: Visualisation of oscillation mode projections in  $xy$ - and  $xz$ -plane of fundamental order  $l = 2$  and all three  $m$ -modes. Source: [21]

### 3.2 Measurement procedure

The identification of the oscillation frequencies of the fundamental order ( $l = 2$ ) requires the basic knowledge of the time dependent geometry of the single  $m$ -modes. In Figure 3.11 the projections in the  $xy$ -plane, which are observed by the top camera, as well as the one of the  $xz$ -plane, that is recorded by the density front camera, are visualised.

In general, 72 different oscillation spectra can be created for each measurement through application of a Fourier transform, as time dependent radii have been evaluated for the same number of angles (from  $0^\circ$  to  $355^\circ$  in  $5^\circ$  steps). Exemplary spectra for the arbitrary radii  $\alpha$  and  $\alpha+90^\circ$  are depicted in Figure 3.12. In Figure 3.14, spectra for radii at all evaluated angles are plotted it get an idea of the angle dependence of the oscillation amplitude.

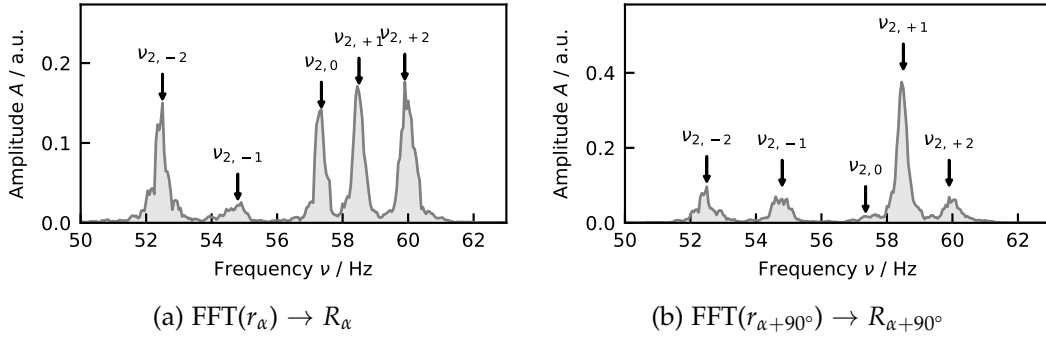


Figure 3.12: Fourier spectra of surface tension image radius at angles  $\alpha$  and  $\alpha+90^\circ$  (nickel).

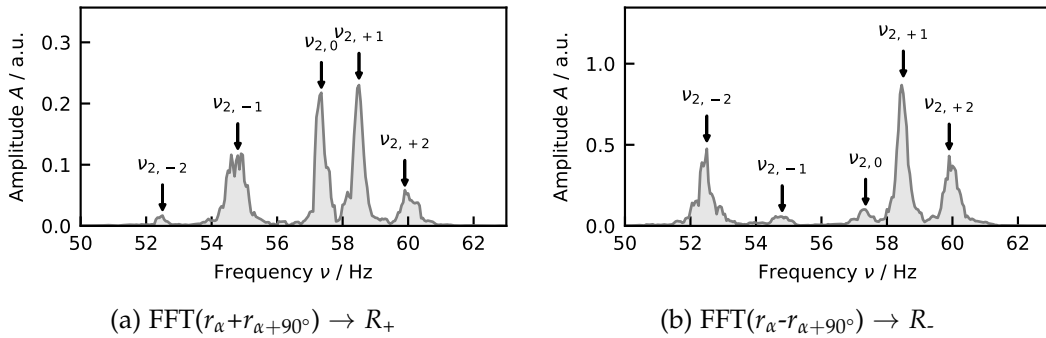


Figure 3.13: Fourier spectra of summed and subtracted surface tension image radius of the angles  $\alpha$  and  $\alpha+90^\circ$  (nickel).

### 3 Experimental

Assignment based on one  $R_\alpha$  spectrum is difficult and not confidential. For this reason specific assignment rules have been established on the appearance of the  $m$ -mode projections in the  $xy$ -plane from Figure 3.11. When building sums or differences of perpendicular radii and Fourier transforming them ( $R_+$ ,  $R_-$  - depicted in Figure 3.13) the following rules are evident:

- $\nu_{l=2,|m|}$ : According Equation 2.7 the splitting of  $|m| = 2$  modes is the double of the  $|m| = 1$  modes.
- $\nu_{l=2,m=0}$ : The  $m = 0$  peak should be only visible in the  $R_+$ -spectrum. It vanishes in the  $R_-$ -spectrum as the sum of two perpendicular radii in the  $xy$ -plane always should give 0, whose Fourier transformation also applies to 0.
- $\nu_{l=2,|m|=1}$ : Neither building sums nor differences of two perpendicular angles will give constant values, so the  $|m| = 1$  modes ought to be present in  $R_{+-}$ , as well as in  $R_-$ -spectrum.
- $\nu_{l=2,|m|=2}$ : It has been proven that the sum of two perpendicular radii gives a constant number for all angles, therefore  $|m| = 2$  modes may not be observable in  $R_+$ -spectrum [21].

In practice, sometimes peaks are visible in spectra even though they should not, as depicted in Figure 3.13. That may occur from slight static sample deformation through the magnetic pressure from the coil or from a  $1^\circ$  to  $3^\circ$  deviation of the observing angle from the vertical direction.

#### Fit equation

The surface tension  $\gamma$  of liquid metals is typically stated as linear function of the temperature  $T$ , see Equation 3.4. Therein,  $T_M$  denotes the melting temperature,  $\gamma_M$  the surface tension at the melting temperature and  $\frac{\partial\gamma}{\partial T}$  the slope of the function, which possesses a negative value basically. For alloys the index L is used instead of M for  $T_M$  and  $\gamma_M$  as the liquidus temperature is used as reference point.

$$\gamma(T) = \gamma_M + \frac{\partial\gamma}{\partial T}(T - T_M) \quad (3.4)$$

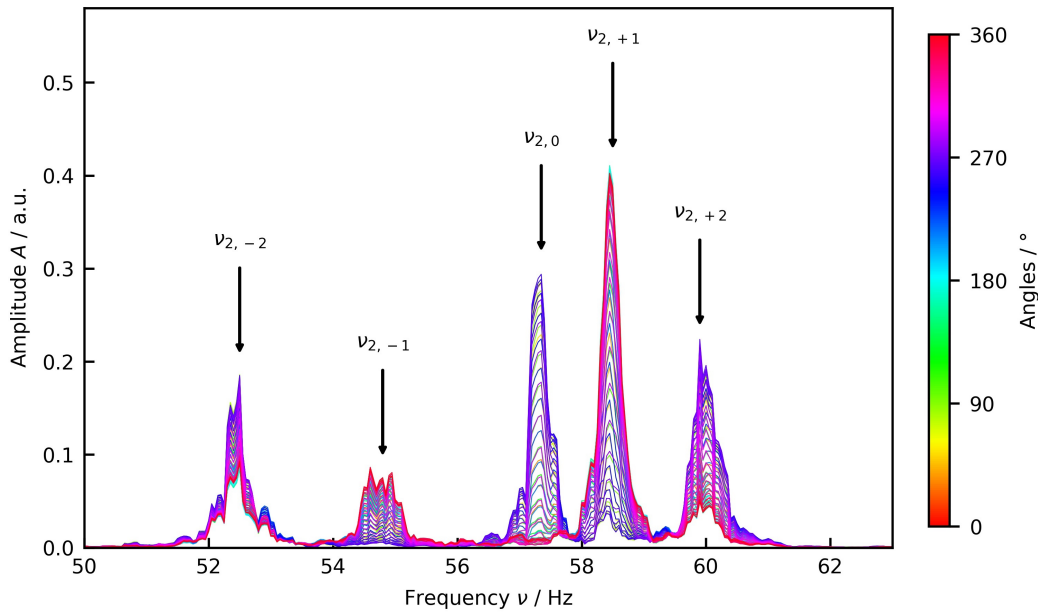


Figure 3.14: Fourier spectra of surface tension image radius at all evaluated angles in  $5^\circ$  steps (nickel).

### Quality aspects

During the work of the master thesis of Olivia Klemmer [24], a noise spectrum of the EML apparatus had been recorded. In the approximated range of (10 to 50) Hz distinct noise peaks occur originated by the pumping system, the cooling device and the fan of the LED panel. Avoiding the generation of oscillation frequencies of the fundamental mode in this range through an optimised choice of sample mass prevents the misidentification of  $l = 2$  peaks caused by erroneous assignment or peak broadening.

As all five  $m$ -mode-frequencies are required for the calculation of the surface tension, all oscillation modes ought to be excited in a noticeable amplitude in the frequency spectrum. When observing visibly translational oscillations in the horizontal plane, the occurrence of explicit peaks in the fundamental mode seems to be correlated. In contrast, for a distinct assignment of the different  $m$ -modes, high rotational frequencies are beneficial to get a severe splitting. The influence of temperature stability and other quantities while measuring is discussed and quantified in Section 6.1.



## 4 W360

The steel *W360* produced by *voestalpine BÖHLER Edelstahl GmbH & Co KG* has been investigated at first. Improvements, that have been discovered at the nickel investigation have not been implemented for this results, but this will be discussed below as well as in Section 6.1.

The typical composition in weight percent (wt%) of the analysed steel *W360* is stated in Table 4.1.

Table 4.1: Typical chemical composition of *W360*. Source: [36]

Steel	Typical chemical composition / wt%						
	Fe	C	Si	Mn	Cr	Mo	V
<i>W360</i>	91.00	0.50	0.20	0.25	4.50	3.00	0.55

### 4.1 Experimental

The sample preparation of *W360* emerged to be quite time-consuming due to the initial block form and the high affinity for oxide formation. Therefore, all *W360* samples had to be polished using an abrasive paper of grade 480 and cleaned in an isopropanol ultrasonic bath before inserting to the vacuum chamber. When omitting polishing, oxide islands could be observed on the levitating sample or even worse, the steel could not be melted at all. In Figure 4.1, samples in all experimental stages are depicted. Therein, the influence of surface oxides is clearly evident for pre (C,D) and post (E,F) levitation samples.

#### 4 W360

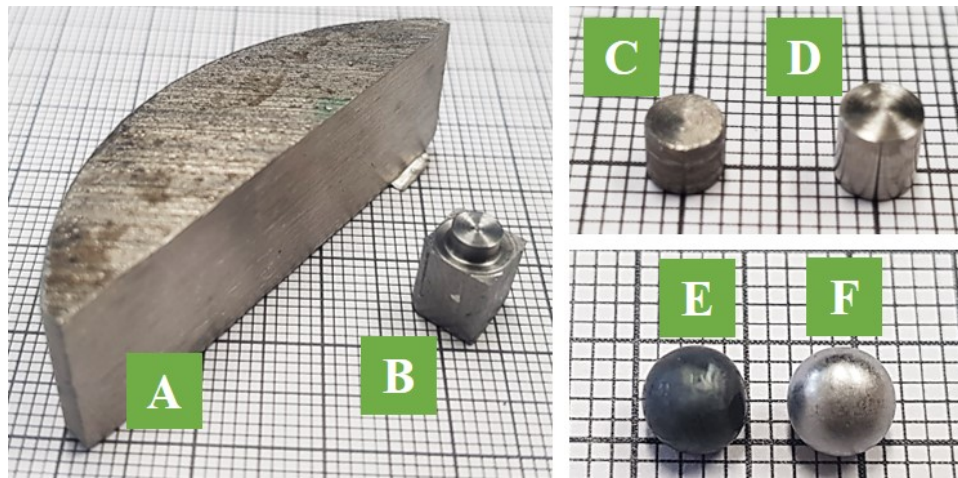


Figure 4.1: *W360* samples in all experimental stages starting from the initial shape as delivered by *BÖHLER* (A). From this block thin cuboids (B) were cut in order to form cylindrical rods by use of a turning machine. Afterwards, small cylindrical samples were cut from the rod (C). The difference in oxide contamination of unpolished (C) and polished (D) samples is obvious. This becomes even more clear for already levitated samples. The one which has been polished before levitation has a shiny surface (F) in comparison to the untreated sample with an apparently darker surface (E). In order to estimate size, samples were placed on millimetre paper.

Liquidus and solidus temperatures obtained through DSC measurements have been provided by *BÖHLER* and are denoted in Table 4.2. Those were used for temperature calibration as explained in Section 3.2.3.

Table 4.2: Liquidus and solidus temperatures of *W360* (from DSC measurements [37]).

$T_L$  ... liquidus temperature / °C or K  
 $T_S$  ... solidus temperature / °C or K

	°C	K
$T_L$	1475.9	1749.1
$T_S$	1385.8	1659.0

The experiments have been carried out under a reducing inert gas atmo-

## 4.1 Experimental

sphere consisting of a combination of *ARCAL 10*<sup>1</sup> (ARCAL) and a *custom gas mixture*<sup>2</sup> (cgm). In Table 4.3 information regarding material and experimentation can be found.

Table 4.3: Information according to specimen mass and experimental parameter

$m_{\text{start}}$	...	mass before levitation / mg
$m_{\text{end}}$	...	mass after levitation / mg
$\Delta m$	...	relative mass loss through levitation / %
$T_{\text{cal,pyro}}$	...	pyrometer reading for further calibration on either $T_{\text{L}}$ or $T_{\text{S}}$ / °C
$N_{\text{D}}$	...	number of density measurements
$N_{\text{S}}$	...	number of surface tension measurements

ID	date	$m_{\text{start}}$	$m_{\text{end}}$	$\Delta m$	atmosphere	$T_{\text{cal,pyro}}$	$N_{\text{D}}$	$N_{\text{S}}$
#1	17.12.2018	428.6	424.0	1.1	ARCAL	$T_{\text{L}} = 1082$	1	1
#2	18.12.2018	420.2	413.6	1.6	ARCAL	$T_{\text{S}} = 1066$	7	7
#3	18.12.2018	435.0	432.8	0.5	ARCAL & cgm	$T_{\text{L}} = 1082$	3	2
#4	14.01.2019	420.1	416.4	0.9	ARCAL & cgm	$T_{\text{L}} = 1078$	6	6
#5	14.01.2019	437.9	436.0	0.4	ARCAL & cgm	$T_{\text{L}} = 1078$	5	4
#6	24.01.2019	421.8	420.0	0.4	ARCAL & cgm	$T_{\text{L}} = 1080$	0	3

Initial sample masses in a small range of  $(430 \pm 20)$  mg have been chosen for experiments due to a sufficient levitation stability. In addition, already for masses  $\geq 500$  mg high surface oscillations are noticeable. In comparison to the later investigated nickel, high mass losses in the range of  $(4 \pm 4)$  mg or  $(0.8 \pm 0.9)$  % have been observed during levitation.

In contrast to the later performed investigation of liquid nickel, the pyrometer reading during a measurement record was manually noted. As the signal is usually changing fast and drifting in the end towards lower regions, the noted value has been just an estimate. Later on for nickel, the pyrometer reading for one particular measurement was already determined directly through the recorded pyrometer signal. So the mean was calculated

<sup>1</sup>ARCAL 10 from AIR LIQUIDE: Ar + 2.4 vol% H<sub>2</sub>

<sup>2</sup>custom gas mixture from AIR LIQUIDE: He + 3.83 vol% H<sub>2</sub>

#### 4 W360

as well as the double standard deviation to estimate the fluctuation range. In addition, the former mass loss model was still in use, that has been enhanced for the investigation of nickel. This is discussed in Section 6.1 in detail.

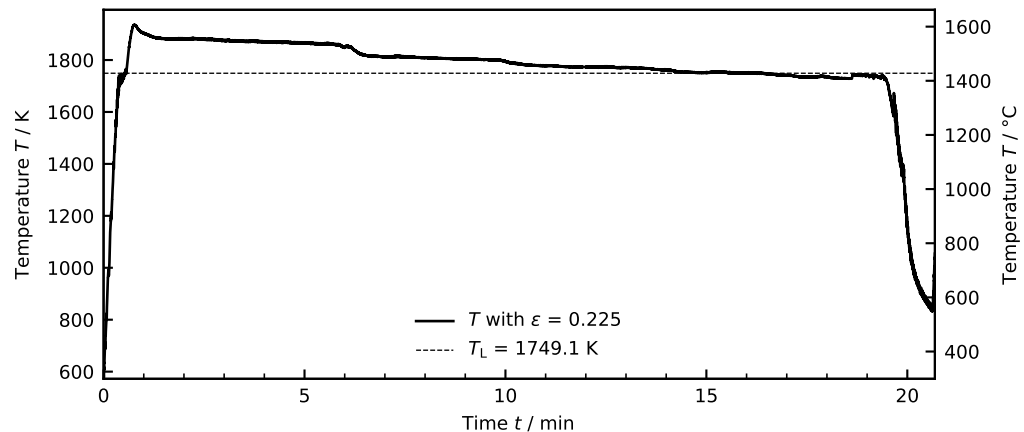
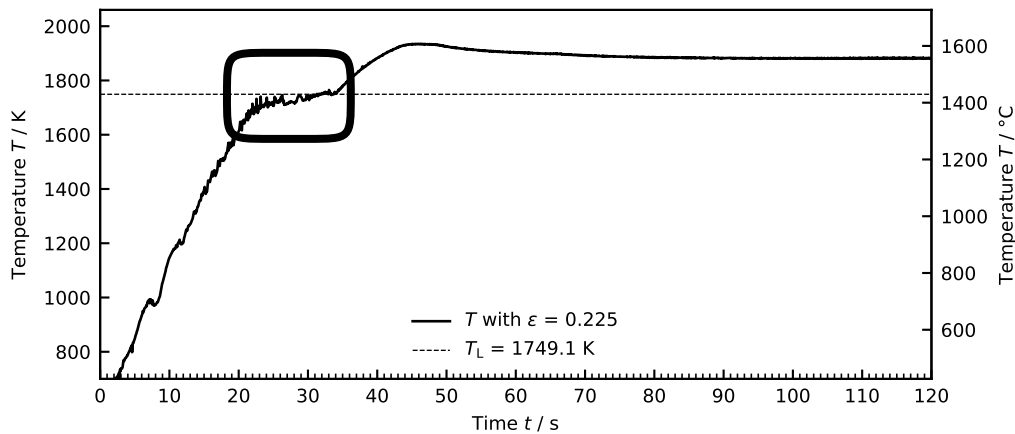


Figure 4.2: Typical temperature profile of W360 at experiment (sample #5 according to Table 4.3). This temperature has been already calibrated on the liquidus plateau at a plateau pyrometer reading of 1078 °C, which gives a normal spectral emissivity  $\epsilon$  of 0.225 at the calibration plateau.

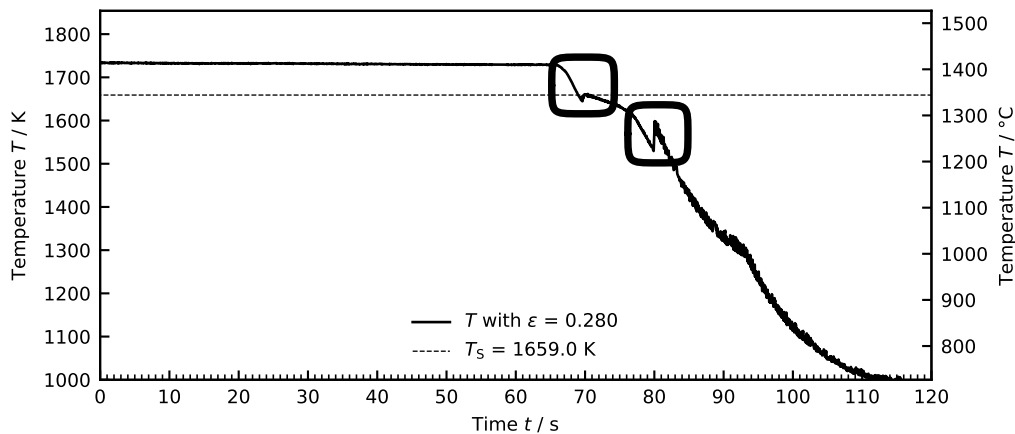
The corresponding plateaus of the pyrometer readings used for calibration are stated in Table 4.3. Specimen #2 was calibrated on the solidus plateau, because the liquidus plateau proceeded so noisy that no evaluation was possible. A typical calibrated temperature profile gained during an experiment is depicted in Figure 4.2. Here, a normal spectral emissivity of 0.225 has been obtained at the calibration plateau. In general, normal spectral emissivities obtained by a calibration on the liquidus plateau are in the range of  $0.24 \pm 0.04$ , whereas the only normal spectral emissivity calculated by use of the solidus plateau (sample #2) is with 0.28 by about 20% higher than the rest. The reason for performing the calibration on the solidus plateau was the highly noisy liquidus plateau, which could not be evaluated. In Figure 4.3 exemplary liquidus and solidus plateaus are plotted. At Figure 4.3a the plateau shows a positive slope. The end point of the plateau, where

## 4.1 Experimental

the slope shows a discontinuity, is used for calibration. In contrary, the solidification plateau is mostly not very pronounced, so mainly emerging on small time scales. In Figure 4.3b only a small undercooling is evident, but after the solidus plateau another phase changing plateau at a temperature of about 1600 K is visible.  $W_{360}$  might undergo a phase transition between two allotropic forms in the solid state, similar to pure iron.



(a) Liquidus plateau of sample #5



(b) Solidus plateau of sample #2 and additional phase changing plateau at  $\sim 1600$  K

Figure 4.3: Liquidus and solidus plateaus of  $W_{360}$ .

## 4.2 Density

Density measurements have been performed in a temperature range of about 200 K starting in the slight undercooled area. The results of the temperature dependent density measurements are plotted in Figure 4.4 according to the sample ID from Table 4.3. Raw data including uncertainties can be found in Table 7.1, where the density uncertainty has been calculated according to the estimation of *Schmon* [22], who assumes a 2% uncertainty using a coverage factor of  $k = 2$ . With a fraction of 91%, iron is the main component of *W360*, hence the pure iron density function<sup>3</sup> is also plotted in Figure 4.4 for comparison reasons.

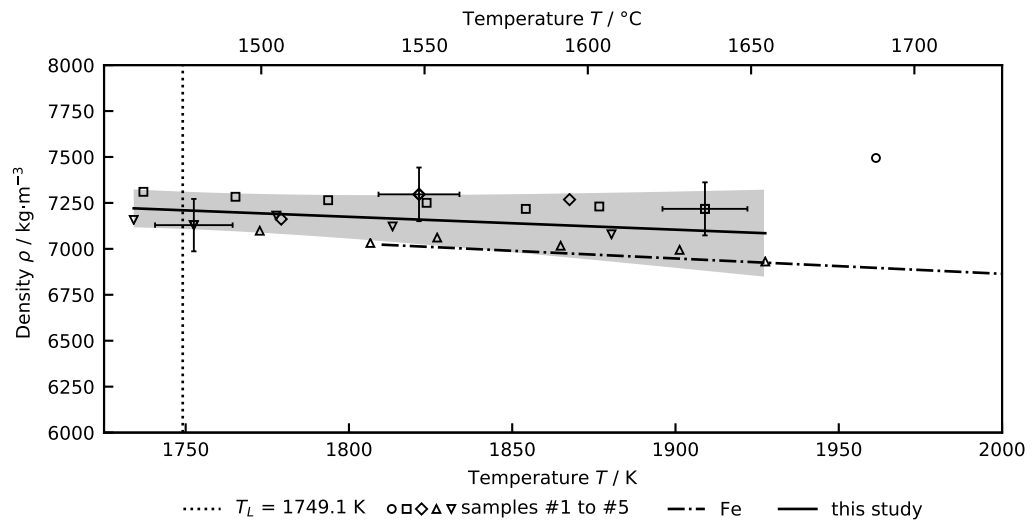


Figure 4.4: Results of temperature dependent density measurements of *W360* (Source: Table 7.1) in comparison to pure iron (Fe, mean of [38–41]). The fit has been applied over all samples, excluding #1. The corresponding fit parameter are stated in Table 4.4.

<sup>3</sup>fit parameter obtained by *Leitner et al.* [5] by building the mean of the single  $\rho_L$  and  $\frac{\partial \rho}{\partial T}$  results from [38–41]

## 4.2 Density

A linear fit has been performed over all measurement data excluding the sample #1 due to a tremendous oxide contamination. The corresponding uncertainties of the fitting parameters and the fit itself have been calculated according to *GUM* [42], also using a coverage factor of  $k = 2$ . The density results of *W360* are slightly higher compared to those of pure iron. All fit parameter are summarised in Table 4.4, whereas exemplary fit data points can be found in Table 7.3.

Table 4.4: Density fit parameters are provided according to model:  $\rho(T) = \rho_L + \frac{\partial\rho}{\partial T}(T - T_L)$

$\rho_L$	...	density at liquidus temperature / $\text{kg} \cdot \text{m}^{-3}$			
$\frac{\partial\rho}{\partial T}$	...	change of density with temperature / $\text{kg} \cdot \text{m}^{-3} \cdot \text{K}^{-1}$			
$T_L$	...	liquidus temperature / K			
T	...	temperature / K			
<b>Material</b>	$\rho_L$	$\frac{\partial\rho}{\partial T}$	$T_L$	<b>Ref</b>	
<i>W360</i>	$7210 \pm 50$	$-0.7 \pm 0.6$	1749.1	this study	
Fe	7022	-0.835	1811 [43]	[5]	

The sets of data points resulting from single measurements appear to be inherent in much lower variances than data points from all experiments. This effect might have occurred from inconsistencies in performing reference measurements, where conversion factors of pixels in mm are gained.

### 4.3 Surface Tension

Surface tension measurements have been performed over a temperature range of about 200 K, starting slightly beneath the liquidus temperature. Translational frequencies in x- and y-direction are both in the range of  $(3.8 \pm 0.5)$  Hz. The one in z-direction has been determined as explained in Section 3.2.5 in the range of  $(11 \pm 1)$  Hz, so it might not have been obtained by the theoretical formula, Equation 2.14, for coils with a linear magnetic field in z-direction as there would be a mean deviation of 3.4 Hz. Oscillation frequencies in the fundamental order  $l = 2$  range from (52 to 67) Hz.

The raw data from Table 7.2 are plotted in Figure 4.5 according to the sample ID from Table 4.3. Uncertainties of data points and their corresponding fit parameters are calculated according to *GUM* [42] using a coverage factor of  $k = 2$ . An exemplary *GUM* uncertainty budget is given in Section 6.3. Again, for comparison reasons the main component of *W360*, iron, is plotted in Figure 4.5. The iron fit data are taken from *Leitner et al.* [5].

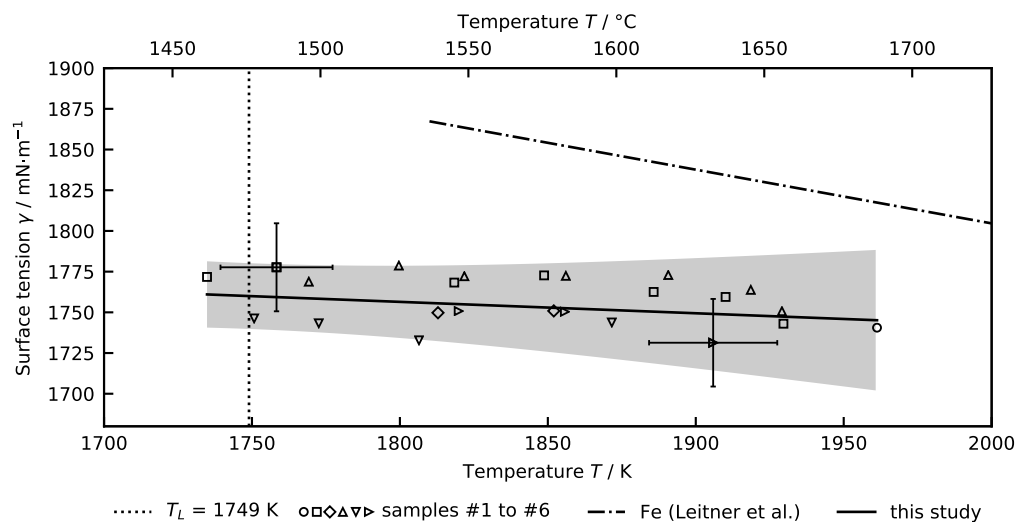


Figure 4.5: Results of temperature dependent surface tension measurements of *W360* (Source: Table 7.2) in comparison to iron (Fe, *Leitner et al.* [5]). Sample IDs according to Table 4.3. The corresponding fit parameter are stated in Table 4.5.

### 4.3 Surface Tension

The surface tension data obtained for  $W_{360}$  are compared to iron lower in both, the slope  $\frac{\partial\gamma}{\partial T}$  and the liquidus temperature intersection  $\gamma_L$ . The linear fit parameters are denoted in Table 4.5, whereas exemplary fit data points can be found in Table 7.3.

Table 4.5: Surface tension fit parameters are provided according to model:

$$\gamma(T) = \gamma_L + \frac{\partial\gamma}{\partial T}(T - T_L)$$

$\gamma_L$  ... surface tension at liquidus temperature /  $\text{mN} \cdot \text{m}^{-1}$

$\frac{\partial\gamma}{\partial T}$  ... change of surface tension with temperature /  $\text{mN} \cdot \text{m}^{-1} \cdot \text{K}^{-1}$

$T_L$  ... liquidus temperature / K

$T$  ... temperature / K

<b>Material</b>	$\gamma_L$	$\frac{\partial\gamma}{\partial T}$	$T_L$	<b>Ref</b>
$W_{360}$	$1760 \pm 10$	$-0.07 \pm 0.09$	1749.1	this study
Fe	1867	-0.33	1811 [43]	[5]



# 5 Nickel

## 5.1 Literature research

In advance of re-measuring the surface tension of liquid nickel at *Graz University of Technology*, a literature study has been done including 17 publications starting in the 1950ies. In these publications the experimental methods *Sessile Drop (SD)*, *Maximum Bubble Pressure (MBP)*, *Dynamic Drop Weight (DDW)*, *Electromagnetic Levitation (EML)* and *Electrostatic Levitation (ESL)* have been used. In this literature research the primary focus lies on analysing or benchmarking the validity of the evaluation formulas used from today's point of view. The investigation could have also been performed regarding other aspects like sample purity, or especially oxygen content of the sample or levitation atmosphere. Particularly for EML setups details about surface deformation amplitude, determination of translational frequency in vertical direction (z-direction), quality of the electromagnetic field produced by the coil system would help benchmarking the quality of the results. But most of the time crucial information about measurement and evaluation parameters is not stated in the publications. For the re-measurement of nickel in this thesis, all those possible influences are treated in Chapter 6, where a detailed uncertainty analysis is performed.

In Figure 5.1, all surface tension results of the investigated literature are depicted. The corresponding information regarding year and first author of the publication, the experimental method used (for EML and ESL even the OD evaluation formula) and finally the linear fit parameters for the temperature dependent surface tension are stated in Table 5.2. In Table 5.1 OD evaluation formulas used in the studies are given. Therein, OD formulas will be named after the ID given in this table, to avoid confusion occurring from the various equation numerations. The ID is principally assembled by the

author, equation number in the original publication and assignment mode of the formula. As described in Section 2.3, evaluation formulas derived by *Cummings and Blackburn* can be either used in the *assigned* (A) or in the *unassigned* (UA) mode, which refers to either performed or not performed identification of the five oscillation frequencies in the fundamental mode  $l = 2$ .

Table 5.1: Overview of *Oscillating Drop* (OD) evaluation formulas used in literature. The ID always contains the author initials, in some cases the original equation tags and the assignment mode of the oscillation frequencies in the  $l = 2$  mode (A: peaks assigned, UA: peaks unassigned).

ID	Author	Ref	Year	Equation	Used in
$R$	Lord Rayleigh	[17]	1879	2.5	[44-47]
$FB$	Feng & Beard	[19]	1990	2.15	[48]
$CB$ (6.3)	Cummings & Blackburn	[3]	1991	2.13	[49]
$CB$ (6.1)	Cummings & Blackburn	[3]	1991	2.8 with 2.12, 2.10	[50]
$CB$ (5.20)UA	Cummings & Blackburn	[3]	1991	2.8 with 2.11, 2.10	[4, 51-53]
$CB$ (5.20)A	Cummings & Blackburn	[3]	1991	2.8 with 2.11, 2.9	[21]

## 5.1 Literature research

Table 5.2: Literature study of the surface tension of liquid nickel. The column *Year* refers to the year of publication, *Author* to the lead author of the publication and *Ref* to the citation reference. The column *Method* gives the experimental method (SD, MBP, DDW, EML, ESL), or in case of EML<sup>†</sup> and ESL<sup>‡</sup>, OD evaluation method according to Table 5.1. Surface tension fit parameters are provided according to model:  $\gamma(T) = \gamma_M + \frac{\partial\gamma}{\partial T}(T - T_M)$

$\gamma_M$  ... surface tension at melting temperature /  $\text{mN} \cdot \text{m}^{-1}$   
 $\frac{\partial\gamma}{\partial T}$  ... change of surface tension with temperature /  $\text{mN} \cdot \text{m}^{-1} \cdot \text{K}^{-1}$   
 $T_M$  ... melting temperature / K  
 $T$  ... temperature / K

Year	Author	Method	$\gamma_M$	$\frac{\partial\gamma}{\partial T}$	$T_M$	Ref
1953	Kingery	SD	1735	-	-	[54]
1961	Fesenko	MBP	1777*	-0.38	-	[55]
1963	Allen	DDW	1780	-0.98	-	[56]
1969	Ayushina	SD	1770*	-0.22	-	[57]
1985	Keene	R <sup>†</sup>	$1854 \pm 2 \%$	-0.36	-	[44]
1986	Schade	R <sup>†</sup>	1846	-0.25	1725	[46]
1986	Nogi	SD	1782	-0.34	-	[45]
1986	Nogi	R <sup>†</sup>	1845	-0.43	-	[45]
1991	Eckler	CB(6.3) <sup>†</sup>	1924	-0.1	1728	[49]
1992	Sauerland	CB(6.1)UA <sup>†</sup>	1868	-0.22	1728	[50]
1993	Brooks	CB(5.20)UA <sup>†</sup>	1797	-0.15	1728	[52]
2004	Ishikawa	FB <sup>‡</sup>	1739	-0.22	1728	[48]
2005	Brillo	CB(5.20)UA <sup>†</sup>	1770	-0.33	1727	[51]
2005	Xiao	SD	1823	-0.46	1728	[58]
2014	Ozawa	CB(5.20)UA <sup>†</sup>	1829	-0.4014	1728	[53]
2015	Aziz	CB(5.20)UA <sup>†</sup>	$1864 \pm 3$	$-0.35 \pm 0.02$	1728	[4]
2016	SanSoucie	R <sup>‡</sup>	1653	-0.03558	1728	[47]

\* obtained  $\gamma_M$  from  $\gamma(T \neq T_M)$

## 5 Nickel

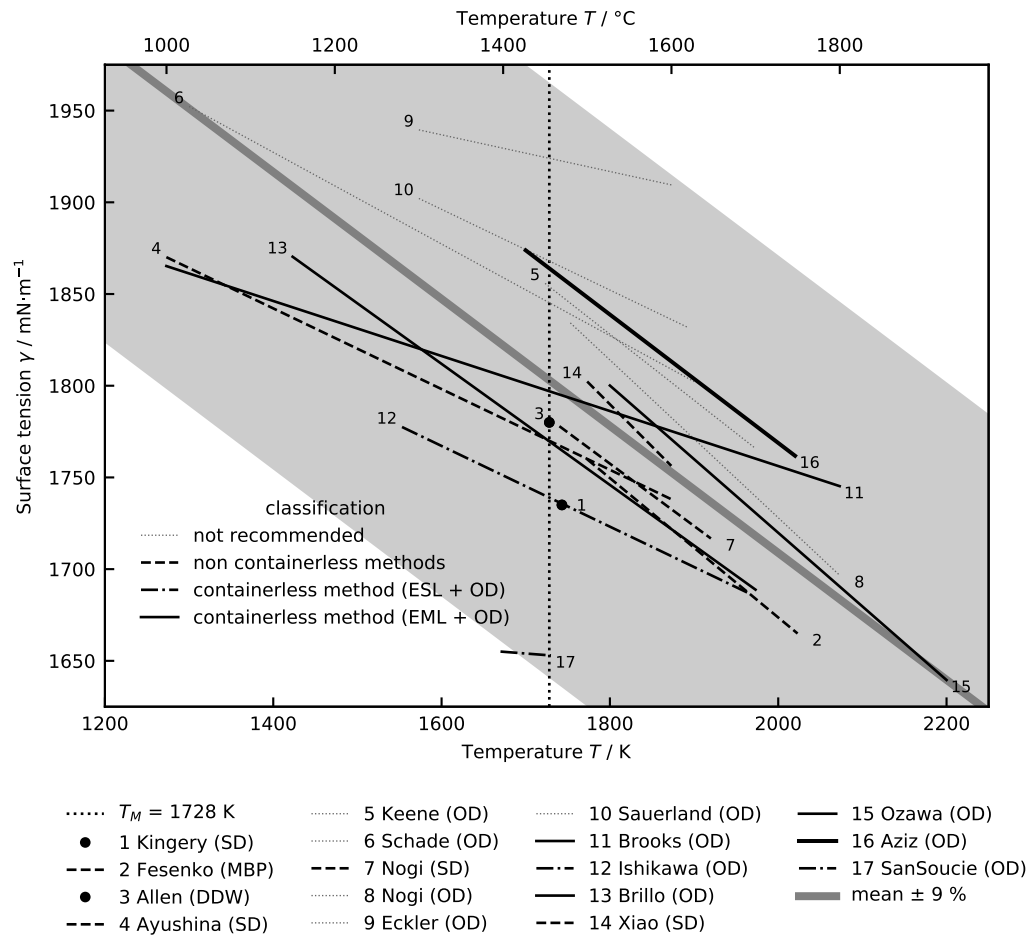


Figure 5.1: Summary of literature study for the surface tension of liquid nickel. A classification has been performed for differing experimental methods and benchmarked OD evaluation methods.

When considering all studies in Figure 5.1 and Table 5.2, surface tension at the melting point ranges from (1653 to 1924)  $\text{mN} \cdot \text{m}^{-1}$  at a mean value of  $\overline{\gamma_M} = (1800 \pm 100) \text{mN} \cdot \text{m}^{-1}$ . The corresponding slope covers the bandwidth of  $\frac{\partial \gamma}{\partial T} = (-0.3 \pm 0.2) \text{mN} \cdot \text{m}^{-1} \cdot \text{K}^{-1}$ . The investigated temperature area extends nearly symmetrically around the melting point of nickel at  $T_M = 1728$  K [31] from (1273 to 2200) K.

At the beginning of the introduction in Chapter 2, the two general approaches for measuring surface tension, namely non-containerless and containerless methods, have been described already and can be contrasted now for the literature study. Results of non-containerless methods appear in a range of  $\bar{\gamma}_M = (1780 \pm 60) \text{ mN} \cdot \text{m}^{-1}$ . The half bandwidth of  $60 \text{ mN} \cdot \text{m}^{-1}$  corresponds to 3 % of  $\bar{\gamma}_M$ . In comparison to this, the surface tension at the melting point with  $\bar{\gamma}_M = (1820 \pm 150) \text{ mN} \cdot \text{m}^{-1}$  is situated by 2 % higher. In addition, also the half bandwidth is with 8 % more than two times higher. This seems to be plausible, as samples investigated by non-containerless methods typically are lowered in surface tension due to suffering from contamination with crucibles.

The widely spreading results obtained by containerless methods (EML and ESL) using the OD technique for evaluation is striking. In order to ascertain more precisely the reason for this broad range, the OD formulas used for evaluation have been investigated. All formulas, as stated in Table 5.1, were in use except the state-of-the-art formula *CB(5.20)A* for the EML setup. Before the publication of *Cummings and Blackburn* in 1991, terrestrial conditions have not been considered by evaluation under the *Rayleigh* equation (*R*). Thus EML studies of *Keene* [44], *Schade* [46] and *Nogi* [45] are classified as "not recommended". Furthermore, the OD formulas for EML setups *CB(6.3)* and *CB(6.1)* are also outdated on the basis of assuming a constant magnetic field in the vertical direction between the levitation coils instead of a linear changing one as discussed in Section 2.3. Hence the results of *Eckler* [49] and *Sauerland* [50] are classified as "not recommended" as well. As a consequence the mean surface tension at the melting point is lowered by 1.5 % and yields  $\bar{\gamma}_M = (1780 \pm 110) \text{ mN} \cdot \text{m}^{-1}$ . The overall mean value equals now the unchanged one of non-containerless methods.

The remaining EML results have been evaluated by *CB(5.20)UA*, which principally gives an upper limit of the surface tension. If sample mass and rotation is low *CB(5.20)UA* may deviate only insignificantly from the best approximating formula *CB(5.20)A*.

The most accurate OD evaluation formula for terrestrial ESL is the one derived by *Feng and Beard* (*FB*), which has been used at the publication of *Ishikawa* [48]. In contrast, the recently published surface tension results from

*SanSoucie* [47], that have been obtained by means of terrestrial ESL at the *NASA Marshall Space Flight Center* in Huntsville, have been gained under usage of the *Rayleigh* equation ( $R$ ). The authors legitimated the usage for their specific ESL setup as deviations to  $FB$  were estimated to be insignificantly small.

The two "outliers" of the remaining recommended literature are the studies from the results from *SanSoucie* [47] and *Aziz* [4]. The obtained surface tension of *SanSoucie* exhibits the major deviation from the mean surface tension at the melting temperature of  $-7\%$ . The results from *Ishikawa* [48], also gained by means of ESL, are only  $2\%$  lower than the mean. The study performed by *Aziz* [4] at the *Thermophysics and Metalphysics Group* at *Graz University of Technology* is the upper outlier with a deviation of  $5\%$  from the mean. The evaluation was performed with  $CB(5.20)UA$ , although technical possibilities for the usage of  $CB(5.20)A$  had been available. Later in 2016, *Aziz* stated in his doctoral thesis [21] that results lower by  $1.3\%$  when using  $CB(5.20)A$ , contrary to the expectations. This correction has not been included to Figure 5.1 as no exact fit equation is given in the doctoral thesis. In the further course of the investigations, the original raw measurement data of *Aziz* have been re-evaluated after the attempt of reproducing the evaluation results of *Aziz*. This is described in Section 5.3.

Table 5.3: Purities stated in publications. Purities are exclusively given on metals basis (m.b.) and not as total purities.

Purity / %	studies
99.999	<i>Brooks, Ozawa</i>
99.995	<i>Aziz, SanSoucie</i>
> 99.99	<i>Nogi (SD)</i>
99.9	<i>Allen, Ishikawa</i>
not stated	<i>Kingery, Fesenko, Ayushina, Brillo,</i>

Table 5.3 gives the stated purities in metals basis for the recommended studies. This includes no information regarding impurification by surfactants

like oxygen or sulphur. Here, no definite correlation between purity on metals basis and surface tension can be confirmed.

A comparison of the recommended EML studies according to the levitation atmospheres results that all experiments have been carried out under reducing atmosphere of 4 % volume fraction  $H_2$  at minimum (*Aziz*). The maximal  $H_2$  volume fraction of 8 % was used by *Brillo*. *Brooks* and *Ozawa* operated at a 5 % volume fraction admixture of  $H_2$ . In contrast, ESL measurements are not mentioned here as levitation is performed under much lower pressures.

## 5.2 Re-measurement

### 5.2.1 Material, experimental and evaluation details

In this work, nickel samples provided by the three suppliers *Alfa Aesar*, *Goodfellow* and *Sigma-Aldrich* have been investigated. In Table 5.4 information of the investigated nickel samples, such as supplier, different purities, article numbers and LOT numbers, is stated.

Table 5.4: Information about nickel samples measured. The purities have been stated by the supplier - the corresponding certificates of analysis are attached in the appendix.

Supplier	Art#	LOT#	Purity m.b.	Purity tot
<i>Alfa Aesar</i>	42331	L29X008	99.995 %	n/a
<i>Goodfellow</i>	267074-14G	28	99.99+ %	99.996 %
<i>Sigma-Aldrich</i>	NI007950	MKCD1178	99.99+ %	n/a

## 5 Nickel

As the nickel samples have been delivered in rod and slug geometry, only minor shaping alterations had to be made. No polishing had to be performed as oxidation was not problematic. The different preparation and experimentation stages of the samples are depicted in Figure 5.2.

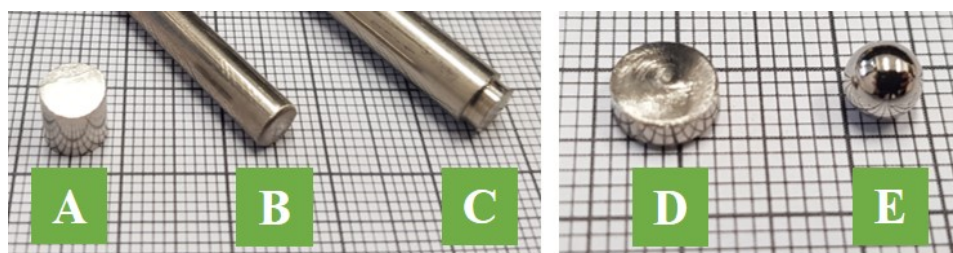


Figure 5.2: Nickel samples in different stages of preparation and experimentation. The picture on the left side shows the shapes as delivered from the suppliers *Alfa Aesar* (A, slug), *Goodfellow* (B, rod) and *Sigma-Aldrich* (C, rod trimmed on one side from fabrication), whereas on the right side a pre-levitation-sample (D), that had been already machined to a cylindrical disk shape ready to be inserted into the levitation chamber, and a post-levitation-sample (E) is depicted. In order to estimate size, samples were placed on millimetre paper.

In Table 5.5 information regarding the single experiments like sample masses with their mass losses, pyrometer readings at the melting plateau and normal spectral emissivities calculated from pyrometer readings at the melting plateaus are summarised. The ID consists of the supplier initials (AA for *Alfa Aesar*, GF for *Goodfellow* and SA for *Sigma-Aldrich*) and a running number. The samples masses investigated were in a range of  $475 \text{ mg} \pm 30\%$ . The mass loss during levitation was no major problem as it occurred in the small bandwidth of (0.0 to 1.4) mg, which corresponds to 0.1 % in average. When starting experimentation, the levitation chamber was evacuated to the  $10^{-6}$  mbar level. Consecutively, the chamber was flooded with high purity argon<sup>1</sup> up to around 750 mbar and with a custom gas mixture<sup>2</sup>, composed of helium with a slight admixture of hydrogen, for further  $\sim 40$  mbar to flood the gas pipes with cooling gas for avoiding sudden temperature changes. Regarding levitation, the frequency generator operated at 350 kHz until 03.05.2019 and later at 290 kHz.

<sup>1</sup>*Alphagaz*<sup>TM</sup>1 Ar [27] from AIR LIQUIDE: Ar  $\geq 99.999$  mol%

<sup>2</sup>*custom gas mixture* from AIR LIQUIDE: He + 3.83 vol% H<sub>2</sub>

## 5.2 Re-measurement

Table 5.5: Information according to specimen mass and experimental parameter

$m_{\text{start}}$	...	mass before levitation / mg
$m_{\text{end}}$	...	mass after levitation / mg
$\Delta m$	...	relative mass loss through levitation / %
$T_{\text{pyro,M}}$	...	pyrometer reading for further calibration at melting plateau / °C
$\epsilon$	...	calculated normal spectral emissivity at the melting plateau
$N_{\text{D}}$	...	number of density measurements
$N_{\text{S}}$	...	number of surface tension measurements

ID	date	$m_{\text{start}}$	$m_{\text{end}}$	$\Delta m$	$T_{\text{pyro,M}}$	$\epsilon$	$N_{\text{D}}$	$N_{\text{S}}$
AA#1	10.04.2019	517.3	516.8	0.10	1049	0.208	1	6
AA#2	10.04.2019	398.7	398.1	0.15	1048	0.206	0	8
AA#3	12.04.2019	463.8	463.3	0.11	1050	0.208	4	6
AA#4	12.04.2019	394.6	393.2	0.35	1048	0.206	0	3
AA#5	12.04.2019	727.0	726.8	0.03	1052	0.210	1	2
AA#6	12.04.2019	516.8	516.8	0.00	1049	0.207	0	7
AA#7	16.04.2019	509.1	508.9	0.04	1050	0.209	0	14
AA#8	16.04.2019	511.2	510.9	0.06	1047	0.205	0	12
AA#9	16.04.2019	361.1	360.9	0.06	1051	0.210	0	8
AA#10	17.04.2019	393.4	393.2	0.05	1047	0.205	15	0
SA#1	17.04.2019	443.5	443.0	0.11	1048	0.206	0	15
GF#1	18.04.2019	522.7	522.2	0.10	1049	0.207	0	14
SA#2	18.04.2019	460.7	460.4	0.07	1048	0.206	1	11
SA#3	18.04.2019	438.9	438.6	0.07	1046	0.204	1	6
AA#11	25.04.2019	393.2	393.0	0.05	1040	0.198	5	1
AA#12	25.04.2019	463.4	463.2	0.04	1040	0.198	9	6
GF#2	30.04.2019	463.2	463.0	0.04	1047	0.205	1	12
GF#3	30.04.2019	516.3	516.0	0.06	1047	0.205	1	15
SA#4	30.04.2019	382.1	381.7	0.10	1045	0.203	1	11
SA#5	30.04.2019	451.0	450.5	0.11	1045	0.203	1	13
GF#4	02.05.2019	533.8	533.4	0.07	1049	0.207	1	11
GF#5	02.05.2019	485.5	485.0	0.10	1046	0.204	2	13
SA#6	03.05.2019	498.1	497.4	0.14	1045	0.195	10	0
AA#13	12.06.2019	463.2	462.5	0.15	1037	0.203	0	11
SA#7	12.06.2019	497.4	497.1	0.06	1044	0.202	1	13

## 5 Nickel

Exemplary temperature profiles including the pyrometer readings of the 1- and 2-colour-pyrometers and the calibrated temperature, as well as the corresponding melting and solidification plateaus, are depicted in Figure 3.4 in Section 3.2.3. Here, in Figure 5.3, a temperature course is plotted, where also the performed measurements are marked. The greenly shadowed areas indicate the time range used for evaluation and the grey areas denote the residual measurement time. For the investigation of nickel the temperature has been determined directly from the pyrometer data, so a mean temperature including statistical uncertainty could be calculated for the evaluated section.

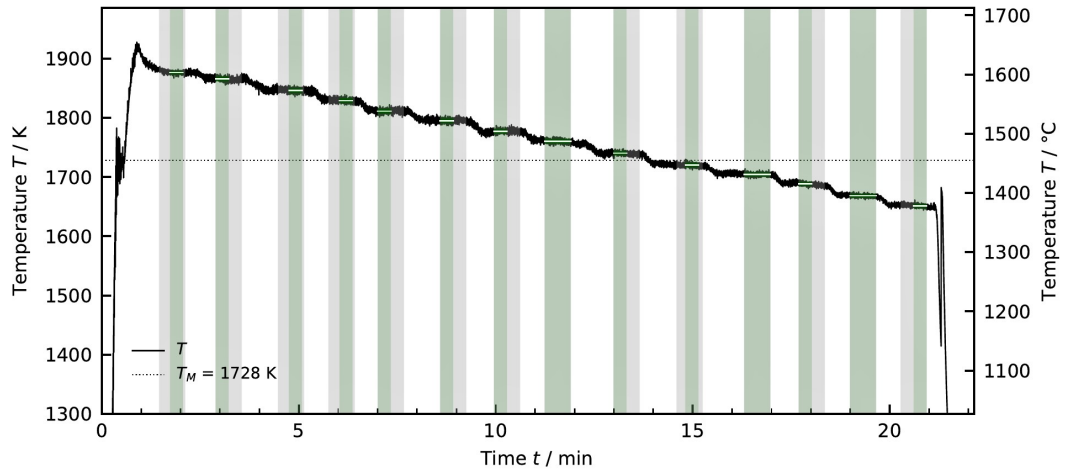


Figure 5.3: Profile of the calibrated temperature of an experiment for investigating nickel. The green areas mark the measurement time used for evaluation, whereas the grey areas denote the residual measurement time.

The pyrometer readings of the melting plateaus appeared in the bandwidth of  $(1046 \pm 9) ^\circ\text{C}$ , which corresponds to  $(1319 \pm 9) \text{ K}$ . This is much smaller than the one of the evaluated solidification plateaus of  $(1030 \pm 20) ^\circ\text{C}$  or  $(1300 \pm 20) \text{ K}$ . Theoretically, those plateaus should appear at the same pyrometer reading for similar measurement conditions. For temperature calibration, the melting plateau has been used due to the elevated reproducibility. This topic is discussed in more detail in Section 6.1.1.

## 5.2 Re-measurement

Regarding the evaluation of surface tension according to Equation 3.3, exemplary spectra of nickel for determining translational frequencies in the horizontal plane in x- and y-direction, translational frequencies in z-direction (vertical axis) and fundamental frequencies have been already plotted in Figures 3.9, 3.10 and 3.12 respectively (Section 3.2.5).

The following mean values of translational frequencies emerged at experimentation:

$$\begin{aligned}\bar{\nu}_{\tau,x} &= (5.1 \pm 0.5) \text{ Hz} \\ \bar{\nu}_{\tau,y} &= (5.2 \pm 0.4) \text{ Hz} \\ \bar{\nu}_{\tau,z} &= (12.1 \pm 0.6) \text{ Hz}\end{aligned}$$

Furthermore, oscillation frequencies of fundamental order  $l = 2$  ( $\nu_{2,m}$ ) with  $m$  from -2 to +2 have been obtained in the broad range of (35 to 70) Hz. The mean fundamental frequency, which corresponds to the root mean square of all five  $\nu_{2,m}$ , is about 58 Hz.

### 5.2.2 Density

Due to the implicit requirement of density for the surface tension determination according to Equation 3.3, density has been also measured and compared to literature. The results are presented in Figure 5.4 and Table 5.6. Uncertainties have been calculated in conformity with GUM [42], using a coverage factor of  $k = 2$ .

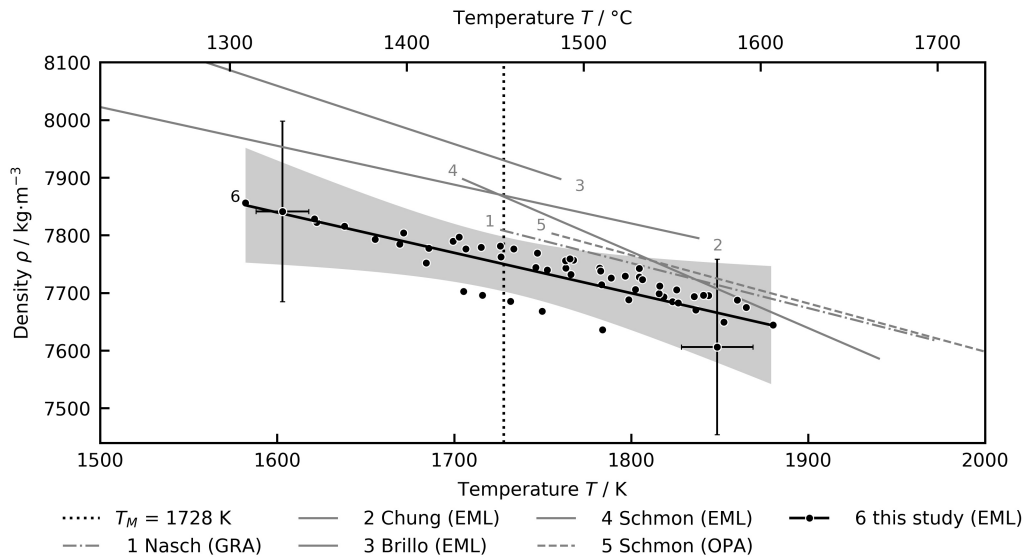


Figure 5.4: Results of density measurements of nickel including literature obtained by different methods. Results from literature were not only gained by the same method of EML, but also by *Gamma Ray Attenuation* (GRA) and *Ohmic Pulse-Heating* (OPA).

The selected results from literature were not only obtained by the method of EML, but also by *Gamma Ray Attenuation* (GRA) and *Ohmic Pulse-Heating* (OPA). Data from *Schmon et al.* [59] were also gained at the *Thermophysics and Metalphysics Group* at *Graz University of Technology*, the results obtained by EML even at the same apparatus by investigation of nickel delivered from *Alfa Aesar* exhibiting the same LOT number. Regardless results are lowered by  $117 \text{ kg} \cdot \text{m}^{-3}$ , which corresponds to  $-1.5\%$ . In general, the density of this work is lower than in the literature listed. In Figure 5.4, it is striking

## 5.2 Re-measurement

that five measurement points, which are all from AA#11 (according to Table 5.5), lie beneath the lower edge of the grey shaded uncertainty area. Considered individually, these series of points seems to be shifted down due to a systematic measurement error, possibly occurring from an inconsistency of the pixel-millimeter-conversion obtained by the corresponding reference measurement.

Table 5.6: Result of the density determination of liquid nickel and corresponding literature. The mean of all listed studies has been used for the surface tension evaluation. Density fit parameters are provided according to model:  $\rho(T) = \rho_M + \frac{\partial\rho}{\partial T}(T - T_M)$

$\rho_M$	...	density at melting temperature / $\text{kg} \cdot \text{m}^{-3}$		
$\frac{\partial\rho}{\partial T}$	...	change of density with temperature / $\text{kg} \cdot \text{m}^{-3} \cdot \text{K}^{-1}$		
$T_M$	...	melting temperature (Nickel: 1728 K [31])		
$T$	...	temperature / K		
Description	Method	$\rho_M$	$\frac{\partial\rho}{\partial T}$	Ref
Nasch*	GRA	7808	-0.781	[60]
Chung*	EML	$7869 \pm 0.8 \%$	-0.673	[61]
Brillo*	EML	$7929 \pm 1 \%$	-1.01	[38]
Schmon	EML	$7867 \pm 1.6 \%$	-1.325	[59]
Schmon	OPA	$7826 \pm 3.5 \%$	-0.838	[59]
this study	EML	$7750 \pm 20$	$-0.7 \pm 0.3$	-
mean	various	$7800 \pm 100$	$-0.9 \pm 0.5$	-

\* obtained  $\rho_M$  from  $\rho(T \neq T_M)$

For the evaluation of surface tension the mean value of the literature and the result of this study, as presented in Table 5.6, has been used.

### 5.2.3 Surface tension

The obtained surface tension data are presented in Figure 5.5, as well as the surface tension fit parameters in Table 5.2. A temperature range of (1600 to 1870) K was investigated, which covers a part of about 130 K in the undercooled range and of about 140 K in the liquid phase. A classification

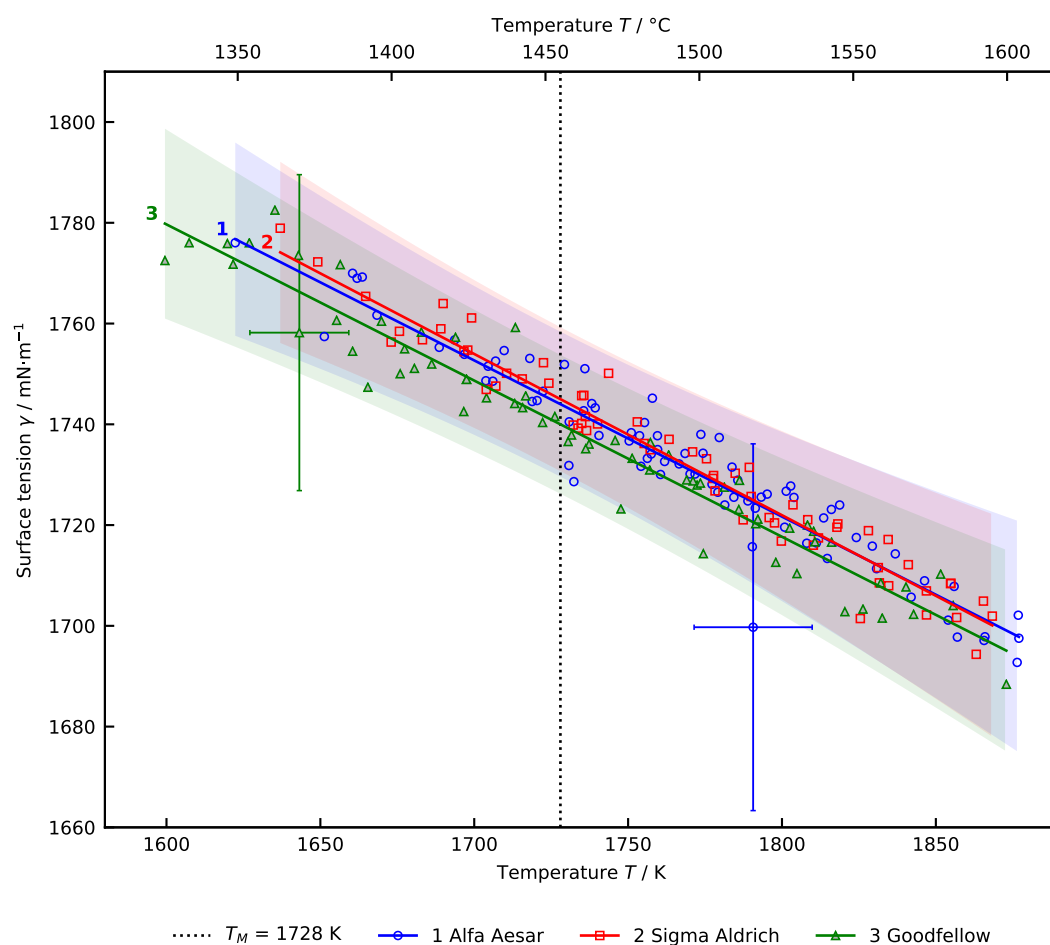


Figure 5.5: Result of the surface tension measurements of high purity liquid nickel provided by the suppliers *Alfa Aesar*, *Goodfellow* and *Sigma-Aldrich* performed at *Graz University of Technology*. Uncertainties of single data points as well as the uncertainty of the fit equation has been determined by means of GUM [42].

## 5.2 Re-measurement

regarding the three supplier *Alfa Aesar*, *Goodfello* and *Sigma-Aldrich* has been made. All uncertainties have been critically assessed by means of GUM (*Guide to the expression of uncertainty in measurement*) [42] with a coverage factor of  $k = 2$ . Potential sources of error are discussed and quantified in Chapter 6. It is evident that surface tension is not significantly deviating for the three supplier since the maximal difference occurring between *Goodfellow* and *Sigma-Aldrich* corresponds only to 0.3 %. In addition, this deviation lies far within the limits of uncertainties. As already discussed in Section 2.3, the most accurate equation for surface tension determination is  $CB(5.20)A$  according to Table 5.1. In earlier times,  $CB(5.20)UA$ , which only provides an upper limit of surface tension, mostly was in use since assigning oscillation frequencies in the fundamental order was technically not feasible or too time-consuming. Nowadays,  $CB(5.20)UA$  is used if a distinct assignment is not possible. Here, the mean values of the surface tension at the melting point  $\bar{\gamma}_M$  is only increased by 0.2 % when using  $CB(5.20)UA$ . This is not much in comparison to the total uncertainty of the fit equation, including the corresponding parameter as well as the temperature uncertainty, at the melting point of  $\pm 12 \text{ mN} \cdot \text{m}^{-1}$  or  $\pm 0.7 \%$ .

Table 5.7: Results of the re-measurement of the surface tension of liquid nickel with samples from different supplier. Methods denote the OD evaluation method used summarised in Table 5.1. Surface tension fit parameters are provided according to model:  $\gamma(T) = \gamma_M + \frac{\partial\gamma}{\partial T}(T - T_M)$

$\gamma_M$	...	surface tension at melting temperature / $\text{mN} \cdot \text{m}^{-1}$
$\frac{\partial\gamma}{\partial T}$	...	change of surface tension with temperature / $\text{mN} \cdot \text{m}^{-1} \cdot \text{K}^{-1}$
$T_M$	...	melting temperature (Nickel: 1728 K [31])
$T$	...	temperature / K

Supplier	Method	$\gamma_M$	$\frac{\partial\gamma}{\partial T}$
<i>Alfa Aesar</i>	$CB(5.20)A$	$1744 \pm 4$	$-0.31 \pm 0.06$
<i>Goodfellow</i>	$CB(5.20)A$	$1740 \pm 4$	$-0.31 \pm 0.05$
<i>Sigma-Aldrich</i>	$CB(5.20)A$	$1745 \pm 4$	$-0.32 \pm 0.06$
all	$CB(5.20)A$	$1743 \pm 2$	$-0.31 \pm 0.03$
all	$CB(5.20)UA$	$1746 \pm 2$	$-0.30 \pm 0.03$

### 5.3 Re-evaluation of Aziz study

Now a direct comparison of the results from both studies operated at the EML apparatus of the *Thermophysics and Metalphysics Group at Graz University of Technology*, namely the study from Aziz, Schmon and Pottlacher [4] in 2015 and this work in 2019, can be facilitated. The EML apparatus has been

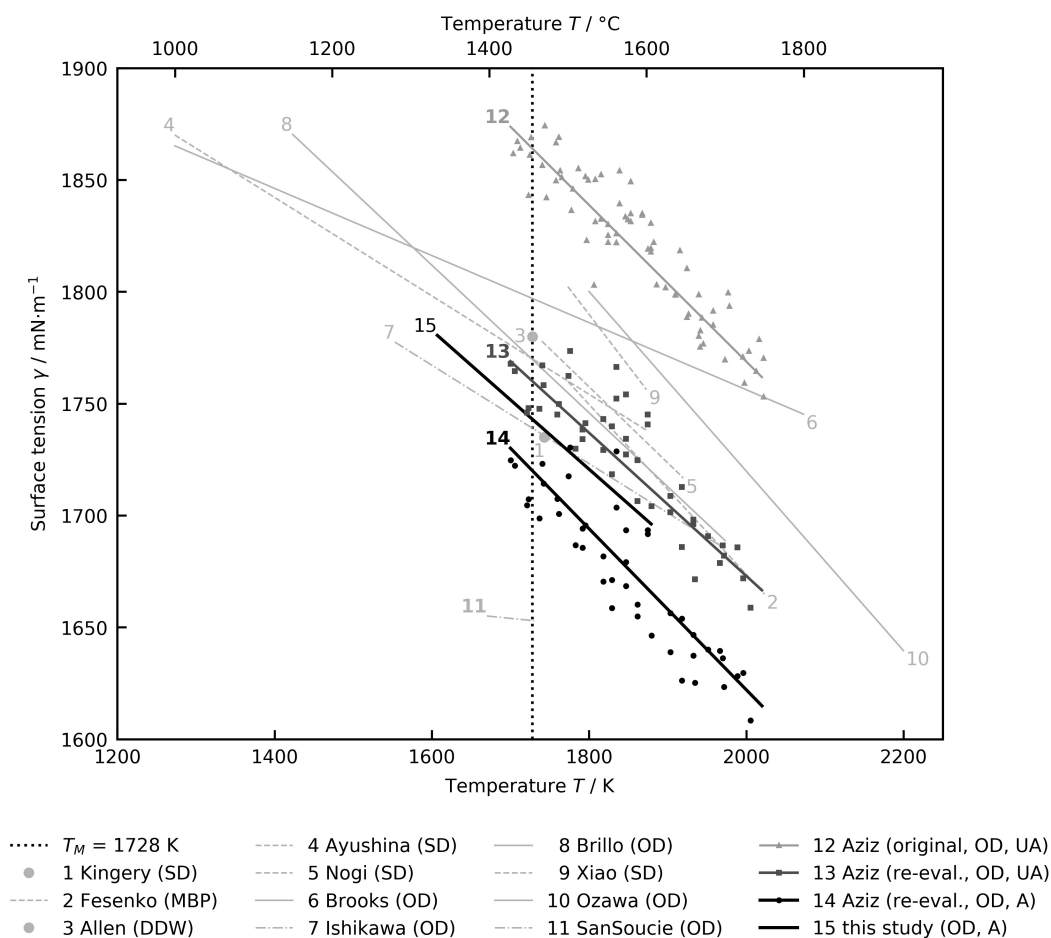


Figure 5.6: Conclusion of the re-evaluation of the experimental data obtained by Aziz [4] in 2015. The abbreviations UA and A in the legend correspond to evaluation formulas  $CB(5.20)UA$  and  $CB(5.20)A$ , respectively. A comparison is also carried out with the results of this work and previous literature.

### 5.3 Re-evaluation of Aziz study

modified slightly and the group gained further knowledge in evaluation processes since the measurements of *Aziz*, but nickel samples from *Alfa Aesar* exhibiting the identical LOT number have been investigated, which is a good basis for comparison.

When presenting the data in Figure 5.6 and Table 5.8 a tremendous deviation of the results of 7% is conspicuous. To identify the root cause, the still available original data was inspected and re-evaluated in order to check if the results obtained by *Aziz* may be reproduced. In this case, further investigations may be conducted regarding the experimental setup itself. However, it appeared that the re-evaluated surface tension lowered by 5.5% by use of the same evaluation formula, namely  $CB(5.20)UA$ . *Aziz* already mentioned in his doctoral thesis [21] that results lower for 1.3% after evaluation with  $CB(5.20)A$ , but this is far lower. Accordingly, the re-evaluation of the original data has been also performed by means of  $CB(5.20)A$ , which gave a lowering of even 8% according to the original data. In the end, results of measurements obtained in course of this work are actually 1.3% higher compared to the re-evaluated data from *Aziz*.

Table 5.8: Comparison of the re-evaluation of the surface tension of liquid nickel from original measurement data from *Aziz* [4] with the original results from the study and the re-measurement of this work. Methods denote the OD evaluation method used, which are summarised in Table 5.1. Surface tension fit parameters are provided according to model:  $\gamma(T) = \gamma_M + \frac{\partial\gamma}{\partial T}(T - T_M)$

$\gamma_M$	...	surface tension at melting temperature / $\text{mN} \cdot \text{m}^{-1}$
$\frac{\partial\gamma}{\partial T}$	...	change of surface tension with temperature / $\text{mN} \cdot \text{m}^{-1} \cdot \text{K}^{-1}$
$T_M$	...	melting temperature (Nickel: 1728 K [31])
$T$	...	temperature / K

Description	Method	$\gamma_M$	$\frac{\partial\gamma}{\partial T}$
Aziz (original)	$CB(5.20)UA$	$1864 \pm 3$	$-0.35 \pm 0.02$
Aziz (re-evaluated)	$CB(5.20)UA$	$1760 \pm 10$	$-0.32 \pm 0.09$
Aziz (re-evaluated)	$CB(5.20)A$	$1720 \pm 10$	$-0.36 \pm 0.09$
this study	$CB(5.20)A$	$1743 \pm 2$	$-0.31 \pm 0.03$

After comparing the evaluated translational frequencies, the main reason for the 8% elevated original results had been identified. *Aziz* determined the translational frequencies in z-direction in a bandwidth of  $\bar{\nu}_{\tau,z} = (5.9 \pm 0.3)$  Hz, in the similar order or magnitude as the translational frequencies in x- and y-direction with  $\bar{\nu}_{\tau,x} = (5.5 \pm 0.1)$  Hz and  $\bar{\nu}_{\tau,y} = (5.7 \pm 0.1)$  Hz, although Equation 2.14 states that  $\nu_{\tau,z}$  should be the double of  $\nu_{\tau,x}$  and  $\nu_{\tau,y}$  for magnetic fields of perfect linearity in z-direction. At the re-evaluation performed in this work, translational frequencies in z-direction have been determined in the range of  $(14.6 \pm 0.3)$  Hz by the same method as described in Section 3.2.5. So FFT-spectra of nickel density measurements performed by Alexander Schmon were created, where  $\nu_{\tau,z}$  can be directly obtained, in order to get an idea of the guiding range of  $\nu_{\tau,z}$ . Accordingly, the frequencies in the centre of mass spectra of the x- and y-coordinate with high amplitudes in the vicinity of the guiding range could be matched.

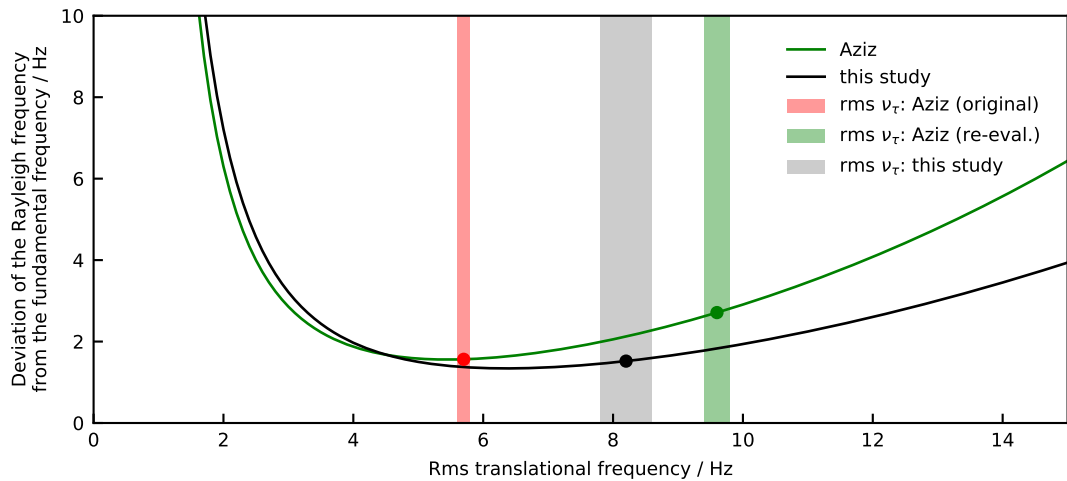


Figure 5.7: Visualisation of the change of the Rayleigh frequency after re-evaluation of the translational frequencies of data obtained by *Aziz*. In order to compare this with measurement data from this work, which exhibits fundamental frequencies in a different frequency range, the deviation of the Rayleigh frequency from the fundamental frequency is plotted on the y-axis.

The effect of the re-evaluated translational frequency in z-direction on the Rayleigh frequency is visualised in Figure 5.7. Therein, also a comparison with the measurements performed within this work is made. For this

### 5.3 Re-evaluation of Aziz study

reason the deviation of the Rayleigh frequency  $\nu_R$  from the fundamental frequency  $\nu_{2,m} = \frac{1}{5}(\nu_{2,0}^2 + 2\nu_{2,|1|}^2 + 2\nu_{2,|2|}^2)$  is plotted regarding to the varying rms translational frequency. The two curves state dependencies for typical experimental conditions<sup>3</sup>. The points/shadings on the curve mark the according mean-positions/ranges of the rms translational frequencies used for surface tension evaluation. It is evident that the deviation is further increased after re-evaluation of data obtained by *Aziz*, which led to lower surface tension values for unchanged mass.

In order to elaborate a reasonable explanation of the residual 1.3% deviation from the surface tension results of this work and the re-evaluated data originally obtained by *Aziz*, further differing parameter emerging at experimentation and evaluation have to be analysed. In contrast to this work, *Aziz* investigated samples with masses of about 1200 mg, which is more than twice as high as the mean of masses used in this work. Accordingly, the oscillation frequencies in the fundamental order of  $l = 2$  shifted towards low frequencies ranging from (20 to 50) Hz. As sample rotation is directly correlated to the splitting of corresponding  $-m$  and  $+m$  modes, Table 5.9 shows that at the measurements of *Aziz* stronger rotations occurred than at measurements of this work, which results in a higher deviation between the surface tension obtained either with *CB(5.20)UA* or *CB(5.20)A* in connection with the higher sample mass.

Table 5.9: Comparison of the  $m = \pm 1$  and  $m = \pm 2$  mode splitting of *Aziz* study and this work. In addition, also the resulting difference of the surface tension at the melting point for evaluation formulas *CB(5.20)UA* and *CB(5.20)A* are given.

$\overline{\Delta\nu_{2,|m|}}$  ... mean splitting of the  $\pm m$  mode / Hz  
 $\Delta\gamma_M$  ... deviation of the surface tension at the melting point for evaluation with either *CB(5.20)UA* or *CB(5.20)A* /  $\text{mN} \cdot \text{m}^{-1}$

Study	$\overline{\Delta\nu_{2, 1 }}$	$\overline{\Delta\nu_{2, 2 }}$	$\Delta\gamma_M$
<i>Aziz</i> [4]	9	17	52
this work	3	6	3

<sup>3</sup>*Aziz*: fundamental frequency  $\nu_{2,m} = 37$  Hz, sample radius  $a = 3.3$  mm  
 This study: fundamental frequency  $\nu_{2,m} = 58$  Hz, sample radius  $a = 2.4$  mm

## 5 Nickel

One possibility to explain the 1.3 % of deviation between the re-evaluated measurement of *Aziz* and this work is, that *Aziz's* samples with higher masses experience higher radial surface deformation amplitudes, which lead to decreased surface tension results. In Section 6.1 this effect is explained, as well as the possible correlation between lowered surface tension and increased radial surface deformation. It is shown that both selected quantifications of the surface deformation are increased for the measurements performed by *Aziz*, but the influence could not be verified. In general, it is difficult to find a representable quantification for radial surface tension deformation under terrestrial conditions, so in future, further emphasis has to be put on the investigation of this topic.

Another reason for the deviation could be the combination of a different coil setup with different sample mass ranges. So, that each coil setup has a different deviation from the theoretically demand of a perfect linearly changing magnetic induction in the vertical direction of the *Cummings and Blackburn* correction.

## 5.4 Conclusion

The result of the investigation of the surface tension of liquid nickel includes a literature benchmarking, the re-measurement at *Thermophysics and Metallurgy Group at Graz University of Technology* and re-evaluation of data obtained by Aziz in 2015. The outcome is presented in Figure 5.8, as well as in Table 5.10.

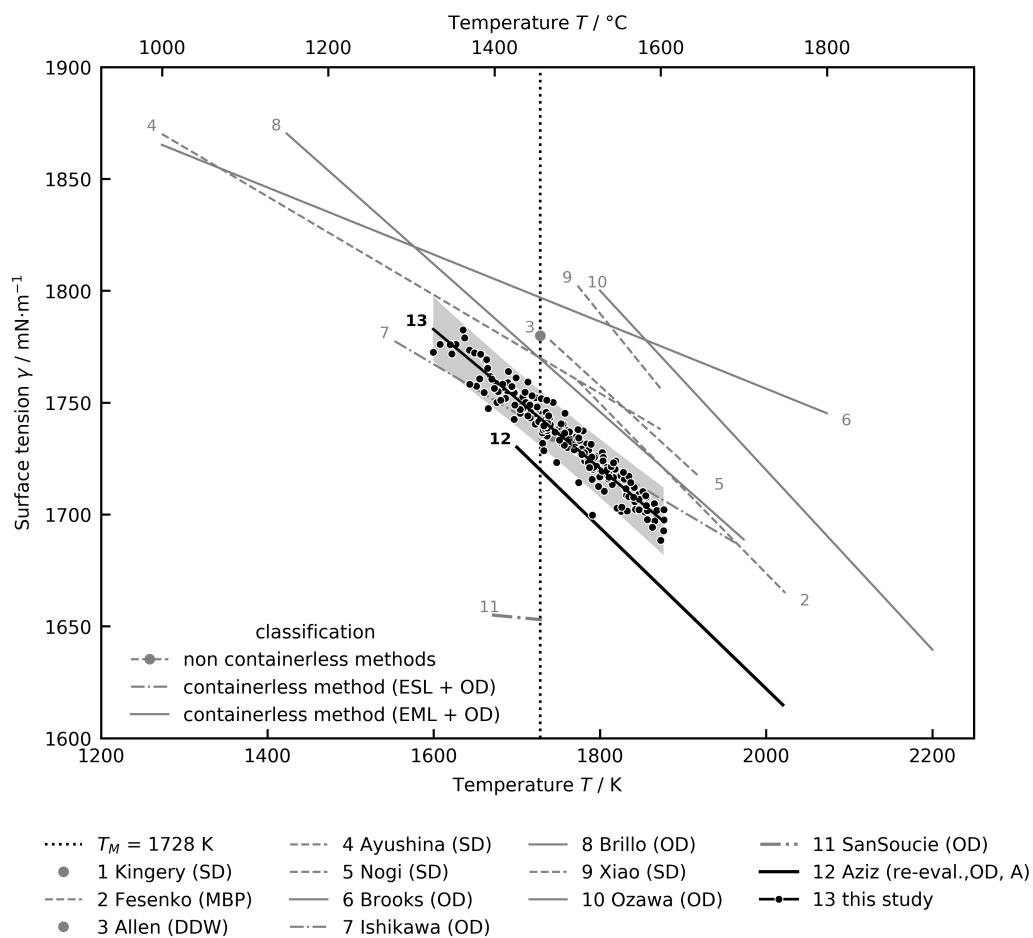


Figure 5.8: The conclusion of the investigation of the surface tension of nickel gives a résumé of literature research, re-measurement and re-evaluation of experimental data obtained by Aziz [4] in 2015.

## 5 Nickel

Table 5.10: Compendium of the investigation of the surface tension of liquid nickel within this work. Methods which denote the OD evaluation method used are summarised in Table 5.1. Surface tension fit parameters are provided according to model:  $\gamma(T) = \gamma_M + \frac{\partial\gamma}{\partial T}(T - T_M)$

$\gamma_M$	...	surface tension at melting temperature / $\text{mN} \cdot \text{m}^{-1}$
$\frac{\partial\gamma}{\partial T}$	...	change of surface tension with temperature / $\text{mN} \cdot \text{m}^{-1} \cdot \text{K}^{-1}$
$T_M$	...	melting temperature (Nickel: 1728 K [31])
$T$	...	temperature / K
$T$ range	...	temperature range of investigation

Description	Method	$\gamma_M$	$\frac{\partial\gamma}{\partial T}$	$T$ range
Aziz (re-evaluated)	CB(5.20)A	$1720 \pm 10$	$-0.36 \pm 0.09$	(1700 to 2020) K
this study	CB(5.20)A	$1743 \pm 2$	$-0.31 \pm 0.03$	(1600 to 1870) K
mean of recommended literature	various	$1760 \pm 90$	$-0.3 \pm 0.2$	(1270 to 2200) K

The motivation of this work was to gain new insights on the strongly spreading literature of the surface tension of liquid nickel. Beforehand, slight variations of impurities of sample material delivered from different suppliers was presumed to contribute to this spread. This assumption became doubtful already during the literature research in Section 5.1 as no purity related trend was evident in literature. Though, the spread was able to be minimised after excluding EML studies where outdated OD evaluation formulas, except *CB(5.20)UA* and *CB(5.20)A*, have been used. Finally, at evaluating the obtained measurement data within this work, no variation in surface tension according to different suppliers could be verified. The acquired surface tension data are in a good agreement with the recommended literature, except for the results of *Aziz* [4]. This initially drastic difference of around 7% in the obtained surface tension data, raised the question why there can be such a huge inconsistency between measurements performed on the same material (partly even the same LOT number) when measuring on the same EML apparatus. After re-evaluating the original data, this issue could be resolved very fast: At that time, *Aziz* erroneously identified the translational frequencies in the Fourier transformed data. The re-evaluation

## 5.4 Conclusion

decreased the surface tension results obtained by *Aziz* by 8%, so that these results are even 1.3% lower than the measurement data within this work. Finally, the bandwidth of the recommended literature was reduced to  $\pm 5\%$  compared to the primary  $\pm 7\%$ . In addition, the surface tension at the melting temperature was lowered by 2%.

In Chapter 6 an extensive uncertainty analysis is performed.



# 6 Uncertainty Analysis

Unless otherwise stated, uncertainties given in this thesis are expressed by the expanded uncertainty (coverage factor of  $k = 2$ ) in accordance with the *Guide to the expression of uncertainty in measurement* (GUM) [42].

## 6.1 Influencing factors

In Figure 6.1 numerous parameter or factors are visualised, which possibly or definitely affect the surface tension results for the special case of measurements with an EML apparatus and the usage of OD method. Those influences might either occur directly at measuring or afterwards at evaluation, which is discussed in detail in the following subsections.

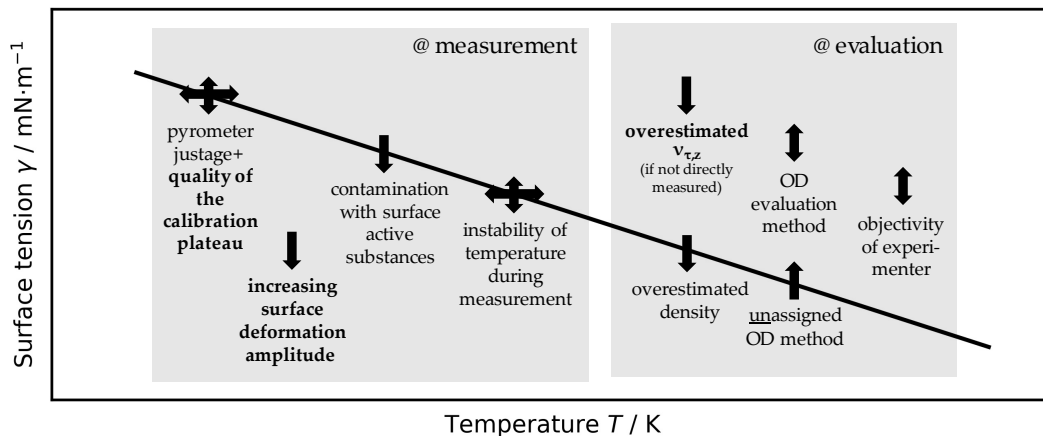


Figure 6.1: Various influencing factors at the surface tension measurement and evaluation especially for the method of EML.

### 6.1.1 Influences at measurement

#### Pyrometric challenges

This subsection is discussed by the example of nickel.

The temperature calibration is performed using the signal of the 1-colour-pyrometer. As explained in Section 6.1.1, the calibration is executed at a phase change plateau visible in the pyrometer signal as a function of time, that can be matched to a known, externally determined real temperature. For pure metals melting and solidification temperatures are equal, but this can not be observed by the pyrometer readings at the plateaus. By the example of the performed experiments with nickel, the pyrometer reading of the melting plateau arose in a bandwidth of  $(1319 \pm 9)$  K, whereas pyrometer readings of the solidification plateaus are with  $(1300 \pm 20)$  K in mean 20 K lower, but exhibit a higher spread. The inequality might either be caused by the variation of normal spectral emissivities for different temperatures, sample shapes and maybe also surface structure during solidification, a deviation of the thermodynamic equilibrium by finite heating rates or different concentration of surfactants at both plateaus.

The choice of the melting plateau for temperature calibration was made due to the increased reproducibility of the pyrometer reading on the plateau. In fact, the expression "plateau" might not be the perfect description, as the pyrometer signal usually exhibits a slightly positive slope during melting. As reference point, the pyrometer reading at the end of the plateau, followed by a discontinuity in slope, is chosen as the sample is already melted at this point and therefore providing a spherical shape and therefore the desired normal spectral emissivity.

After inverting the temperature profile for one experiment of nickel in the way that measurements started at low temperature and the experiment ended at high temperatures, a untypical low pyrometer reading at the melting plateau was observed. In order to follow the question if there might be a correlation between heating rates and pyrometer readings of the plateaus, heating rates of all experiments have been evaluated and plotted regarding their plateau temperatures. This is visualised in Figure 6.2 by additionally

## 6.1 Influencing factors

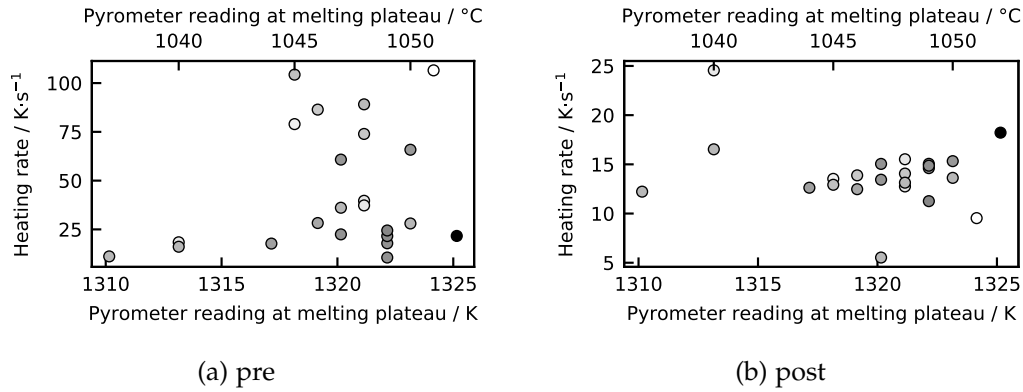


Figure 6.2: Dependence of pyrometer reading at the melting plateau from the heating rate for nickel. The heating rate has been determined prior (pre) and after (post) the plateau. The point shadings represent the sample mass in the range of (360 to 727) mg with light colours denoting low sample masses.

indicating the mass of the sample by the shadings of the measurement points. For this purpose heating rates were evaluated prior (pre) and after (post) the melting plateaus.

Heating rates prior to the plateau (Figure 6.2a) are typically higher than those after the plateau (Figure 6.2b), but no distinct correlation can be verified. To eliminate a possible distortion of the correlation due the influence of mass, mass specific heating rates were obtained and displayed in Figure 6.3.

But also for this case no functional relation between those measures could be verified. Nevertheless, low heating rates should be facilitated in order approach thermal equilibrium as far as possible. Thus the uncertainty of the pyrometer reading of the melting plateau has been specified to 10 K, which has been determined statistically. For the highest temperature measured, roughly 1850 K, uncertainty reaches a value of 20 K. The main contribution to uncertainty (index of 93 %) arises from the pyrometer reading at the melting temperature. Performing the temperature calibration for the highest pyrometer readings occurring at measurement of 1389 K one time with the typical plateau reading 1319 K and the other time with the worst-case plateau reading 1309 K (10 K lower), gives calibrated temperatures of 1850 K

## 6 Uncertainty Analysis

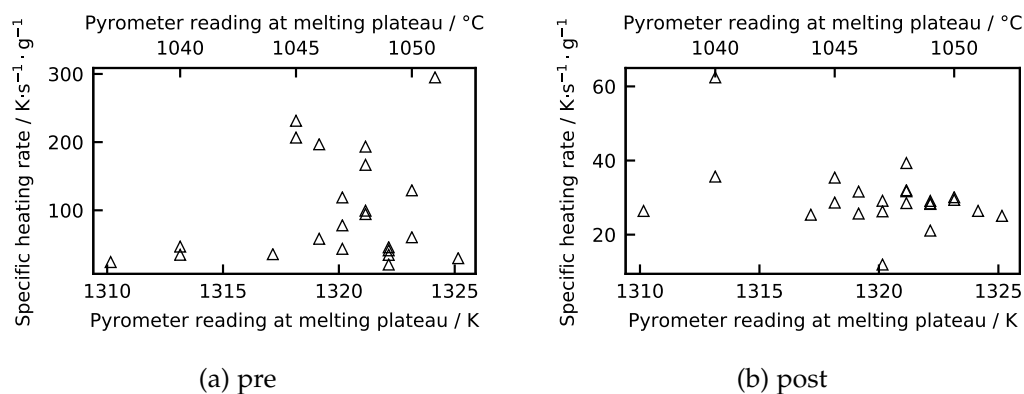


Figure 6.3: Dependence of pyrometer reading at the melting plateau from the mass specific heating rate, which takes also the mass into account, for nickel.

and 1870 K. This worst-case difference in calibrated temperature of 20 K corresponds to an increase of  $6 \text{ mN} \cdot \text{m}^{-1}$  or 0.4 % on surface tension. For materials with a stronger temperature dependent surface tension (steeper slope), uncertainty may further increase.

### Surface active elements

Contamination of samples with surfactants like oxides or sulphur, decrease the measured surface tension strongly [6] and also affects pyrometric temperature acquisition as the normal spectral emissivity is increased drastically. When certain contamination levels are exceeded, samples can impossibly be melted as the outer oxide monolayers posses an elevated melting point. This effect was observed at *W360* samples where no surface treatment had been performed before levitation. To counteract, *W360* samples were polished before incorporation to the experimental chamber. In order to prevent additional oxide formation during levitation, the oxygen content of cooling gases, which exhibit low oxygen partial pressures from the start, is further decreased by factor of  $10^3$  through the implementation of an oxygen filter. By the admixture of hydrogen, surface oxides are possibly reduced. Further details of the levitation atmosphere are stated in Section 3.1.4.

## 6.1 Influencing factors

The distinct quantification of surface active elements during measurement is a difficult task. For example, the working group of *Ozawa* [53] tracks oxygen partial pressures at experimentation. But a definite quantification of oxide contents of the samples can only be performed before and after levitation through a chemical analysis or *energy dispersive x-ray spectroscopy* (EDX). Some suppliers state typical impurities of surfactants in the certificate of analysis, but the majority gives only a trace metal analysis. Regarding to this work, *Alfa Aesar* quotes a typical oxygen content of 5 ppm and a typical sulphur content of 2.5 ppm. The corresponding certificate of analysis is attached in the appendix (Chapter 7). Within this thesis no additional chemical quantification of surfactant was performed, but the oxygen content of the atmosphere at the start of levitation was estimated. This was calculated for maximal pressure of 850 mbar during experimentation and initial evacuation pressure in the  $10^{-6}$  mbar regime by the stated oxygen impurities and the reduction factor of  $10^{-3}$  by the oxygen filter. For nickel experiments, the initial oxygen partial pressure at levitation was estimated to  $\leq 2 \times 10^{-6}$  mbar and for *W360*  $\leq 2 \times 10^{-5}$  mbar.

### Temperature control

Measurements at stable temperatures give peaks with narrow bandwidths in oscillation spectra that give surface tension results with a high accuracy and small uncertainties. Temperature drifts result in a broadening of oscillation spectra as shifts are induced, whereas strong fluctuations cause a broadening independent of the direction. The implementation of the mass flow controller enhanced the accuracy in temperature regulation and thus also in temperature stability. For nickel, the pyrometer signal for a single surface tension and density measurement was determined by calculating the mean and the expanded uncertainty in the time range of the measurement from the pyrometer signal of the whole measurement. For the earlier *W360* measurements, the pyrometer signal at the start of the measurement has been noted by hand for further temperature calculations, which was prone to errors through twisted numbers or temperature drifts.

In order to further increase temperature stability, a PID-controller (proportional–integral–derivative controller) could be installed to the experimental setup.

## 6 Uncertainty Analysis

### Change in composition

A change in chemical composition concerns only alloys as the evaporation rate differs for each metal. The evaporation rate depends predominately on the vapour pressure of the metals, surface coverage and the corresponding temperature that the sample exhibits. Figure 6.4 shows vapour pressures of eleven metals common in alloys. Evaporation during  $W_{360}$  experiments were not apparent by eye, but it is assumed that the weight fraction of manganese with initial 0.25 % rapidly decreases due to its high vapour pressure and the intrinsic stirring evoked by the method of EML. A quantification of mass fractions of the distinct metals was not performed. To minimise changes in chemical composition, levitation time should be kept low.

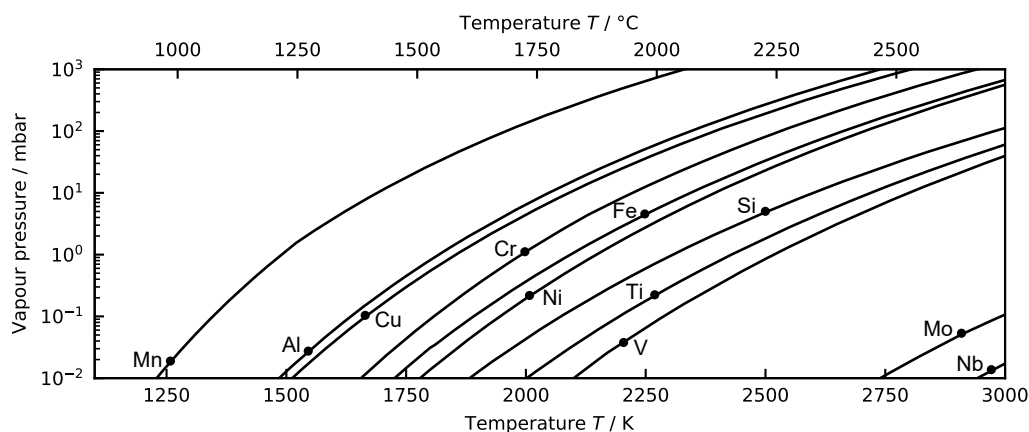


Figure 6.4: Vapour pressure of selected metals in dependence of temperature. The dots on the curves are only relevant for labelling. Data source: [62]

### Surface deformation amplitudes

Surface oscillations with a finite deformation amplitude induce negative frequency shifts, which further lead to a decrease in the surface tension measurement result. This is caused by the rising non-linear effects for larger surface deformation amplitudes, which have not been taken into account at deriving the fundamental formulas of the *Oscillating Drop* (OD) method.

## 6.1 Influencing factors

Research in this topic is still at the beginning, but for example *Xiao, et al.* [63] investigated the influence of the surface deformation amplitude of the steel *LEK-94*<sup>1</sup> by  $\mu\text{g}$ -EML<sup>2</sup> onboard of the ISS (international space station). They observed that a radial deformation of 5 % leads to a frequency shift of about  $-1$  %. Two reasons raise difficulties in comparing radial deformation obtained by *Xiao, et al.* and this study: The first is the inequality of the investigated material and the second reason is connected to the differently excited oscillation modes for  $\mu\text{g}$ - and terrestrial EML. At  $\mu\text{g}$ -EML intentionally only the  $m = 0$  mode is excited, which leads to a well quantifiable radial deformation along one distinct axis. As radial deformation is obtained in general by observation of the sample projection in the horizontal plane, the quantification of real deformation amplitudes cannot be directly compared with the observed ones. For the case of terrestrial EML, the observed amplitudes of 5 % are estimated to correspond to total deformations in a range between (3 to 5) % at the occurrence of mixed modes. [63–65]

The following estimation of the influence of the surface deformation on the surface tension is only performed on nickel.

In order to estimate the surface deformation for measurements performed within this thesis, the time dependent radii of all angles in  $5^\circ$  steps used for evaluation were plotted as presented in Figures 6.5 and 6.6. To quantify deformation amplitudes obtained from observation of the horizontal projection, two simple approaches were used:

1.  $\delta_{\text{mean}}$  gives the mean symmetrical radial deformation of the extrema of each angle<sup>3</sup>.
2.  $\delta_{\text{min-max}}$  gives the percentage of the difference of the maximal and minimal amplitude used for evaluation, which can further be seen as total worst-case peak-to-peak deformation.

---

<sup>1</sup>The typical chemical composition of the nickel-based super alloy *LEK-94* has been stated with 64 % Ni, 15 % Al, 7 % Co, and 7 % Cr.

<sup>2</sup> $\mu\text{g}$ -EML denotes EML under microgravity ( $\mu\text{g}$ ) conditions.

<sup>3</sup>In more detail, minimal and maximal radii of all angles are calculated for each time step. These are averaged separately and afterwards again the mean is calculated from these two quantities.

## 6 Uncertainty Analysis

In Figure 6.5a an exemplary course of radii as a function of time is visualised. Therein,  $\delta_{\text{mean}}$  seems to be underrepresented, but after zooming in time scale (Figure 6.5b), the origin of  $\delta_{\text{mean}}$  is clear. Figures 6.6a and 6.6b are examples for comparable low and high radial deformations, respectively. In general  $\delta_{\text{mean}}$  occurred in a range of (0.8 to 3.5) %, which corresponds to a mean of about  $(1.9 \pm 0.8)$  %. The worst-case estimation of the peak-to-peak deformation amplitude  $\delta_{\text{min-max}}$  gave 4 % and 24 % at minimum and maximum, respectively. In mean a  $\delta_{\text{min-max}}$  of  $(13 \pm 5)$  % was attained.

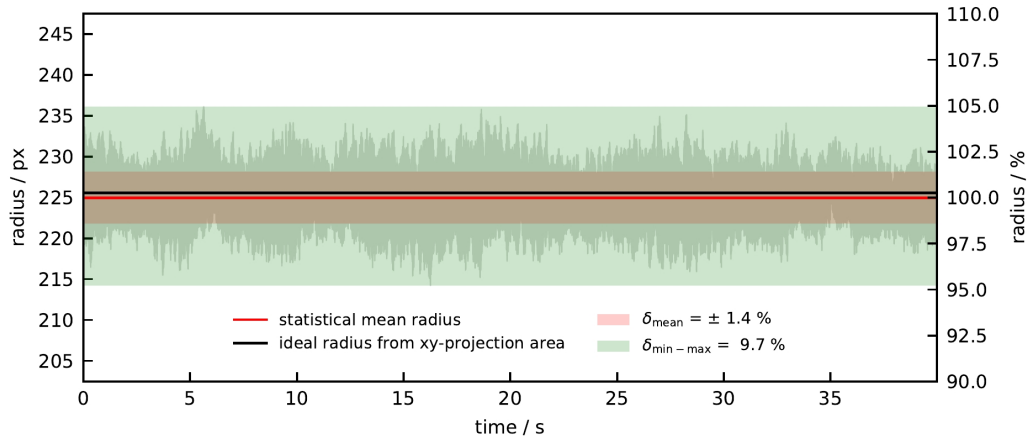
As the re-evaluated data originally obtained by *Aziz, et al.* [4], see Section 5.3, are compared to surface tension measured within this study 1.3 % lower, a possible correlation with increased surface deformation at measurements from *Aziz* is investigated. Unfortunately, edge detection was performed incorrect sometimes for one specific angle, which has no effect on the surface tension results, but may distort the statistic of radial deformation. For this reason, only selected measurements were used for the following statistic:  $\delta_{\text{mean}}$  was observed in the range of (2.6 to 3.5) %, which corresponds to a mean of  $(2.9 \pm 0.4)$  %. The minimum of the worst-case peak-to-peak deformation amplitude  $\delta_{\text{min-max}}$  is 14 % and the maximum 19 %. Accordingly the mean of  $\delta_{\text{min-max}}$  was determined to  $(16 \pm 3)$  %. Consequently,  $\delta_{\text{mean}}$ , as well as  $\delta_{\text{min-max}}$  is increased by roughly 50 % and 25 % at the measurements performed by *Aziz, et al.* in respect to the ones of this work. Therefore, the possibility cannot be ruled out that the increased surface deformation at the study performed by *Aziz* partly causes the surface tension lowering of 1.3 %.

In order to give a vague estimation of a possible influence of the finite surface deformation on the surface tension for measurements obtained by this thesis, an observed deformation amplitude of roughly 5%<sup>4</sup> would give an increase in surface tension of about 2 % due to the negative frequency shift of 1 %.

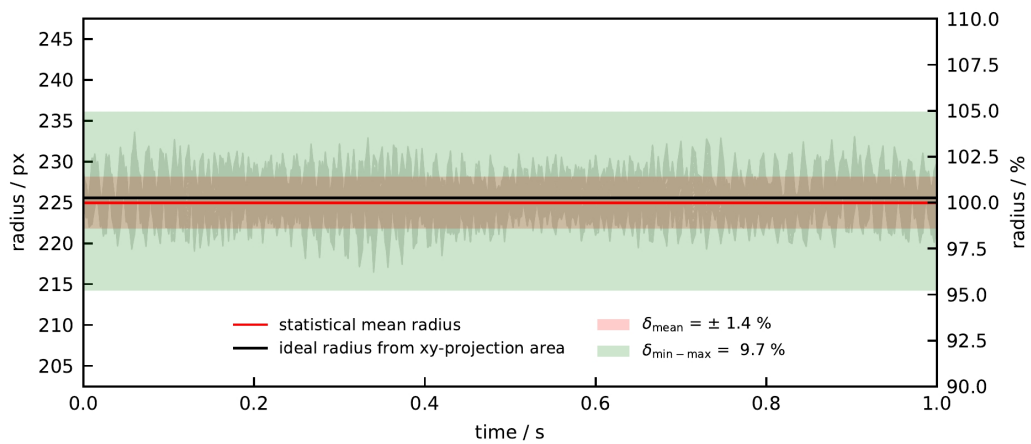
---

<sup>4</sup>This is obtained by the worst-case estimation of the obtained surface deformation by the half of the mean peak-to-peak measure  $\frac{\bar{\delta}_{\text{min-max}}}{2} = \frac{13\%}{2} \approx 5\%$ .

## 6.1 Influencing factors



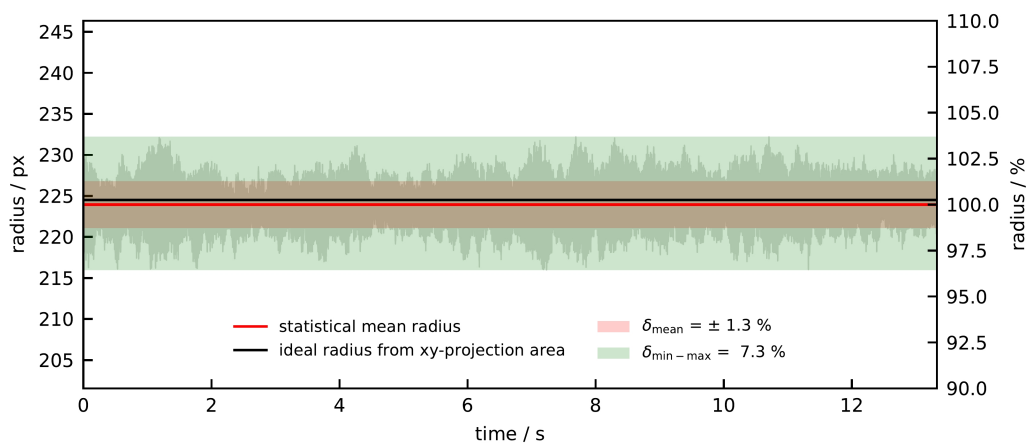
(a) Time period used for surface tension evaluation



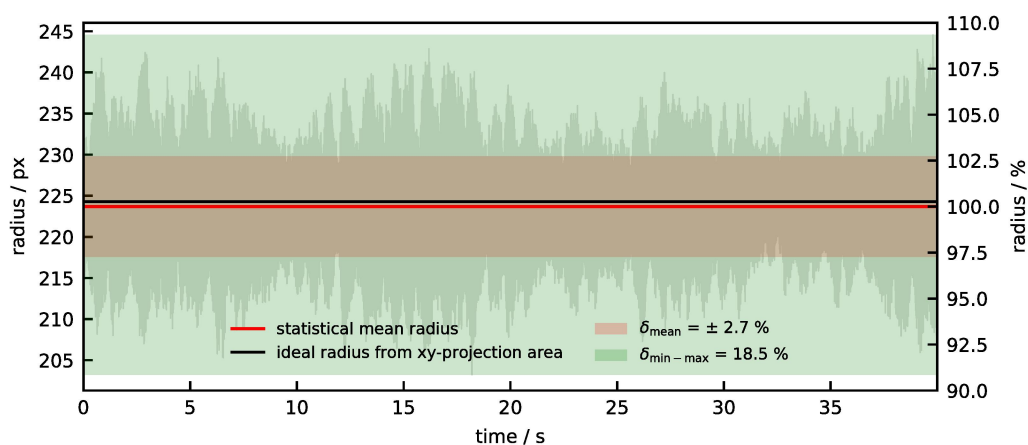
(b) First second of time period used for surface tension evaluation

Figure 6.5: Typical radial deformation  $R(t)$  in the horizontal plane in dependence of time  $t$  by the example of nickel sample AA#2 (ID according to Table 5.5) at a temperature of 1759 K - radii are given in the units of pixel (px) and %

## 6 Uncertainty Analysis



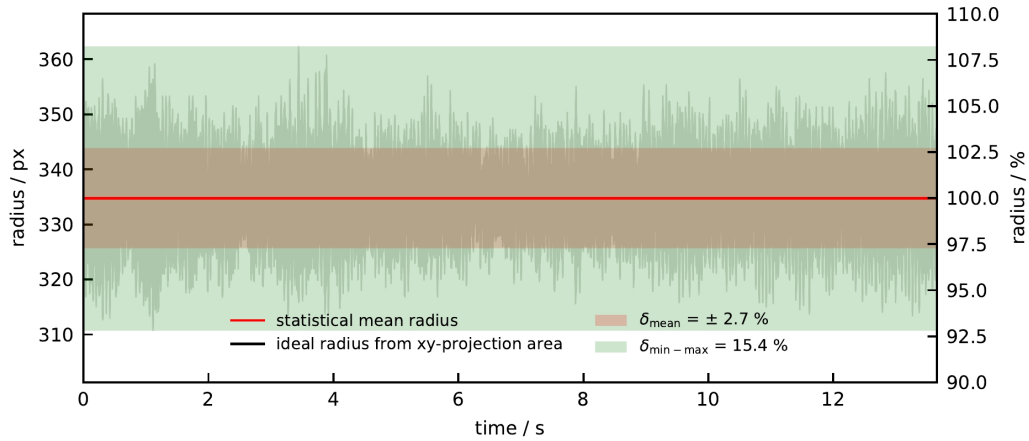
(a) Compareable low radial surface deformation (1753 K)



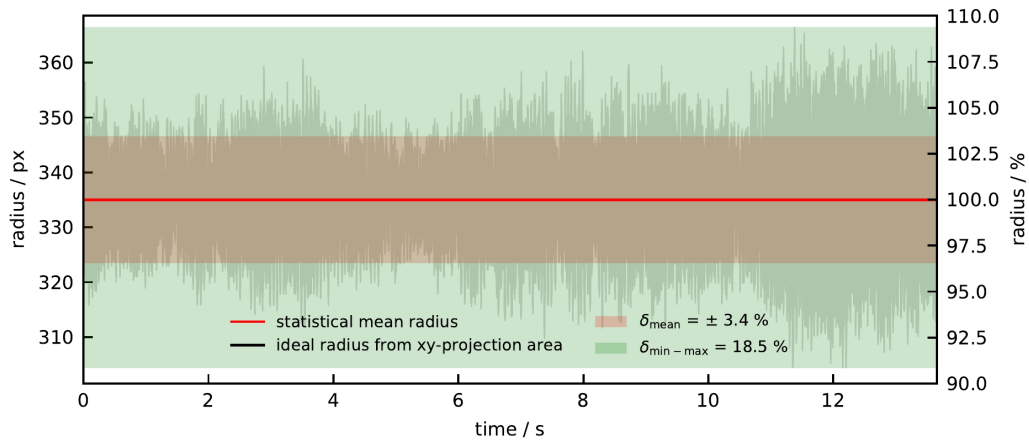
(b) Compareable high radial surface deformation (1780 K)

Figure 6.6: Extremal radial deformation  $R(t)$  in the horizontal plane in dependence of time  $t$  by the example of nickel sample AA#2 (ID according to Table 5.5) - radii are given in the units of pixel (px) and %

## 6.1 Influencing factors



(a) Compareable low radial surface deformation of measurements performed by Aziz (1760 K)



(b) Compareable high radial surface deformation of measurements performed by Aziz (1774 K)

Figure 6.7: Exemplary radial deformation  $R(t)$  in the horizontal plane in dependence of time  $t$  from nickel measurements performed by Aziz [4] - radii are given in the units of pixel (px) and %

## 6 Uncertainty Analysis

### 6.1.2 Influences at evaluation

Here, problems are discussed which arise at evaluation and the question is raised which parts of the evaluation depend strongly on the perception and experience of the experimenter.

#### Evaluation method

The dependence of OD evaluation formulas used is already discussed extensively in Section 5.1. When taking a closer look to the difference of surface tension  $\gamma_{UA}$  and  $\gamma_A$  resulting from formulas  $CB(5.20)UA$  and  $CB(5.20)A$  respectively (according to Table 5.1), Equation 6.1 shows that only the single rotational splittings of the  $m$  modes and the absolute value of the sample mass contribute to the elevated surface tension results of the unassigned formula  $CB(5.20)UA$ .

$$\begin{aligned}\Delta\gamma &= \gamma_{UA} - \gamma_A \\ \Delta\gamma &= \frac{3}{8}\pi M \left[ \frac{1}{5} \left( \sum_{m=+2}^{-2} v_{2,m}^2 - v_{2,0}^2 - 2v_{2,|1|}^2 - v_{2,|2|}^2 \right) \right] \\ \Delta\gamma &= \dots \\ \Delta\gamma &= \frac{3}{80}\pi M \left[ (v_{2,-1} - v_{2,+1})^2 + (v_{2,-2} - v_{2,+2})^2 \right] \quad (6.1)\end{aligned}$$

$\Delta\gamma$	...	difference in surface tension / $N \cdot m^{-1}$
$\gamma_{UA}$	...	surface tension obtained from $CB(5.20)UA$ / $N \cdot m^{-1}$
$\gamma_A$	...	surface tension obtained from $CB(5.20)A$ / $N \cdot m^{-1}$
$M$	...	mass / kg
$v_{2,m}$	...	oscillation frequency of $l = 2, m$ -mode / Hz

The impact of this difference for the data obtained by *Aziz*, is discussed in Section 5.3.

### Determination of translational frequency in z-direction

The method for obtaining translational frequencies in the vertical direction  $\nu_{\tau,z}$  is rarely described in publications. Most of the EML setups only contain the camera required for surface tension measurement. As this one observes the sample projection only in the horizontal plane  $\nu_{\tau,z}$  have to be estimated. Sometimes a direct determination through a camera observing a projection in a random vertical plane is not even possible, hence the lower coils designed in the manner that samples are positioned partly below the upper coil windings. In Section 5.3 the fatal consequences on the surface tension results are described in detail. So a mean increase of  $\nu_{\tau,z}$  from 5.9 Hz to 14.6 Hz, which corresponds to 150%, caused a decrease in surface tension of 5.5% by the use of *CB(5.20)UA* according to Table 5.1. To prevent misidentifications projections in a random vertical plane should be recorded synchronised to surface tension records.

### Mass loss model

As the sample mass cannot be monitored during measurement, an estimation of the actual mass at the measurement has to be made. This is based on the knowledge of sample masses before and after levitation, which are denoted as  $m_s$  and  $m_e$  respectively. From this only a mass loss can be calculated, but to obtain an estimate for the mass at the measurement  $i$  of all  $N$  measurements some model has to be applied.

For the steel *W360*, mass losses  $m_{\text{loss}}$  emerged in the range of  $(4 \pm 4)$  mg and for nickel in  $(0.4 \pm 0.5)$  mg respectively. At the begin of this work, a simple mass loss model was in use, where the mass of measurement  $i$ ,  $m_i$ , is calculated in accordance to Equation 6.2. In the following, times are denoted by  $t$  by use of the same indices as masses  $m$ .

$$m_i(t_i) = m_s - \frac{i}{N} m_{\text{loss}} \quad (6.2)$$

## 6 Uncertainty Analysis

In the course of investigating nickel, a new mass loss model has been introduced. This model is stated in Equation 6.3 and takes also the accomplished time dependent temperature profile  $T(t)$  of the whole experiment into account.

$$m_i(t_i) = m_s - \frac{\int_{t_s}^{t_i} T(t) dT}{\int_{t_s}^{t_e} T(t) dT} m_{\text{loss}} \quad (6.3)$$

As suggested by Thomas Leitner, the mass loss model could be improved for further measurements by considering only the time where the sample is in the liquid state and by subtracting the lowest temperature occurring in this period from the profile in order to elevate the influence of temperature alterations that happen above the melting temperature. Equation 6.3 has no theoretical background, so it is just an estimate without proof due to the lack of theoretical approaches for EML setups. For ESL, *Lee and Matson* [33] suggested to estimate the rate of mass evaporation of a liquid metal by *Langmuir's* equation. Therein, also a similar formula for multicomponent alloys is stated. But both cannot be adopted for EML since the pressure in the experimental chamber is higher by a factor of  $10^{10}$ , which leads to the formation of a gaseous interfacial layer between sample and levitation atmosphere.

In the uncertainty analysis of surface tension for nickel that was performed in accordance to GUM, mass uncertainty (extended uncertainty with a coverage factor of  $k = 2$ ) had the universal value  $\Delta m = 0.5$  mg. This is predominately arising from the margin of mass loss, which is estimated by the typical appearing mass loss value of 0.5 mg as this is acting like a maximum limiting factor. The uncertainty of the precision balance is even smaller. For this reason, a conventional GUM conform uncertainty analysis of Equation 6.2 or 6.3 is not sufficiently informative. Model errors cannot be included, only uncertainties of the precision balance.

By contending that, assuming the highest possible uncertainty can be justified as long as no prove of this or any other approach is gained. Indeed, adjusting  $\Delta m$  to the mass loss of the corresponding measurement instead of using the fixed typical value could increase precision in uncertainty estimation, thus can be implemented in future studies. To delve deeper into the subject of mass loss phenomena would go beyond the scope of this

## 6.1 Influencing factors

work. The sample mass has in fact in total a low contribution to the GUM uncertainty budget of surface tension (Table 6.2). For a sample with 516.1 mg the absolute uncertainty contribution is  $\sim 1 \text{ mN} \cdot \text{m}^{-1}$ , that corresponds to an index of 0.4%. Therefore the uncertainty arising from mass loss only would be lower than 0.4%.

In addition, mass loss has been set in dependence to levitation time for both investigated materials, but Figure 6.8 shows that there is no clear functional relation. Dots with a white shading denote high starting masses.

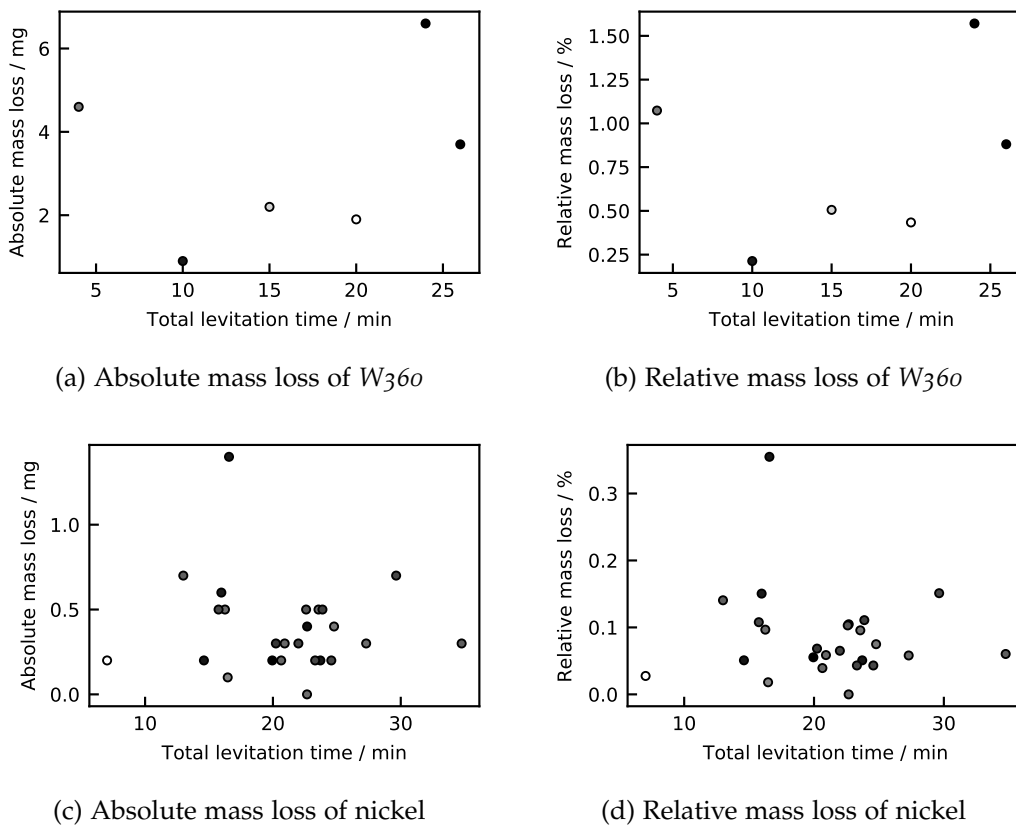


Figure 6.8: Absolute and relative mass loss in dependence of total levitation time for measurements of steel W360 and nickel show no functional relation. Points with a bright shading correspond to high starting masses.

## 6 Uncertainty Analysis

The dependence of the mass loss with the integral over the temperature profile  $\int T dt$  has been evaluated for nickel and is presented in Table 6.9. This enables testing the validity of Equation 6.3. At first sight no distinct correlation can be identified, but it is evident that for low  $\int T dt$  mass losses exhibit a huge difference caused by the initial sample mass. This shows clearly the influence of the surface size and the surface-to-volume-ratio: Samples with high surface-to-volume-ratios suffer more from mass evaporation than samples with a small surface-to-volume-ratio. From this point of view, samples with small surface-to-volume-ratios should be used preferably, which are then in turn prone to decreased surface tension caused by elevated surface deformation amplitudes (see Section 6.1.1). So, an acceptable compromise has to be found. Further measurements with equal starting masses over a broad range of  $\int T dt$  are required to investigate possible correlations.

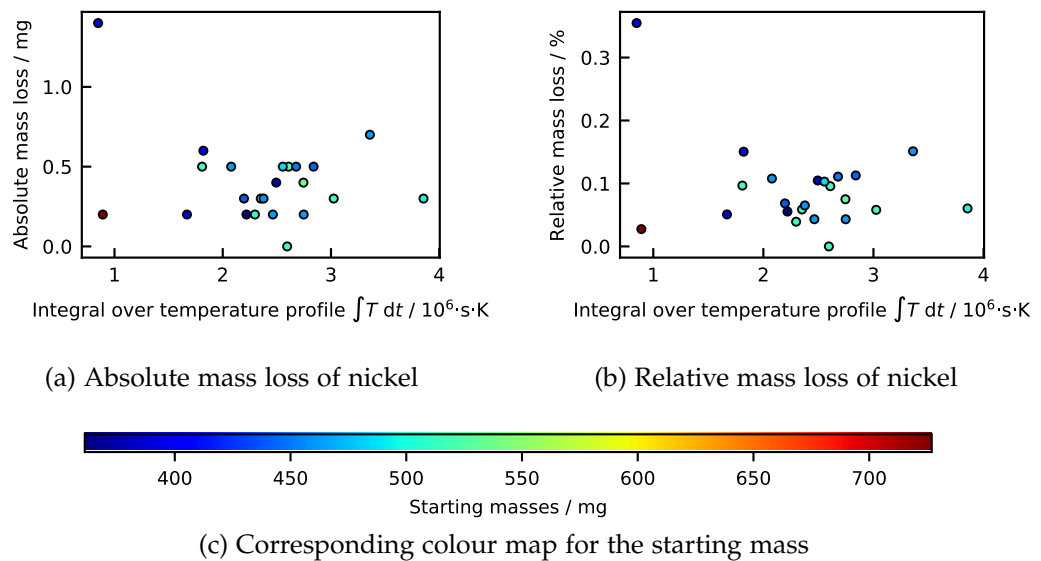


Figure 6.9: Absolute and relative mass losses of nickel in dependence of the integral over the time dependent temperature profile for nickel. The colouring of the single data points is correlated to the starting mass.

### Temperature calibration formula

In Section 2.4 and 3.2.3 temperature measurement and evaluation is described in detail. In order to avoid high computational efforts at temperature calibration, *Wien's* law of spectral radiance is used instead of *Planck's* radiation law (Equation 2.16). For increasing wavelengths, *Wien's* law exhibits an increased deviation from *Planck's* law. Regardless, the use of *Wien's* law is justified if the condition  $\lambda T \ll c_2$  is satisfied. Considering the highest occurring temperature  $T_{\max, W360}$  of about 1960 K, the central wavelength  $\lambda$  of the 1-colour-pyrometer of  $1.625 \mu\text{m}$  and the characteristic constant  $c_2 = \frac{ch}{k} \approx 0.0144 \text{ m} \cdot \text{K}$ ,  $\lambda T \ll c_2$  is satisfied with a  $\lambda T_{\max}$  of  $0.0032 \text{ m} \cdot \text{K}$ . For Nickel,  $\lambda T_{\max}$  would even give a lower value of  $0.0030 \text{ m} \cdot \text{K}$  with a  $T_{\max, \text{Ni}}$  of about 1850 K. Accordingly, this influencing factor has an insignificant effect on temperature uncertainty and is not included in calculation.[20]

## 6.2 Statistical reproducibility

In order to quantify the reproducibility of measurement and evaluation, the surface tension  $\gamma$  was measured at a constantly held temperature  $T$ , as far this was possible by manually controlling of the cooling rate of the gas flow. The result of this measurement series is presented in Figure 6.10. For all data points the uncertainties were obtained to  $\Delta T = 20$  K and  $\Delta\gamma = 30$  mN · m<sup>-1</sup>. The statistical spread of the data was determined to  $\bar{T} = (1735 \pm 4)$  K and  $\bar{\gamma} = (1739 \pm 2)$  mN · m<sup>-1</sup>.

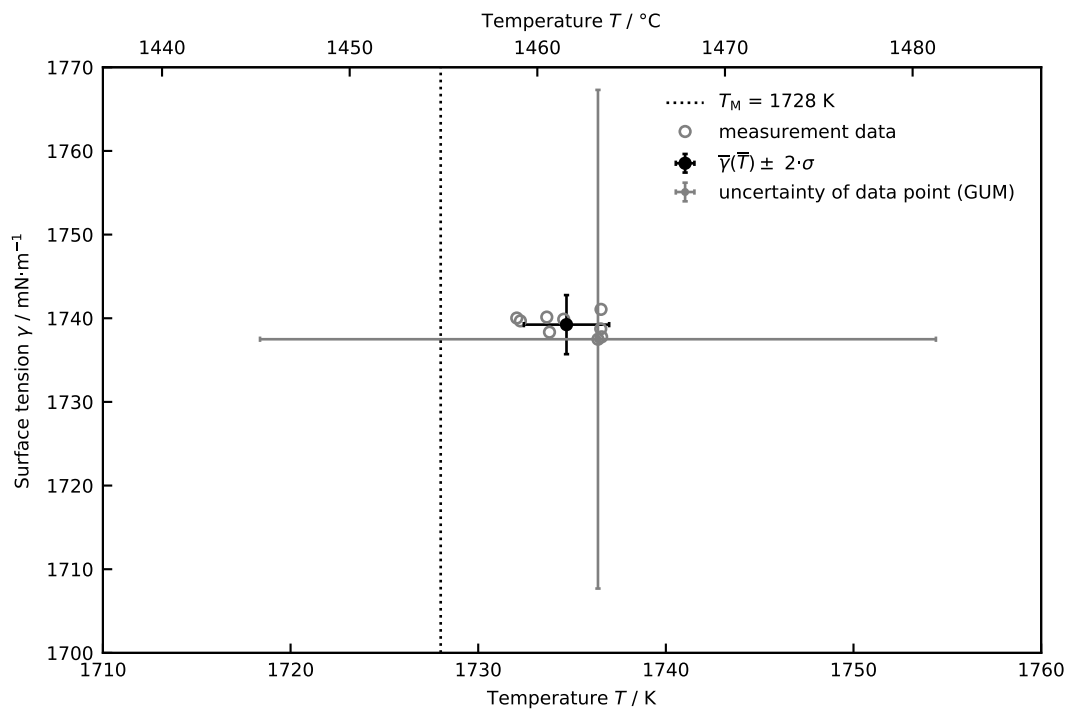


Figure 6.10: The statistical spread of measurement and evaluation is significantly smaller than the uncertainties of the single data points. During experimentation it was tried to keep temperature stable at about 1735 K.  $2\cdot\sigma$  denotes the expanded uncertainty obtained by GUM.

## 6.3 Uncertainty budget

The program *GUM Workbench 2.4* was used for the assessment of measurement uncertainties in accordance with the *Guide to the expression of uncertainty in measurement* (GUM) [42]. In Tables 6.1 and 6.2 exemplary GUM uncertainty budgets for surface tension measurements are presented for *W360* and nickel, respectively. Therein, quantities including standard uncertainties ( $k = 1$ ), sensitivity coefficients, standard uncertainty contributions and indexes are quantified. Quantities  $x_i$  refer to all measurands with  $i$  ranging from 1 to  $N$ . In order to determine surface tension by Equation 3.3, the following 12 quantities are used (as in GUM uncertainty budgets in Tables 6.1 and 6.2):

$M$	...	sample mass
$\nu_{\tau,m}$	...	3 translational frequencies in directions $m = x, y$ and $z$
$\nu_{2,m}$	...	5 oscillation frequencies in the $l = 2$ and $m = -2$ to $+2$
$\rho_M, \frac{\partial \rho}{\partial T}, T$	...	parameter for calculating density $\rho$ at temperature $T$ according to Equation 3.2

Constant input quantities as melting/liquidus temperature or gravitational constant are not stated here, explicitly.

The previously listed quantities each possess a standard uncertainty (coverage factor  $k = 1$ ) denoted as  $u(x_i)$ , which corresponds to the "Type B" of standard uncertainties as  $u(x_i)$  was estimated for each measurand. In contrast "Type A" standard uncertainties are statistically obtained and have to be treated differently.

In order to determine the combined standard uncertainty  $u_c(\gamma)$  of one particular surface tension measurement, Equation 6.4 has to be applied. [42]

$$u_c(\gamma) = \sqrt{\sum_{i=1}^N \left( \frac{\partial \gamma}{\partial x_i} u(x_i) \right)^2} \quad (6.4)$$

Parts of Equation 6.4 can be identified as sensitivity coefficients  $\frac{\partial \gamma}{\partial x_i}$  and the standard uncertainty contribution  $\frac{\partial \gamma}{\partial x_i} u(x_i)$ , which are also stated in

## 6 Uncertainty Analysis

the GUM uncertainty budget. In addition, also the contribution index of quantity  $x_i$  to the combined uncertainty  $u_{c(\gamma)}$  is assessed by Equation 6.5 [66].

$$\text{Index: } \frac{\left(\frac{\partial \gamma}{\partial x_i} u(x_i)\right)^2}{\sum_{i=1}^N \left(\frac{\partial \gamma}{\partial x_i} u(x_i)\right)^2} \quad (6.5)$$

In this thesis uncertainties are stated almost exclusively in the expanded form with a coverage factor  $k$  of 2 instead of 1 as for the combined standard uncertainty in Equation 6.4. The difference between those uncertainties is the confidence level, which is about 68 % for  $k = 1$  and about 95 % for  $k = 2$ . Expanded uncertainties  $U$  of the output quantity  $y$  are determined by means of Equation 6.6 [66].

$$U = 2u_c(y) \quad (6.6)$$

In both cases, steel  $W360$  and nickel, it is evident that the five oscillation frequencies  $\nu_{2,m}$  nearly exclusively dominate the uncertainty contribution with indices of about 20 % each. For the uncertainty budget of nickel the contribution of the translational frequency in vertical direction  $\nu_{\tau,z}$  increased by 10 % in index. This was evoked by the increased standard uncertainty for determining  $\nu_{\tau,z}$  due to the latest findings referred to Section 5.3 and the method of determination, which is not the most exact and most reliable one.

### 6.3 Uncertainty budget

Table 6.1: GUM uncertainty budget of one selected data point of  $W_{360}$  measurements (sample #3 according to Table 4.3). All uncertainties have been estimated ("Type B") and input quantities are presumed to follow a normal distribution, except for the mass  $M$  which is assumed to follow a rectangular distribution. This results in a surface tension of  $\gamma = (1750 \pm 30) \text{ mN} \cdot \text{m}^{-1}$  when using the expanded uncertainty. As uncertainties have been estimated by use of the expanded uncertainty,  $M$ ,  $\nu_{\tau,x}$ ,  $\nu_{\tau,y}$ ,  $\nu_{\tau,z}$  and  $\rho_L$  contain one additional significant number to enable reproducing the original expanded uncertainty.

$x_i \pm u(x_i)$	$\frac{\partial \gamma}{\partial x_i}$	$\frac{\partial \gamma}{\partial x_i} u(x_i)$	Index
$x_i \pm u(x_i)$ ... quantity with standard uncertainty ( $k = 1$ )			
$\frac{\partial \gamma}{\partial x_i}$ ... sensitivity coefficient			
$\frac{\partial \gamma}{\partial x_i} u(x_i)$ ... standard uncertainty contribution / $\text{mN} \cdot \text{m}^{-1}$			
$M = (435.00 \pm 0.25) \text{ mg}$	$4.1 \times 10^{+3}$	1.2	0.7 %
$\nu_{\tau,x} = (4.30 \pm 0.25) \text{ Hz}$	$-1.2 \times 10^{-3}$	-0.31	0.0 %
$\nu_{\tau,y} = (4.30 \pm 0.25) \text{ Hz}$	$-1.2 \times 10^{-3}$	-0.31	0.0 %
$\nu_{\tau,z} = (11.17 \pm 0.25) \text{ Hz}$	$-3.2 \times 10^{-3}$	-0.79	0.3 %
$\nu_{2,0} = (60.3 \pm 0.5) \text{ Hz}$	$1.2 \times 10^{-2}$	6.2	20.1 %
$\nu_{2,-1} = (56.9 \pm 0.5) \text{ Hz}$	$1.2 \times 10^{-2}$	6.2	20.0 %
$\nu_{2,+1} = (63.3 \pm 0.5) \text{ Hz}$	$1.2 \times 10^{-2}$	6.2	20.0 %
$\nu_{2,-2} = (53.0 \pm 0.5) \text{ Hz}$	$1.2 \times 10^{-2}$	6.1	19.4 %
$\nu_{2,+2} = (65.6 \pm 0.5) \text{ Hz}$	$1.2 \times 10^{-2}$	6.1	19.4 %
$\rho_L = (7210 \pm 25) \text{ kg} \cdot \text{m}^{-3}$	$-2.8 \times 10^{-6}$	-0.069	0.0 %
$\frac{\partial \rho}{\partial T} = (-0.7 \pm 0.3) \text{ kg} \cdot \text{m}^{-3} \cdot \text{K}^{-1}$	$-2.8 \times 10^{-4}$	-0.083	0.0 %
$T = (1850 \pm 10) \text{ K}$	$1.9 \times 10^{-6}$	0.019	0.0 %

## 6 Uncertainty Analysis

Table 6.2: GUM uncertainty budget of one selected data point of nickel measurements (GF#3 according to Table 5.5). All uncertainties have been estimated ("Type B") and input quantities are presumed to follow a normal distribution, except for the mass  $M$  which is assumed to follow a rectangular distribution. This results in a surface tension of  $\gamma = (1740 \pm 30) \text{ mN} \cdot \text{m}^{-1}$  when using the expanded uncertainty. As uncertainties have been estimated by use of the expanded uncertainty,  $M$ ,  $\nu_{\tau,x}$ ,  $\nu_{\tau,y}$  and  $\frac{\partial \rho}{\partial T}$  contain one additional significant number to enable reproducing the original expanded uncertainty.

$x_i \pm u(x_i)$	$\frac{\partial \gamma}{\partial x_i}$	$\frac{\partial \gamma}{\partial x_i} u(x_i)$	Index
$x_i \pm u(x_i)$ ... quantity with standard uncertainty ( $k = 1$ )			
$\frac{\partial \gamma}{\partial x_i}$ ... sensitivity coefficient			
$\frac{\partial \gamma}{\partial x_i} u(x_i)$ ... standard uncertainty contribution / $\text{mN} \cdot \text{m}^{-1}$			
$M = (516.10 \pm 0.25) \text{ mg}$	$3.4 \times 10^{+3}$	0.98	0.4 %
$\nu_{\tau,x} = (5.40 \pm 0.25) \text{ Hz}$	$-2.9 \times 10^{-3}$	-0.72	0.2 %
$\nu_{\tau,y} = (5.40 \pm 0.25) \text{ Hz}$	$-2.9 \times 10^{-3}$	-0.72	0.2 %
$\nu_{\tau,z} = (12.4 \pm 0.4) \text{ Hz}$	$-6.6 \times 10^{-3}$	-2.6	3.0 %
$\nu_{2,0} = (55.5 \pm 0.5) \text{ Hz}$	$1.3 \times 10^{-2}$	6.7	19.5 %
$\nu_{2,-1} = (53.6 \pm 0.5) \text{ Hz}$	$1.3 \times 10^{-2}$	6.7	19.2 %
$\nu_{2,+1} = (56.7 \pm 0.5) \text{ Hz}$	$1.3 \times 10^{-2}$	6.7	19.2 %
$\nu_{2,-2} = (51.9 \pm 0.5) \text{ Hz}$	$1.3 \times 10^{-2}$	6.7	19.1 %
$\nu_{2,+2} = (58.1 \pm 0.5) \text{ Hz}$	$1.3 \times 10^{-2}$	6.7	19.1 %
$\rho_M = (7800 \pm 50) \text{ kg} \cdot \text{m}^{-3}$	$-2.2 \times 10^{-6}$	-0.11	0.0 %
$\frac{\partial \rho}{\partial T} = (-0.90 \pm 0.25) \text{ kg} \cdot \text{m}^{-3} \cdot \text{K}^{-1}$	$-4.0 \times 10^{-6}$	-0.001	0.0 %
$T = (1730 \pm 10) \text{ K}$	$1.9 \times 10^{-6}$	0.019	0.0 %

## 7 Outlook

In order to attain surface tension results with a higher accuracy and lower susceptibility to errors the following improvements in the experimental setup and data evaluation are suggested:

Probably the most important one for the EML setup of the *Thermophysics and Metalphysics Group* at *Graz University of Technology*, is the implementation of a synchronous determination of the translational frequency in the vertical direction. This may avoid misidentifications and drastic errors in the resulting surface tension as described in Section 5.3 and 6.1.2.

To reduce the uncertainties of the temperature measured and also the surface tension obtained, a PID-controller (proportional–integral–derivative controller) could be installed for an increased temperature control and stability during measurements.

In general, emphasis may also be put on further investigations of influencing factors at surface tension measurements for EML apparatuses. This comprises the quantification and impact of finite surface deformation amplitudes on surface tension under terrestrial conditions (Section 6.1.1), performing further test series to forecast mass losses on experimental basis (Section 6.1.2) and the quantification of the influence of sample purity (Section 6.1.1). In addition, it might be interesting to investigate the effect on surface tension if levitation is performed under a non-reducing atmosphere.



# Appendix

Legend of tables in this chapter:

$T$	...	temperature / K or °C
$\rho$	...	density / $\text{kg} \cdot \text{m}^{-3}$
$\gamma$	...	surface tension / $\text{mN} \cdot \text{m}^{-1}$
$\Delta T$	...	expanded uncertainty in temperature / K
$\Delta \rho$	...	expanded uncertainty of density / $\text{kg} \cdot \text{m}^{-3}$
$\Delta \gamma$	...	expanded uncertainty of surface tension / $\text{mN} \cdot \text{m}^{-1}$

## W360

In Table 7.1 and 7.2, density and surface tension data points of steel *W360* obtained within this study are summarised. Information regarding corresponding experimental parameter are given in Table 4.3. Expanded uncertainties were determined according to *GUM* [42]. In addition, exemplary data points of the obtained fitting equations are stated in Table 7.3.

Table 7.1: Density data points of steel *W360* obtained at this thesis.

sample	$T / \text{K}$	$T / ^\circ\text{C}$	$\rho$	$\Delta T$	$\Delta \rho$
#1	1960	1690	7500	10	100
#2	1910	1640	7200	10	100
#2	1880	1600	7200	10	100
#2	1850	1580	7200	10	100
#2	1820	1550	7300	10	100
#2	1790	1520	7300	10	100
#2	1770	1490	7300	10	100

Continued on next page

## 7 Outlook

Table 7.1: Obtained density data of steel  $W_{360}$

sample	$T / K$	$T / ^\circ C$	$\rho$	$\Delta T$	$\Delta \rho$
#2	1740	1460	7300	10	100
#3	1870	1590	7300	10	100
#3	1820	1550	7300	10	100
#3	1780	1510	7200	10	100
#4	1930	1650	6900	10	100
#4	1900	1630	7000	10	100
#4	1860	1590	7000	10	100
#4	1830	1550	7100	10	100
#4	1810	1530	7000	10	100
#4	1770	1500	7100	10	100
#5	1880	1610	7100	10	100
#5	1810	1540	7100	10	100
#5	1780	1500	7200	10	100
#5	1750	1480	7100	10	100
#5	1730	1460	7200	10	100

Table 7.2: Surface tension data points of steel  $W_{360}$  obtained at this thesis.

sample	$T / K$	$T / ^\circ C$	$\gamma$	$\Delta T$	$\Delta \gamma$
#1	1960	1690	1740	20	30
#2	1930	1660	1740	20	30
#2	1910	1640	1760	20	30
#2	1890	1610	1760	20	30
#2	1850	1580	1770	20	30
#2	1820	1550	1770	20	30
#2	1760	1490	1780	20	30
#2	1730	1460	1770	20	30
#3	1850	1580	1750	20	30
#3	1810	1540	1750	20	30
#4	1930	1660	1750	20	30
#4	1920	1650	1760	20	30
#4	1890	1620	1770	20	30
#4	1860	1580	1770	20	30

Continued on next page

Table 7.2: Obtained surface tension data of steel W360

sample	$T / \text{K}$	$T / ^\circ\text{C}$	$\gamma$	$\Delta T$	$\Delta\gamma$
#4	1820	1550	1770	20	30
#4	1800	1530	1780	20	30
#4	1770	1500	1770	20	30
#5	1870	1600	1740	20	30
#5	1810	1530	1730	20	30
#5	1770	1500	1740	20	30
#5	1750	1480	1750	20	30
#6	1910	1630	1730	20	30
#6	1860	1580	1750	20	30
#6	1820	1550	1750	20	30

Table 7.3: Exemplary data points of density and surface tension linear fits of steel W360 with corresponding uncertainties.

$T / \text{K}$	$T / ^\circ\text{C}$	$\rho$	$\Delta\rho$	$\gamma$	$\Delta\gamma$
1730	1460	7200	100	1760	20
1740	1470	7200	100	1760	20
1750	1480	7200	100	1760	20
1760	1490	7200	100	1760	20
1770	1500	7200	100	1760	20
1780	1510	7200	100	1760	20
1790	1520	7200	100	1760	20
1800	1530	7200	100	1760	20
1810	1540	7200	100	1760	20
1820	1550	7200	100	1760	20
1830	1560	7200	100	1750	20
1840	1570	7100	100	1750	30
1850	1580	7100	200	1750	30
1860	1590	7100	200	1750	30
1870	1600	7100	200	1750	30
1880	1610	7100	200	1750	30
1890	1620	7100	200	1750	30
1900	1630	7100	200	1750	30
1910	1640	7100	200	1750	40

Continued on next page

## 7 Outlook

Table 7.3: Exemplary data points of density and surface tension linear fits of steel *W360* with corresponding uncertainties

$T / \text{K}$	$T / ^\circ\text{C}$	$\rho$	$\Delta\rho$	$\gamma$	$\Delta\gamma$
1920	1650	7100	200	1750	40
1930	1660	-	-	1750	40
1940	1670	-	-	1750	40
1950	1680	-	-	1750	40
1960	1690	-	-	1750	40

## Nickel

In Table 7.4 and 7.5, density and surface tension data points of nickel obtained within this study are summarised. Information regarding corresponding experimental parameter are given in Table 5.5. Expanded uncertainties were determined according to *GUM* [42]. In addition, exemplary data points of the obtained fitting equations are stated in Table 7.6. In the end of this section, certificates of analysis provided by suppliers are attached.

Table 7.4: Density data points of nickel obtained at this thesis.

sample	$T / \text{K}$	$T / ^\circ\text{C}$	$\rho$	$\Delta T$	$\Delta\rho$
AA#1	1620	1350	7800	20	200
AA#3	1820	1550	7700	20	200
AA#3	1790	1520	7700	20	200
AA#3	1760	1490	7700	20	200
AA#3	1720	1440	7800	20	200
AA#5	1780	1510	7300	20	100
AA#10	1840	1560	7700	20	200
AA#10	1830	1550	7700	20	200
AA#10	1820	1550	7700	20	200
AA#10	1800	1530	7700	20	200
AA#10	1780	1510	7700	20	200
AA#10	1770	1490	7700	20	200
AA#10	1750	1470	7700	20	200

Continued on next page

Table 7.4: Obtained density data of nickel

sample	$T / \text{K}$	$T / ^\circ\text{C}$	$\rho$	$\Delta T$	$\Delta\rho$
AA#10	1730	1450	7800	20	200
AA#10	1710	1430	7800	20	200
AA#10	1690	1410	7800	20	200
AA#10	1670	1400	7800	20	200
AA#10	1640	1360	7800	20	200
AA#10	1620	1350	7800	20	200
AA#10	1600	1330	7800	10	200
AA#10	1580	1310	7900	10	200
SA#2	1660	1380	7800	20	200
SA#3	1780	1510	7700	20	200
AA#11	1780	1510	7600	20	200
AA#11	1750	1480	7700	20	200
AA#11	1730	1460	7700	20	200
AA#11	1720	1440	7700	20	200
AA#11	1710	1430	7700	20	200
AA#12	1870	1590	7700	20	200
AA#12	1840	1570	7700	20	200
AA#12	1830	1550	7700	20	200
AA#12	1800	1530	7700	20	200
AA#12	1800	1530	7700	20	200
AA#12	1760	1490	7800	20	200
AA#12	1730	1460	7800	20	200
AA#12	1700	1430	7800	20	200
AA#12	1670	1400	7800	20	200
GF#2	1750	1480	7700	20	200
GF#3	1820	1540	7700	20	200
SA#4	1810	1530	7700	20	200
SA#5	1840	1570	7700	20	200
GF#4	1850	1580	7600	20	200
GF#5	1860	1590	7700	20	200
GF#5	1770	1490	7800	20	200
SA#6	1880	1610	7600	20	200
SA#6	1850	1580	7600	20	200

Continued on next page

## 7 Outlook

Table 7.4: Obtained density data of nickel

sample	$T / \text{K}$	$T / ^\circ\text{C}$	$\rho$	$\Delta T$	$\Delta\rho$
SA#6	1840	1560	7700	20	200
SA#6	1820	1540	7700	20	200
SA#6	1800	1520	7700	20	200
SA#6	1780	1510	7700	20	200
SA#6	1770	1490	7800	20	200
SA#6	1750	1470	7800	20	200
SA#6	1730	1450	7800	20	200
SA#6	1700	1430	7800	20	200
SA#7	1800	1530	7700	20	200

Table 7.5: Surface tension data points of nickel obtained at this thesis.

sample	$T / \text{K}$	$T / ^\circ\text{C}$	$\gamma$	$\Delta T$	$\Delta\gamma$
AA#1	1810	1530	1720	20	30
AA#1	1760	1480	1730	20	30
AA#1	1720	1450	1750	20	30
AA#1	1660	1390	1770	20	30
AA#1	1620	1350	1780	20	30
AA#2	1800	1530	1730	20	30
AA#2	1750	1480	1740	20	30
AA#2	1750	1480	1740	20	30
AA#2	1770	1500	1730	20	30
AA#2	1780	1510	1740	20	30
AA#2	1760	1490	1740	20	30
AA#2	1750	1480	1740	20	30
AA#2	1760	1480	1750	20	30
AA#3	1860	1580	1710	20	30
AA#3	1850	1580	1700	20	30
AA#3	1820	1550	1720	20	30
AA#3	1790	1520	1720	20	30
AA#3	1760	1490	1730	20	30
AA#3	1710	1430	1750	20	30
AA#4	1730	1460	1730	20	30

Continued on next page

Table 7.5: Obtained surface tension data of nickel

sample	$T / \text{K}$	$T / ^\circ\text{C}$	$\gamma$	$\Delta T$	$\Delta\gamma$
AA#4	1780	1510	1720	20	30
AA#4	1790	1520	1720	20	30
AA#5	1790	1520	1700	20	40
AA#6	1780	1510	1730	20	30
AA#6	1770	1500	1730	20	30
AA#6	1770	1490	1730	20	30
AA#6	1750	1480	1730	20	30
AA#6	1700	1430	1750	20	30
AA#6	1700	1420	1750	20	30
AA#6	1660	1390	1770	20	30
AA#7	1880	1600	1690	20	30
AA#7	1870	1590	1700	20	30
AA#7	1850	1570	1710	20	30
AA#7	1830	1560	1720	20	30
AA#7	1810	1540	1720	20	30
AA#7	1800	1520	1730	20	30
AA#7	1780	1500	1730	20	30
AA#7	1760	1490	1730	20	30
AA#7	1740	1470	1740	20	30
AA#7	1720	1450	1740	20	30
AA#7	1700	1430	1750	20	30
AA#7	1690	1420	1760	20	30
AA#7	1670	1400	1760	20	30
AA#7	1650	1380	1760	20	30
AA#8	1870	1590	1700	20	30
AA#8	1860	1580	1700	20	30
AA#8	1840	1570	1710	20	30
AA#8	1830	1560	1710	20	30
AA#8	1810	1540	1710	20	30
AA#8	1800	1530	1720	20	30
AA#8	1790	1520	1720	20	30
AA#8	1770	1500	1730	20	30
AA#8	1760	1480	1730	20	30

Continued on next page

## 7 Outlook

Table 7.5: Obtained surface tension data of nickel

sample	$T / \text{K}$	$T / ^\circ\text{C}$	$\gamma$	$\Delta T$	$\Delta\gamma$
AA#8	1740	1460	1740	20	30
AA#8	1720	1450	1740	20	30
AA#8	1710	1430	1750	20	30
AA#9	1800	1530	1730	20	20
AA#9	1780	1510	1730	20	20
AA#9	1760	1490	1730	20	30
AA#9	1730	1460	1740	20	30
AA#9	1800	1530	1730	20	20
AA#9	1790	1510	1730	20	30
AA#9	1740	1470	1740	20	30
AA#9	1710	1440	1750	20	30
SA#1	1850	1580	1710	20	30
SA#1	1830	1560	1710	20	30
SA#1	1830	1550	1700	20	30
SA#1	1810	1540	1720	20	30
SA#1	1800	1520	1720	20	30
SA#1	1780	1510	1730	20	30
SA#1	1770	1500	1730	20	30
SA#1	1760	1480	1730	20	30
SA#1	1740	1470	1750	20	30
SA#1	1740	1460	1750	20	30
SA#1	1720	1450	1750	20	30
SA#1	1710	1430	1750	20	30
SA#1	1700	1420	1750	20	30
SA#1	1690	1420	1760	20	30
SA#1	1680	1400	1760	20	30
GF#1	1830	1560	1710	20	30
GF#1	1820	1550	1700	20	30
GF#1	1800	1530	1710	20	30
GF#1	1790	1520	1720	20	30
GF#1	1770	1500	1710	20	30
GF#1	1760	1480	1730	20	30
GF#1	1740	1460	1740	20	30

Continued on next page

Table 7.5: Obtained surface tension data of nickel

sample	$T / \text{K}$	$T / ^\circ\text{C}$	$\gamma$	$\Delta T$	$\Delta\gamma$
GF#1	1740	1460	1740	20	30
GF#1	1720	1450	1740	20	30
GF#1	1700	1430	1750	20	30
GF#1	1690	1410	1750	20	30
GF#1	1670	1400	1760	20	30
GF#1	1660	1380	1760	20	30
GF#1	1640	1360	1780	20	30
SA#2	1830	1560	1710	20	30
SA#2	1820	1540	1720	20	30
SA#2	1810	1540	1720	20	30
SA#2	1800	1520	1720	20	30
SA#2	1780	1500	1730	20	30
SA#2	1760	1480	1740	20	30
SA#2	1740	1460	1740	20	30
SA#2	1720	1450	1750	20	30
SA#2	1710	1440	1750	20	30
SA#2	1700	1420	1750	20	30
SA#2	1680	1410	1760	20	30
SA#3	1860	1590	1690	20	30
SA#3	1860	1580	1700	20	30
SA#3	1800	1530	1720	20	30
SA#3	1780	1500	1730	20	30
SA#3	1700	1430	1750	20	30
SA#3	1660	1390	1770	20	30
AA#11	1790	1520	1730	20	30
AA#12	1820	1550	1720	20	30
AA#12	1780	1510	1730	20	30
AA#12	1760	1480	1740	20	30
AA#12	1730	1460	1750	20	30
AA#12	1690	1420	1760	20	30
AA#12	1660	1390	1770	20	30
GF#2	1820	1540	1720	20	30
GF#2	1800	1530	1720	20	30

Continued on next page

## 7 Outlook

Table 7.5: Obtained surface tension data of nickel

sample	$T / \text{K}$	$T / ^\circ\text{C}$	$\gamma$	$\Delta T$	$\Delta\gamma$
GF#2	1790	1510	1730	20	30
GF#2	1770	1500	1730	20	30
GF#2	1750	1470	1720	20	30
GF#2	1730	1460	1740	20	30
GF#2	1720	1440	1750	20	30
GF#2	1700	1420	1750	20	30
GF#2	1680	1410	1760	20	30
GF#2	1670	1390	1750	20	30
GF#2	1630	1350	1780	20	30
GF#2	1610	1330	1780	20	30
GF#3	1850	1580	1710	20	30
GF#3	1840	1570	1700	20	30
GF#3	1830	1560	1700	20	30
GF#3	1810	1540	1720	20	30
GF#3	1800	1520	1710	20	30
GF#3	1790	1510	1720	20	30
GF#3	1770	1500	1730	20	30
GF#3	1760	1490	1730	20	30
GF#3	1750	1470	1740	20	30
GF#3	1730	1450	1740	20	30
GF#3	1720	1440	1740	20	30
GF#3	1700	1420	1750	20	30
GF#3	1680	1400	1750	20	30
GF#3	1640	1370	1770	20	30
GF#3	1620	1350	1770	20	30
SA#4	1850	1570	1710	20	30
SA#4	1850	1570	1700	20	30
SA#4	1830	1560	1720	20	30
SA#4	1830	1550	1720	20	30
SA#4	1800	1530	1720	20	30
SA#4	1790	1520	1730	20	30
SA#4	1780	1500	1730	20	30
SA#4	1760	1490	1740	20	30

Continued on next page

Table 7.5: Obtained surface tension data of nickel

sample	$T / \text{K}$	$T / ^\circ\text{C}$	$\gamma$	$\Delta T$	$\Delta\gamma$
SA#4	1750	1480	1740	20	30
SA#4	1650	1380	1770	20	30
SA#4	1640	1360	1780	20	30
SA#5	1870	1590	1700	20	30
SA#5	1870	1600	1700	20	30
SA#5	1850	1580	1710	20	30
SA#5	1840	1570	1710	20	30
SA#5	1830	1560	1710	20	30
SA#5	1820	1540	1720	20	30
SA#5	1810	1540	1720	20	30
SA#5	1790	1520	1730	20	30
SA#5	1730	1460	1750	20	30
SA#5	1720	1440	1750	20	30
SA#5	1700	1430	1760	20	30
SA#5	1690	1420	1760	20	30
SA#5	1670	1400	1760	20	30
GF#4	1810	1540	1720	20	30
GF#4	1780	1510	1730	20	30
GF#4	1770	1500	1730	20	30
GF#4	1760	1480	1740	20	30
GF#4	1710	1440	1740	20	30
GF#4	1690	1420	1760	20	30
GF#4	1680	1400	1750	20	30
GF#4	1660	1390	1750	20	30
GF#4	1640	1370	1760	20	30
GF#4	1620	1350	1780	20	30
GF#4	1600	1330	1770	20	30
GF#5	1870	1600	1690	20	30
GF#5	1860	1580	1700	20	30
GF#5	1840	1570	1710	20	30
GF#5	1830	1550	1700	20	30
GF#5	1810	1540	1720	20	30
GF#5	1790	1520	1720	20	30

Continued on next page

## 7 Outlook

Table 7.5: Obtained surface tension data of nickel

sample	$T / \text{K}$	$T / ^\circ\text{C}$	$\gamma$	$\Delta T$	$\Delta\gamma$
GF#5	1770	1500	1730	20	30
GF#5	1750	1480	1730	20	30
GF#5	1730	1460	1740	20	30
GF#5	1710	1440	1760	20	30
GF#5	1700	1420	1740	20	30
GF#5	1680	1410	1750	20	30
GF#5	1660	1380	1770	20	30
AA#13	1790	1510	1720	20	30
AA#13	1780	1510	1730	20	30
AA#13	1740	1460	1740	20	30
AA#13	1740	1470	1740	20	30
AA#13	1740	1460	1740	20	30
AA#13	1740	1460	1740	20	30
AA#13	1740	1460	1740	20	30
AA#13	1740	1460	1740	20	30
AA#13	1730	1460	1740	20	30
AA#13	1740	1460	1740	20	30
AA#13	1730	1460	1740	20	30
AA#13	1730	1460	1740	20	30
AA#13	1730	1460	1740	20	30
AA#13	1730	1460	1740	20	30
SA#7	1730	1460	1730	60	30
SA#7	1740	1470	1740	20	30
SA#7	1740	1460	1750	20	30
SA#7	1770	1500	1730	20	30
SA#7	1770	1500	1740	20	30
SA#7	1810	1540	1720	20	30
SA#7	1820	1540	1720	20	30
SA#7	1840	1560	1710	20	30
SA#7	1880	1600	1700	20	30
SA#7	1880	1600	1700	20	30
SA#7	1720	1440	1750	20	30

Table 7.6: Exemplary data points of density and surface tension linear fits of nickel with corresponding uncertainties.

$T / \text{K}$	$T / ^\circ\text{C}$	$\rho$	$\Delta\rho$	$\gamma$	$\Delta\gamma$
1580	1310	7900	100	-	-
1590	1320	7800	100	1790	10
1600	1330	7840	90	1780	10
1610	1340	7830	90	1780	10
1620	1350	7830	80	1780	10
1630	1360	7820	80	1770	10
1640	1370	7810	70	1770	10
1650	1380	7800	70	1770	10
1660	1390	7800	60	1760	10
1670	1400	7790	60	1760	10
1680	1410	7780	60	1760	10
1690	1420	7780	50	1750	10
1700	1430	7770	50	1750	10
1710	1440	7760	50	1750	10
1720	1450	7760	50	1750	10
1730	1460	7750	50	1740	10
1740	1470	7740	50	1740	10
1750	1480	7730	50	1740	10
1760	1490	7730	50	1730	10
1770	1500	7720	50	1730	10
1780	1510	7710	60	1730	10
1790	1520	7710	60	1720	10
1800	1530	7700	60	1720	10
1810	1540	7690	70	1720	10
1820	1550	7690	70	1710	10
1830	1560	7680	80	1710	10
1840	1570	7670	80	1710	10
1850	1580	7660	90	1710	10
1860	1590	7660	90	1700	10
1870	1600	7700	100	1700	10
1880	1610	7600	100	-	-



## Certificate of analysis

Product No.: 42331  
 Product: Nickel slug, 6.35mm (0.25in) dia x 6.35mm (0.25in) length,  
 Puratronic®, 99.995% (metals basis)  
 Lot No.: L29X008

Ni 99.998 %

Ag	< 0.05	Al	0.05	As	< 0.01	Au	< 0.05
B	< 0.001	Ba	< 0.001	Be	< 0.001	Bi	< 0.005
Br	< 0.01	C	10.5	Ca	< 0.05	Cd	< 0.01
Ce	< 0.001	Cl	< 0.05	Co	1	Cr	2.05
Cs	< 0.001	Cu	0.115	F	< 0.01	Fe	12.25
Ga	< 0.01	Ge	< 0.05	H	< 1	Hf	< 0.005
Hg	< 0.05	I	< 0.005	In	< 0.005	Ir	0.245
K	< 0.05	La	< 0.001	Li	< 0.001	Mg	< 0.005
Mn	0.032	Mo	0.32	N	1	Na	< 0.001
Nb	< 0.01	Nd	< 0.001	O	5	Os	0.215
P	0.01	Pb	0.018	Pd	< 0.05	Pt	< 0.05
Rb	< 0.001	Re	0.135	Rh	0.02	Ru	< 0.01
S	2.5	Sb	0.74	Sc	< 0.001	Se	< 0.01
Si	0.145	Sn	< 0.01	Sr	< 0.01	Ta	< 1
Te	< 0.005	Th	< 0.0001	Ti	0.185	Tl	< 0.01
U	< 0.0001	V	0.019	W	0.02	Y	< 0.001
Zn	0.08	Zr	< 0.005				

Values given in ppm unless otherwise noted  
 Oxygen and sulfur determined by LECO  
 All other elements determined by GDMS

This document has been electronically generated and does not require a signature.

Order our products online [www.alfa.com](http://www.alfa.com)

**ThermoFisher**  
 S C I E N T I F I C



**Goodfellow Cambridge Limited**  
Ermine Business Park, Huntingdon PE29 6WR England  
E-mail info@goodfellow.com  
Web : www.goodfellow.com  
Telefon 00 44 1480 424 800  
Telefax 00 44 1480 424 900

Institut fuer Experimentalphysik, TU Graz  
Petersgasse 16  
8010 GRAZ  
AUSTRIA

Ihr Zeichen

vom

Unser Zeichen

Datum

LS510703/J V

NI007950/28

28-Jan-2019

ANALYSENSCHEIN

Lieferscheinnummer : LS510703  
Ihre Auftragsnummer : 4500115794  
Artikel-Nr / Charge-Nr : NI007950/28

Nickel	: Matrix
Eisen	: 2.4
Iridium	: 0.48
Kobalt	: 1.85
Kupfer	: 0.385
Rhenium	: 0.24
Titan	: 0.405

Alle Werte sind in parts per million angegeben, wenn nicht anders vermerkt.  
Die Analyse ist auf der Basis dieser Materialcharge, entweder im Endzustand  
und oder im Laufe des Herstellungsprozesses, vorgenommen worden

## 7 Outlook

**SIGMA-ALDRICH®**

[sigma-aldrich.com](http://sigma-aldrich.com)

3050 Spruce Street, Saint Louis, MO 63103, USA  
Website: [www.sigmaaldrich.com](http://www.sigmaaldrich.com)  
Email USA: [techserv@sial.com](mailto:techserv@sial.com)  
Outside USA: [eurtechserv@sial.com](mailto:eurtechserv@sial.com)

Product Name:  
Nickel - rod, diam. 6.35 mm, ≥99.99% trace metals basis

### Certificate of Analysis

**Product Number:** 267074  
**Batch Number:** MKCD1178  
**Brand:** ALDRICH  
**CAS Number:** 7440-02-0  
**Formula:** Ni  
**Formula Weight:** 58.69 g/mol  
**Quality Release Date:** 09 MAY 2017

Ni

Test	Specification	Result
Appearance (Color) Grey	Conforms	Conforms
Appearance (Form) Rod	Conforms	Conforms
Diameter 6.35 mm	Conforms	Conforms
ICP Major Analysis Confirms Nickel Component	Confirmed	Confirmed
Trace Metal Analysis	≤ 100.0 ppm	< 100.0 ppm
Aluminum (Al)		< 0.1 ppm
Antimony (Sb)		1.9 ppm
Chromium (Cr)		< 0.1 ppm
Cobalt (Co)		2.5 ppm
Indium (In)		0.2 ppm
Iron (Fe)		2.6 ppm
Lanthanum (La)		< 0.1 ppm
Manganese (Mn)		< 0.1 ppm
Rhenium (Re)		0.1 ppm
Rhodium (Rh)		< 0.1 ppm
Ruthenium (Ru)		0.1 ppm
Silicon (Si)		0.2 ppm
Titanium (Ti)		0.4 ppm
Tungsten (W)		< 0.1 ppm
Ytterbium (Yb)		0.1 ppm
Zinc (Zn)		< 0.1 ppm

Sigma-Aldrich warrants, that at the time of the quality release or subsequent retest date this product conformed to the information contained in this publication. The current Specification sheet may be available at [Sigma-Aldrich.com](http://Sigma-Aldrich.com). For further inquiries, please contact Technical Service. Purchaser must determine the suitability of the product for its particular use. See reverse side of invoice or packing slip for additional terms and conditions of sale.

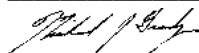
Version Number: 1

Page 1 of 2

## Certificate of Analysis

Product Number: 267074  
Batch Number: MKCD1178

Test	Specification	Result
Purity > = 99.99% Based On Trace Metals Analysis	Meets Requirements	Meets Requirements



Michael Grady, Manager  
Quality Control  
Milwaukee, WI US

Sigma-Aldrich warrants, that at the time of the quality release or subsequent retest date this product conformed to the information contained in this publication. The current Specification sheet may be available at [Sigma-Aldrich.com](http://Sigma-Aldrich.com). For further inquiries, please contact Technical Service. Purchaser must determine the suitability of the product for its particular use. See reverse side of invoice or packing slip for additional terms and conditions of sale.



# Bibliography

- [1] B. Buchmayr and G. Panzl. "Eine SWOT-Analyse zum Einsatz der Additiven Fertigung für metallische Bauteile." In: *BHM Berg- und Hüttenmännische Monatshefte* 160.1 (Dec. 2014), pp. 15–20. DOI: 10.1007/s00501-014-0326-1 (cit. on p. 2).
- [2] EPMA's European Hot Isostatic Pressing Group (EuroHIP). "Introduction to Hot Isostatic Pressing Technology." In: (2018). URL: <https://www.epma.com/epma-free-publications/product/introduction-to-hot-isostatic-pressing-brochure> (cit. on p. 2).
- [3] D. L. Cummings and D. A. Blackburn. "Oscillations of magnetically levitated aspherical droplets." In: *Journal of Fluid Mechanics* 224.-1 (Mar. 1991), p. 395. DOI: 10.1017/s0022112091001817 (cit. on pp. 3, 11–13, 50).
- [4] K. Aziz, A. Schmon, and G. Pottlacher. "Measurement of surface tension of liquid nickel by the oscillating drop technique." In: *High Temperatures-High Pressures* 44 (2015), pp. 475–481 (cit. on pp. vi, vii, 3, 50, 51, 54, 64, 65, 67, 69, 70, 80, 83).
- [5] T. Leitner, O. Klemmer, and G. Pottlacher. "Bestimmung der temperaturabhängigen Oberflächenspannung des Eisen-Nickel-Systems mittels elektromagnetischer Levitation." In: *tm-Technisches Messen* 84.12 (Dec. 2017), pp. 787–796. DOI: 10.1515/teme-2017-0085 (cit. on pp. 3, 44–47).
- [6] I. Egry, E. Ricci, R. Novakovic, and S. Ozawa. "Surface tension of liquid metals and alloys-Recent developments." In: *Advances in Colloid and Interface Science* 159.2 (Sept. 2010), pp. 198–212. DOI: 10.1016/j.cis.2010.06.009 (cit. on pp. 5, 76).

## Bibliography

- [7] K. J. Mysels. "The maximum bubble pressure method of measuring surface tension, revisited." In: *Colloids and surfaces* 43.2 (1990), pp. 241–262. DOI: 10.1016/0166-6622(90)80291-B (cit. on p. 5).
- [8] J. Brillo, G. Lohofer, F. S. Hohagen, S. Schneider, and I. Egry. "Thermophysical property measurements of liquid metals by electromagnetic levitation." In: *International Journal of Materials and Product Technology* 26.3/4 (2006), p. 247. DOI: 10.1504/ijmpt.2006.009469 (cit. on p. 5).
- [9] G. Lohöfer. "Theory of an electromagnetically levitated metal sphere I: absorbed power." In: *SIAM Journal on Applied Mathematics* 49.2 (Apr. 1989), pp. 567–581. DOI: 10.1137/0149032 (cit. on pp. 6, 7).
- [10] CODATA *Internationally recommended 2018 values of the Fundamental Physical Constants*. URL: <https://physics.nist.gov/cuu/Constants/index.html> (visited on 09/13/2019) (cit. on pp. 6, 7, 12, 14–16, 32).
- [11] D. Platzek, C. Notthoff, D. M. Herlach, G. Jacobs, D. Herlach, and K. Maier. "Liquid metal undercooled below its Curie temperature." In: *Applied Physics Letters* 65.13 (Sept. 1994), pp. 1723–1724. DOI: 10.1063/1.112898 (cit. on p. 8).
- [12] R. W. Hyers. "Fluid flow effects in levitated droplets." In: *Measurement Science and Technology* 16.2 (Jan. 2005), pp. 394–401. DOI: 10.1088/0957-0233/16/2/010 (cit. on p. 8).
- [13] J. Brillo, H. Fritze, G. Lohoefer, M. Schulz, and C. Stenzel. "Advanced measurement devices for the microgravity electromagnetic levitation facility EML." In: *Materials Research in Microgravity 2012*. Jan. 2012. URL: <https://ntrs.nasa.gov/archive/nasa/casi.ntrs.nasa.gov/20120015590.pdf> (visited on 08/30/2019) (cit. on p. 8).
- [14] I. Egry, G. Lohöfer, and G. Jacobs. "Surface tension of liquid metals: results from measurements on ground and in space." In: *Physical review letters* 75.22 (1995), p. 4043. DOI: 10.1103/PhysRevLett.75.4043 (cit. on p. 8).
- [15] P.-F. Paradis, T. Ishikawa, G.-W. Lee, D. Holland-Moritz, J. Brillo, W.-K. Rhim, and J. T. Okada. "Materials properties measurements and particle beam interactions studies using electrostatic levitation." In: *Materials Science and Engineering: R: Reports* 76 (2014), pp. 1–53. DOI: 10.1016/j.mser.2013.12.001 (cit. on p. 9).

- [16] C. Stenzel. "Materials science experiments under microgravity - a review of history, facilities, and future opportunities." In: *Materials Research in Microgravity 2012*. Jan. 2012. URL: <https://ntrs.nasa.gov/archive/nasa/casi.ntrs.nasa.gov/20120015590.pdf> (visited on 08/30/2019) (cit. on p. 9).
- [17] L. Rayleigh. "VI. On the capillary phenomena of jets." In: *Proceedings of the Royal Society of London* 29.196-199 (Dec. 1879), pp. 71–97. DOI: 10.1098/rsp1.1879.0015 (cit. on pp. 10, 50).
- [18] F. H. Busse. "Oscillations of a rotating liquid drop." In: *Journal of Fluid Mechanics* 142.-1 (May 1984), p. 1. DOI: 10.1017/s0022112084000963 (cit. on p. 11).
- [19] J. Q. Feng and K. V. Beard. "Small-amplitude oscillations of electrostatically levitated drops." In: *Proceedings of the Royal Society A* 430.1878 (July 1990), pp. 133–150. DOI: 10.1098/rspa.1990.0084 (cit. on pp. 14, 50).
- [20] F. Henning. *Temperaturmessung*. Springer Science Business Media, 1977. DOI: 10.1007/978-3-642-81138-8 (cit. on pp. 15, 16, 89).
- [21] K. Aziz. "Surface Tension Measurements of Liquid Metals and Alloys by Oscillating Drop Technique in combination with an Electromagnetic Levitation Device." PhD thesis. Graz: Graz University of Technology, 2016. URL: <http://diglib.tugraz.at/surface-tension-measurements-of-liquid-metals-and-alloys-by-oscillating-drop-technique-in-combination-with-an-electromagnetic-levitation-device-2016> (visited on 08/12/2019) (cit. on pp. 17, 18, 34, 36, 50, 54, 65).
- [22] A. Schmon. "Density Determination of Liquid Metals by Means of Containerless Techniques." PhD thesis. Graz: Graz University of Technology, 2016. URL: <http://diglib.tugraz.at/density-determination-of-liquid-metals-by-means-of-containerless-techniques-2016> (visited on 08/12/2019) (cit. on pp. 18, 30, 44).
- [23] T. Leitner. "Thermophysical properties of liquid aluminium determined by means of electromagnetic levitation." MA thesis. Graz University of Technology, Institute of Experimental Physics, 2016. URL: <http://diglib.tugraz.at/thermophysical-properties-of->

## Bibliography

- liquid-aluminium-determined-by-means-of-electromagnetic-levitation-2016 (cit. on pp. 18, 25, 30, 32).
- [24] O. Klemmer. "Surface tension of the liquid iron-nickel system determined by means of electromagnetic levitation." MA thesis. Graz University of Technology, 2017. URL: <http://diglib.tugraz.at/surface-tension-of-the-liquid-iron-nickel-system-determined-by-means-of-electromagnetic-levitation-2017> (cit. on pp. 18, 37).
- [25] *Datasheet of IMPAC IS 6 Advanced and IGA 6 Advanced*. LumaSense. 2018. URL: [https://www.lumasenseinc.com/uploads/Products/Temperature\\_Measurement/Infrared\\_Thermometers/IMPAC\\_Pyrometers/Series\\_6/pdf/DE-IS-IGA-6-Advanced\\_Datenblatt.pdf](https://www.lumasenseinc.com/uploads/Products/Temperature_Measurement/Infrared_Thermometers/IMPAC_Pyrometers/Series_6/pdf/DE-IS-IGA-6-Advanced_Datenblatt.pdf) (visited on 09/10/2019) (cit. on p. 21).
- [26] *Datasheet of IMPAC ISR 6-TI Advanced*. LumaSense. 2019. URL: [https://www.lumasenseinc.com/uploads/Products/Temperature\\_Measurement/Infrared\\_Thermometers/IMPAC\\_Pyrometers/Series\\_6/pdf/DE-ISR6-TI-Advanced\\_Datenblatt.pdf](https://www.lumasenseinc.com/uploads/Products/Temperature_Measurement/Infrared_Thermometers/IMPAC_Pyrometers/Series_6/pdf/DE-ISR6-TI-Advanced_Datenblatt.pdf) (visited on 09/10/2019) (cit. on p. 21).
- [27] *Datasheet of Alphagaz 1 Argon*. Air Liquide S.A. 2008. URL: <https://produkte.airliquide.de/gasekatalog/pdb/alphagaz1argon.pdf> (visited on 09/10/2019) (cit. on pp. 22, 56).
- [28] *Datasheet of ARCAL 10*. Air Liquide S.A. 2008. URL: <https://produkte.airliquide.de/gasekatalog/pdb/arc10.pdf> (visited on 09/10/2019) (cit. on p. 22).
- [29] *Datasheet of Alphagaz 1 Helium*. Air Liquide S.A. 2008. URL: <https://produkte.airliquide.de/gasekatalog/pdb/alphagaz1argon.pdf> (visited on 09/10/2019) (cit. on p. 22).
- [30] *Datasheet of Alphagaz 1 Hydrogen*. Air Liquide S.A. 2008. URL: <https://produkte.airliquide.de/gasekatalog/pdb/alphagaz1wasserstoff.pdf> (visited on 09/10/2019) (cit. on p. 22).
- [31] J. Rumble. *CRC Handbook of Chemistry and Physics, 100th Edition*. Taylor & Francis Ltd., June 21, 2019. 1700 pp. ISBN: 9781138367296 (cit. on pp. 23, 52, 61, 63, 65, 70).

- [32] I. Egry and J. Brillo. "Surface Tension and Density of Liquid Metallic Alloys Measured by Electromagnetic Levitation." In: *Journal of Chemical & Engineering Data* 54.9 (Sept. 2009), pp. 2347–2352. DOI: 10.1021/je900119n (cit. on p. 24).
- [33] J. Lee and D. Matson. "Prediction of Mass Evaporation of Fe<sub>50</sub>Co<sub>50</sub> During Measurements of Thermophysical Properties Using an Electrostatic Levitator." In: *International Journal of Thermophysics* 35.9-10 (2014), pp. 1697–1704. DOI: 10.1007/s10765-014-1662-9 (cit. on pp. 24, 86).
- [34] A. Höll. "Entwicklung und Fertigung der Probenwechseinheit für die elektromagnetische Levitation." Bachelor thesis. TU Graz, 2019 (cit. on p. 25).
- [35] F. Kametriser. "Ansteuerung und Auswertung eines Gasdurchflussreglers zur Optimierung der Temperaturregelung während EML-Versuchen." 2019 (cit. on p. 25).
- [36] voestalpine BÖHLER Edelstahl GmbH & Co KG. *Plastic Mould Steels*. Oct. 11, 2019. URL: [https://www.boehler-edelstahl.com/app/uploads/sites/92/2018/08/BW010En\\_Plastic-Mould-Steels.pdf](https://www.boehler-edelstahl.com/app/uploads/sites/92/2018/08/BW010En_Plastic-Mould-Steels.pdf) (cit. on p. 39).
- [37] M. Hirtler. "Beurteilung der Einflussgrößen auf die Verdüsbarekeit von Metallschmelzen." MA thesis. Montanuniversität Leoben, 2018 (cit. on p. 40).
- [38] J. Brillo and I. Egry. "Density and excess volume of liquid copper, nickel, iron, and their binary alloys." In: *International Journal of Materials Research* 95.8 (Aug. 2004), pp. 691–697. DOI: 10.3139/146.018009 (cit. on pp. 44, 61).
- [39] H. Kobatake and J. Brillo. "Density and thermal expansion of Cr-Fe, Fe-Ni, and Cr-Ni binary liquid alloys." In: *Journal of Materials Science* 48.14 (Mar. 2013), pp. 4934–4941. DOI: 10.1007/s10853-013-7274-0 (cit. on p. 44).
- [40] A. Grosse and A. Kirshenbaum. "The densities of liquid iron and nickel and an estimate of their critical temperature." In: *Journal of Inorganic and Nuclear Chemistry* 25.4 (Apr. 1963), pp. 331–334. DOI: 10.1016/0022-1902(63)80181-5 (cit. on p. 44).

## Bibliography

- [41] M. Watanabe, M. Adachi, and H. Fukuyama. "Densities of Fe–Ni melts and thermodynamic correlations." In: *Journal of Materials Science* 51.7 (Dec. 2015), pp. 3303–3310. DOI: 10.1007/s10853-015-9644-2 (cit. on p. 44).
- [42] W. G. 1. of the Joint Committee for Guides in Metrology (JCGM/WG 1). *Evaluation of measurement data – Supplement 2 to the "Guide to the expression of uncertainty in measurement" – Extension to any number of output quantities*. BIPM, 2011. URL: [https://www.bipm.org/utils/common/documents/jcgm/JCGM\\_102\\_2011\\_E.pdf](https://www.bipm.org/utils/common/documents/jcgm/JCGM_102_2011_E.pdf) (cit. on pp. 45, 46, 60, 62, 63, 73, 91, 97, 100).
- [43] Landolt-Börnstein. "Thermodynamic Properties of Elements, Callcium to Germanium." In: *Pure Substances. Part 1: Elements and Compounds from AgBr to Ba<sub>3</sub>N<sub>2</sub>*. Springer Nature, 1999, pp. 25–50. DOI: 10.1007/10652891\_5 (cit. on pp. 45, 47).
- [44] B. J. Keene, K. C. Mills, and R. F. Brooks. "Surface properties of liquid metals and their effects on weldability." In: *Materials Science and Technology* 1.7 (July 1985), pp. 568–571. DOI: 10.1179/mst.1985.1.7.559 (cit. on pp. 50, 51, 53).
- [45] K. Nogi, K. Ogino, A. McLean, and W. A. Miller. "The temperature coefficient of the surface tension of pure liquid metals." In: *Metallurgical Transactions B* 17.1 (Jan. 1986), pp. 163–170. DOI: 10.1007/bf02670829 (cit. on pp. 50, 51, 53).
- [46] J. Schade, A. McLean, and W. Miller. "Surface tension measurements on oscillating droplets of undercooled liquid metals and alloys." In: *Undercooled Alloy Phases* (1986), pp. 233–248 (cit. on pp. 50, 51, 53).
- [47] M. P. SanSoucie, J. R. Rogers, V. Kumar, J. Rodriguez, X. Xiao, and D. M. Matson. "Effects of Environmental Oxygen Content and Dissolved Oxygen on the Surface Tension and Viscosity of Liquid Nickel." In: *International Journal of Thermophysics* 37.7 (June 2016). DOI: 10.1007/s10765-016-2085-6 (cit. on pp. 50, 51, 54).
- [48] T. Ishikawa, P.-F. Paradis, and Y. Saita. "Thermophysical Property Measurements of Molten Nickel Using an Electrostatic Levitation Furnace." In: *Journal of the Japan Institute of Metals* 68.9 (2004), pp. 781–786. DOI: 10.2320/jinstmet.68.781 (cit. on pp. 50, 51, 53, 54).

- [49] K. Eckler, I. Egry, and D. M. Herlach. "Measurements of surface tension on levitated oscillating metallic drops." In: *Materials Science and Engineering: A* 133 (Mar. 1991), pp. 718–721. DOI: 10.1016/0921-5093(91)90170-R (cit. on pp. 50, 51, 53).
- [50] S. Sauerland, K. Eckler, and I. Egry. "High-precision surface tension measurements on levitated aspherical liquid nickel droplets by digital image processing." In: *Journal of Materials Science Letters* 11.6 (1992), pp. 330–333. DOI: 10.1007/bf00729172 (cit. on pp. 50, 51, 53).
- [51] J. Brillo and I. Egry. "Surface tension of nickel, copper, iron and their binary alloys." In: *Journal of Materials Science* 40.9-10 (May 2005), pp. 2213–2216. DOI: 10.1007/s10853-005-1935-6 (cit. on pp. 50, 51).
- [52] R. Brooks and K. Mills. "Measurement of the thermophysical properties of melts by a levitated-drop method." In: *High Temperatures-High Pressures* 25.6 (1993), pp. 657–664 (cit. on pp. 50, 51).
- [53] S. Ozawa, S. Takahashi, N. Watanabe, and H. Fukuyama. "Influence of Oxygen Adsorption on Surface Tension of Molten Nickel Measured Under Reducing Gas Atmosphere." In: *International Journal of Thermophysics* 35.9-10 (Sept. 2014), pp. 1705–1711. DOI: 10.1007/s10765-014-1674-5 (cit. on pp. 50, 51, 77).
- [54] W. D. Kingery and M. Humenik Jr. "Surface tension at elevated temperatures. I. Furnace and method for use of the sessile drop method; surface tension of silicon, iron and nickel." In: *Journal of Physical Chemistry* 57.3 (Mar. 1953), pp. 359–363. DOI: 10.1021/j150504a026 (cit. on p. 51).
- [55] V. V. Fesenko and M. I. Vasiliu. "Temperature Dependence of the Surface Tension of Cobalt and Nickel." In: *Poroshkovaya Metallurgiya* 3 (1961), pp. 25–28 (cit. on p. 51).
- [56] B. C. Allen. "The surface tension of liquid transition metals at their melting points." In: *The American Institute of Mining, Metallurgical, and Petroleum Engineers* 227 (1963). URL: <https://www.onemine.org/document/abstract.cfm?docid=25191&title=Institute-of-Metals-Division--The-Surface-Tension-of-Liquid-Transition-Metals-at-Their-Melting-Points> (cit. on p. 51).

## Bibliography

- [57] G. D. Ayushina, E. S. Levin, and P. V. Geld. "Influence of Temperature and Composition on the Density and Surface Energy of Molten Alloys of Aluminium with Cobalt and Nickel." In: *Russian Journal of Physical Chemistry* 43.11 (1969), pp. 2756–2760 (cit. on p. 51).
- [58] F. Xiao, L. Fang, and K. Nogi. "Surface Tension of Molten Ni and Ni-Co Alloys." In: *Journal of Materials Science & Technology* 21.2 (2005), pp. 201–206. DOI: 10.3321/j.issn:1005-0302.2005.02.013 (cit. on p. 51).
- [59] A. Schmon, K. Aziz, and G. Pottlacher. "Density Determination of Liquid Copper and Liquid Nickel by Means of Fast Resistive Pulse Heating and Electromagnetic Levitation." In: *Metallurgical and Materials Transactions A: Physical Metallurgy and Materials Science* 46.6 (Mar. 2015), pp. 2674–2679. DOI: 10.1007/s11661-015-2844-1 (cit. on pp. 60, 61).
- [60] P. M. Nasch and S. G. Steinemann. "Density and Thermal Expansion of Molten Manganese, Iron, Nickel, Copper, Aluminum and Tin by Means of the Gamma-Ray Attenuation Technique." In: *Physics and Chemistry of Liquids* 29.1 (Jan. 1995), pp. 43–58. DOI: 10.1080/00319109508030263 (cit. on p. 61).
- [61] S. K. Chung, D. B. Thiessen, and W.-K. Rhim. "A noncontact measurement technique for the density and thermal expansion coefficient of solid and liquid materials." In: *Review of Scientific Instruments* 67.9 (Sept. 1996), pp. 3175–3181. DOI: 10.1063/1.1147584 (cit. on p. 61).
- [62] M. Schmid. *Vapor Pressure Calculator*. IAP/TU Wien Surface Physics Group. URL: [https://www.iap.tuwien.ac.at/www/surface/vapor\\_pressure](https://www.iap.tuwien.ac.at/www/surface/vapor_pressure) (visited on 10/16/2019) (cit. on p. 78).
- [63] X. Xiao, R. W. Hyers, R. K. Wunderlich, H.-J. Fecht, and D. M. Matson. "Deformation induced frequency shifts of oscillating droplets during molten metal surface tension measurement." In: *Applied Physics Letters* 113.1 (July 2018), p. 011903. DOI: <https://doi.org/10.1063/1.5039336> (cit. on p. 79).
- [64] E. Becker, W. J. Hiller, and T. A. Kowalewski. "Experimental and theoretical investigation of large-amplitude oscillations of liquid droplets." In: *Journal of Fluid Mechanics* 231 (Oct. 1991), pp. 189–210. DOI: 10.1017/s0022112091003361 (cit. on p. 79).

## Bibliography

- [65] E. Trinh and T. G. Wang. "Large-amplitude free and driven drop-shape oscillations: experimental observations." In: *Journal of Fluid Mechanics* 122.-1 (Sept. 1982), p. 315. DOI: 10.1017/s0022112082002237 (cit. on p. 79).
- [66] M. GmbH. *GUM Workbench - Benutzerhandbuch für Version 1.3, 2.3 und 2.4*. 2011 (cit. on p. 92).